UNIVERSITY OF CALIFORNIA,

LOS ANGELES

# Multi-frequency Harmonic Acoustography for Tissue Identification and Border Detection

A dissertation submitted in partial satisfaction of
the requirements for the degree
Doctor of Philosophy in Electrical Engineering

by

Ashkan Maccabi

2016

ABSTRACT OF THE DISSERTATION

Multi-frequency Harmonic Acoustography for Tissue Identification and Border Detection

by

Ashkan Maccabi

Doctor of Philosophy in Electrical Engineering

University of California, Los Angeles, 2016

Professor Warren Grundfest, Chair

Tissue identification and border delineation of diseased regions are essential for surgeons during surgical operations in tumor excisions. In the absence of an imaging technique that provides quantitative well-defined margins by identifying diseased from healthy regions, palpation of the tissue during surgery is the only practical option. To ensure complete resection of the diseased region, surgeons typically require large margins surrounding the suspect tissue in order to reduce the possibility of leaving behind any unhealthy tissue. The goal of this project is to develop an imaging modality that utilizes vibroacoustography (VA) technique to spatially map the contrast in mechanical and acoustic properties between malignant and normal tissue for abnormal tissue identification and border delineation. By enhancing boundary regions between malignant and healthy tissue, with this novel imaging technique, surgical margins are decreased and as a result, the resection of healthy tissue is potentially minimized. Some approaches that are used in the detection of tumor regions include conventional ultrasound, manual palpation, and CT scan. However, they suffer from limitations such as lack of sensitivity, subjectivity, and low contrast.

As an alternative, VA provides an enhanced image of the boundary lines using the mechanical and acoustic properties of the target as the main mechanism of contrast. This work outlines the development of a VA medical imaging system for enhanced border detection as well as:

- Construction, improvement, and advancement of the VA system
- Characterization and optimization of VA system parameters such as point spread function (PSF), modulation transfer function (MTF), lateral and axial resolution of the imaging beam, and sensitivity and specificity specifications for biomedical imaging applications
- Investigation of VA feasibility in imaging mechanical properties of targets
- Design of a compact VA system for *in vivo* applications to enhance tissue characterization and boundary detection

The imaging system includes a dual electrode transducer, which possesses a confocal, piezoelectric element that produces two relatively close ultrasonic tones. When the two tones overlap at the point of interest, the beat frequency of the two tones is generated in a non-linear regime. The long-term goal of VA medical imaging is to provide a quantitative, intra-operative method of detecting the border between malignant and healthy tissue during surgical procedures. In the scope of this dissertation work, this study aims to culminate with *in vivo* system design and determination of tissue mechanical properties in pre-clinical models.

This dissertation of Ashkan Maccabi is approved.

Maie A. St. John

Oscar M. Stafsudd

Robert N. Candler

Zachary D. Taylor

Warren Grundfest, Committee Chair

University of California, Los Angeles

2016

*To my parents, brother, sister, and almighty creator whose support have been with me all along.*

# Table of Contents

# List of Figures

# List of Tables

# Acknowledgements

منت خدای را عزوجل که طاعتش موجب قربتست و به شکر اندرش مزید نعمت هر نفسی که فرو میرود ممد حیاتست و چون بر میاید مفرح ذات پس در هر نفسی دو نعمت موجودست و برهر نعمت شکری واجب.

First and foremost, I would like to take this opportunity and show my appreciation and gratitude toward my parents and my siblings for their support, guidance, and more importantly their patience. Their vast support made me realize the greatest gift of family and its everlasting compassion. Especially, I would like to thank my parents for their kindness and unconditional love toward me amid my success, failures, and accomplishments as a person and as a future PhD.

I also would like to express my gratitude to my adviser, Professor Warren Grundfest. Without his support, mentorship, and guidance this work would not have been accomplished.

I would like to also thank my committee members for their time, effort, and critical feedback.

UCLA Biophotonics, UCLA Electrical Engineering, UCLA Bioengineering, and CASIT graduate colleagues including Ahmad Abiri, Rory Geoghegan, Eric Johnson, Yiwen Meng, Alan Priester aka “aP”, Meghedi Babakhanian aka “luv”, James Garritano aka “Jimmy”, Shijun Sung, Neha Bajwa, Priyamvada Tewari, Artemio Navarro aka “Temo”, Nathan Francis, Paymon Rezaii, Andrew Shin, Sammy Norris, Stephanie Delgado, Shadi Kordbacheh, Max Ho, William Yao, Marko Kostic, Asael Papour, David Bennett, Justin Thai, Armin Arshi, and Adria Sherman among many other students I forgot to mention deserve my appreciation and gratitude.

My most gratitude also goes toward the Postdocs as well as residents like George Saddik, Zachary Taylor, Bryan Nowroozi, Irene Kim, and Bobby Tajudeen, whose leadership and assistance guided me through the graduate path. I especially would like to thank George and Zach who were with me throughout the process each and every day and showed me how to get on the “fast track”.

Shijun Sung aka “homey”, you were more than a colleague to me. You were more like a mentor in some cases of course. Whenever I needed help in MATLAB or needed a nice scientific discussion, you were there for me. Whenever I needed that extra burden to study for the EE prelim, you were there for me. I just want to thank you for all your support and devotion toward me throughout both undergrad and graduate years at UCLA.

Alan Priester aka “aP”, you made CASIT fun with your movie previews using my face. Up to this day, I do not know how you got your hands on my picture, but I am glad you did. You have an unusual talent for Photoshop and cinematography; I think it is worth perusing, perhaps after you get your PhD of course.

Meghedi Babakhanian aka “luv”, thank you for being with me as a TA for my first UCLA class and as a colleague throughout graduate school, I never forget our discussions “gossips” about funding and our superiors. I know you are at a better place now at Stanford, well at least I hope. I wish you success and happiness wherever you are.

James Garritano aka “Jimmy”, thanks for believing and defending me no matter what the situation was. Up to this day, I still remember our long discussions about Vibro and how the previous Graduate student on the project was wrong about the imaging setup and image generation. I greatly appreciate your help and wish you the best of luck at Yale.

Neha Bajwa aka “lil Bajwa”, I do not know where to start. You along Shijun were with me at all times. Whenever I needed extra help, be it grant writings, manuscript writings, experimental setup *i.e.* rat liver attaining, or just chatting about the project, you were there for me. You helped me in any way you could and for that I would like to express my utmost gratitude.

To my undergraduates, Ahuva Weltman, Albert Cheng, Nikan Namiri, and Suraj Dhanjani, I would like to thank you and hope you succeed at whatever you desire. Especially, Nikan, you share the same birthday as me, so I demand you to cherish it.

צדיק נופל שבע פעמים, קום, אבל מעידת רשעי פורענות.

Funding for the completion of this work was provided by the Jonsson Comprehensive Cancer Center and Elsa U. Pardee foundation.

# Curriculum Vitae

## EDUCATION

**University of California, Los Angeles, CA**

**Ph.D. in Electrical Engineering** **Expected December 2016**
Concentration: Biomedical Instrumentation e.g. Acoustics

**M.S. in Biomedical Engineering** **March 2013**
Concentration: Biomedical Instrumentation e.g. Acoustics

**B.S. in Bioengineering** **July 2011**
Concentration: Terahertz imaging and system development, **Cum Laude**
Completed Management Series at UCLA

## RESEARCH EXPERIENCE

**Graduate Researcher** September **2011** – **Present**

- Center for Advanced Surgical and Interventional Technology (CASIT), UCLA
- Biophotonics Laboratory, UCLA

## TEACHING EXPERIENCE

**Mathematics and Physics Instructor, West Coast Ultrasound Institute** July **2015 - Present**

**Teaching Fellow, UCLA** September **2012- Present**

- **BIOENGR167L** (Prof. D. Di Carlo), **CHEM154** (Dr. S. Nakamoto), **ENGR112** (Prof. D. Bristow), **BIOENGR188** (Dr. G. Saddik), **EL ENGR173DA/B** (Prof. Stafsudd), **EL ENGR176** (Prof. Ozcan)

**Mentor, UCLA** June **2010 – Present**

- **CEED** and **HSSRP** programs for more than 20 students

**Consultant, UCLA** September **2014– Present**

**Academic Tutor** September **2006 – Present**

## PATENT

- Warren Grundfest, Maie St. John, **Ashkan Maccabi**, George N. Saddik, Zachary D. Taylor. Multi Frequency Harmonic Acoustography for Target Identification and Border Detection. The Regents of the University of California, a California Corporation, assignee. Patent UC. Case No. UC-2017-223-2-LA. Oct. 2016.

## PUBLICATIONS AND CONFERENCE PAPERS

- **Ashkan Maccabi**, Yiwen Meng, Nikan Namiri, Zachary Taylor, Maie St. john, Warren Grundfest, George Saddik. "Compact Vibroacoustography (VA) System Design and Characterization." 38th IEEE Engineering in Medicine and Biology (EMBC). 2016 Aug 16-20; Orlando, FL.
- N. Namiri, **A. Maccabi**, N. Bajwa, M. St. John, G. Saddik, Z. Taylor, and W. Grundfest. "Vibroacoustography system characterization using parallel difference frequency and elasticity measurements for potential applications in tumor margin detection." Biomedical Engineering Society (BMES) Annual Meeting. 2016 Oct 5-8, Minneapolis, MN.
- Li Ling, Ahmad Abiri, **Ashkan Maccabi**, Warren Grundfest, and Robert Candler. "Measurements of Hysteretic Stress-strain Curves of Porcine and Rat Liver Tissue at Different Loading Rates." Biomedical Engineering Society (BMES) Annual Meeting. 2016 Oct 5-8, Minneapolis, MN.
- **A. Maccabi**, Z. Taylor, N. Bajwa, J. Mallen-St Clair, M. St John, S. Sung, W. Grundfest, and G. Saddik. "An examination of the elastic properties of tissue-mimicking phantoms using vibro-acoustography and a muscle motor system." Review of Scientific Instruments 87, no. 2 (2016): 024903.
- M. Babakhanian, B. Nowroozi, G. Saddik, **A. Maccabi**, N. Bajwa, and W. Grundfest. "Acoustic characterization of low intensity focused ultrasound system through skull." Journal of Therapeutic Ultrasound 3, no. Suppl 1 (2015): P13.
- A. P. Mulgaonkar, R. Singh, G. N. Saddik, **A. Maccabi**, W. P. Melega, M. O. Culjat, and W. S. Grundfest. "Design of a minimally invasive low-frequency microtransducer for ultrasonic neuromodulation." In Ultrasonics Symposium (IUS), 2014 IEEE International, pp. 405-408. IEEE, 2014.
- **A. Maccabi**, A. Arshi, J. Garritano, G. Saddik, E. Kohanbash, B. A. Tajudeen, M. St John, W. S. Grundfest, and Z. D. Taylor. "Ultrasound-stimulated vibro-acoustography for high-resolution differentiation based on viscoelastic properties of tissue mimicking phantoms." Studies in health technology and informatics 196 (2013): 262-264.
- **A. Maccabi**, J. Garritano, A. Arshi, G. Saddik, B. A. Tajudeen, M. St John, W. S. Grundfest, and Z. D. Taylor. "Ex vivo viscoelastic characterization of head and neck tissue abnormalities using ultrasound-stimulated vibro-acoustography (USVA)." In SPIE Medical Imaging, pp. 904006-904006. International Society for Optics and Photonics, 2014.
- **A. Maccabi** , D. B. Bennett , N. Bajwa , P. Tewari , S. Sung , W. S. Grundfest , Z. D. Taylor, "Reflectivity measurements of water and dioxane mixtures using a 100 GHz Gunn diode source. Proc. SPIE 8585, (2013).
- **A. Maccabi,** G.N. Saddik, N. Bajwa, M. St. John, W.S. Grundfest. "Characterization of the elasticity of embedded objects in PVA phantoms using USVA." 14th UC Systemwide Bioengineering Symposium; 2013 Jun 19-21; San Diego, CA.
- D. B. Bennett, Z. D Taylor , P. Tewari , S. Sung **, A. Maccabi** , R. S. Singh , M. O. Culjat , W. S Grundfest , J. Hubschman , E. R. Brown, "Corneal Hydration Sensing Through the Terahertz Band: In Vivo Results at 100 GHz", Journal of Biomedical Optics, SPIE (2012).
- S. Sung, D.B. Bennett, Z. D. Taylor, N. Bajwa, **A. Maccabi**, P. Tewari, M. Culjat, R. Singh, and W. Grundfest."Reflective measurement of water concentration using millimeter wave illumination." Proc. SPIE 7984: 798434(2011).

## 1. Introduction

Boundary detection and identification based on various physical properties of tissue are important fields that remain to be fully investigated. These fields can be further investigated and used to develop new imaging modalities for mapping the human body and assisting surgeons in intra-operative surgical procedures. Mechanical parameters, such as viscoelastic properties of biological tissue, are emerging factors that various medical imaging modalities desire to utilize as their main contrast mechanism to characterize regions with different mechanical properties and to identify pathological conditions. The most critical prognostic indicator for a disease is its stage at the time of diagnosis, which is most commonly performed using palpation [1]. In conventional palpation, a physician applies a static force to the tissue and crudely estimates tissue stiffness by feeling with the fingers [2]. Stiffness of soft tissue is often related to its respective composition, and the relative difference between neighboring tissues is often correlated to pathology and treatment. Many malignancies, like cancers of the breast or prostate, appear as lesions of higher stiffness relative to neighboring healthy tissue and therefore can be distinguished from normal surrounding tissues by identifying the difference in mechanical properties [3]. Moreover, many studies have shown a positive correlation between stiffness and diseased state in breast, liver, prostate, and arterial tissues, further leading to the thorough investigation of the factors behind this correlation [4-6]. In addition, treatment of advanced-stage head and neck cancer often requires complicated multimodal management strategies, such as complete surgical resection of the tumor, and is associated with high morbidity and poor patient outcomes [7]. Therefore, given that histologically sufficient resections with clear margins are difficult in practice, positive margins - defined as the presence of any viable tumor at the edge of the resected tumor- are common and associated with significantly decreased survival [8]. Although using tissue stiffness as a differentiating criteria for

pathological identity is clinically acceptable, the delineation of malignant lesions from benign lesions by clinical inspection alone is unreliable, subjective, and may be insensitive to small or deep lesions [9, 10]. Thus, there is a need for more accurate and sensitive diagnostic tools that can detect early lesions and determine either their potentially malignant or benign nature to assist surgeons real-time with tumor excision procedures. The main goal of viscoelastic imaging systems is to non-invasively acquire high-resolution images with sufficient SNR (signal to noise ratio) and real-time quantitative viscoelastic maps of regions to relatively distinguish regions with different viscoelastic properties.

## 1.1. Mechanical Parameters

It is necessary to understand certain parameters in order to approach the basis of imaging modalities that generate quantitative viscoelasticity maps of targets. For simplicity, all the parameters discussed in this section will be defined in one dimension

Stress is defined as an applied force per unit area as shown in equation 1.1 and is usually measured in units of kPa. In this particular application, the stress will be applied to biological tissue that will undergo deformation.

$$\sigma = \frac{F}{A} \tag{1.1}$$

In equation 1.1, $\sigma$ is stress, $F$ is the external force in Newton, and $A$ is the area of the tissue in $cm^2$. Strain, defined in equation 1.2, is a dimensionless parameter that is defined as the ratio of relative changes in geometry of an object due to the applied external force with respect to its original shape.

$$\varepsilon = \frac{\Delta l}{l_0} \tag{1.2}$$

where $\varepsilon$ is strain, $\Delta l$ is the relative size change in cm, and $l_0$ is the original size of the object in cm.

Elastic modulus, $E$, is a constant that describes the tendency of an object to deform along an axis when an external force is applied along that axis. In another words, it is defined as the slope of stress to strain in the linear regime, and it contributes heavily to the elasticity portion of the mechanical properties of tissues [11].

$$E = \frac{\sigma}{\varepsilon} \tag{1.3}$$

Bulk modulus, $K$, is a constant that measures the tendency of an object to deform in all directions when uniform pressure is applied in all directions. It is defined as pressure over volumetric strain and it is an extension of elastic modulus to three dimensions, hence volumetric strain [11].

$$K = \frac{p}{\varepsilon_V} \tag{1.4}$$

where $p$ is the applied pressure in units of kPa and $\varepsilon_V$ is the volumetric strain.

Shear modulus or modulus of rigidity, $\mu$, is another constant that describes an object's tenacity to shear stress when acted upon by opposing forces parallel to one face of the object while the opposite face is held fixed by another equal force. It is defined as the ratio of shear stress to shear strain and contributes heavily to the viscosity portion of the mechanical properties of tissues [11].

$$\mu = \frac{\sigma_{shear}}{\varepsilon_{shear}} \tag{1.5}$$

where $\sigma_{shear}$ is the shear stress in kPa and $\varepsilon_{shear}$ is the shear strain.

These three aforementioned moduli can be related to one another using Fung *et al*. continuum mechanics in a homogeneous isotropic medium:

$$\mu = \frac{E}{2(1+\vartheta)} = \frac{3KE}{9K-E} = \frac{3K(1-2\vartheta)}{2(1+\vartheta)} \tag{1.6}$$

where $\vartheta$ is the Poisson ratio, the ratio of the transverse contracting strain to the elongation strain of biological materials. For incompressible materials, $\vartheta$ is between 0.45 to 0.5, and for biological

materials it is assumed to be 0.5 [5, 12]. As for acoustic wave speed through tissue, two types of speed can be formulated 1) compressional speed, $c_b$, in terms of bulk modulus, $K$, and 2) shear speed, $c_s$, in terms of shear modulus, $\mu$, and unperturbed mass density of the medium, $\rho_0$.

$$c_b = \sqrt{\frac{E(1-\vartheta)}{\rho_0(1+\vartheta)(1-2\vartheta)}} \tag{1.7}$$

$$c_s = \sqrt{\frac{\mu}{\rho_0}} = \sqrt{\frac{E}{2\rho_0(1+\vartheta)}} \tag{1.8}$$

## 1.2. Ultrasonography Imaging Systems

Over the past decades, ultrasonography, which relies on wave scattering and differences in acoustic impedance, has been extensively used to image soft tissue lesions [13]. It has been used as a diagnostic imaging modality for approximately 25% of all imaging examinations and in other fields such as nondestructive testing of products and structures for detecting flaws [13-15]. Ultrasound (US) is an acoustic wave at frequencies greater than maximum human audible frequencies of 20 kHz, as defined by the American National Institute. The frequency of choice is application dependent, primarily because there exists a tradeoff between spatial resolution and depth of penetration. A pressure plane wave, $p(x,t)$, propagating along $x$-dimension, through a homogeneous medium can be shown as:

$$p(x,t) = Pe^{-\alpha x}\cos(\omega t - kx) \tag{1.9}$$

where $P$ is the amplitude of the propagating acoustic wave, $\omega = 2\pi f$ is the radian frequency in rad/sec , $\alpha$ (Np/m) is the attenuation coefficient, and $k = \frac{2\pi}{\lambda}$ is the wave number in rad/m.

The primary causes of attenuation of US waves in a medium are specular reflections (mirror-like reflection), diffuse reflections (rough surfaces), scattering, interference, and thermal absorption

[15]. US scattering usually occurs when the acoustic wave encounters an impedance difference in the propagating medium, where the equation for impedance is given as

$$Z = \rho_0 c \tag{1.10}$$

where $Z$ is the acoustic impedance, $\rho_0$ is the undisturbed mass density of the medium, and $c$ is the speed of sound in medium. Constructive and destructive interference of scattered echoes are other sources of attenuation that can provide snowy patterns, speckle, in US generated images. Speckle results from random interference of the scattered ultrasound waves emitted from the probe, reducing the contrast of US imaging and limits the detection of small structures. Although US is non-invasive and can provide sufficient images of lesions that a physician may have prior knowledge about, *i.e.* location and physical properties from a biopsy, the echo pattern and morphological structure of some lesions especially in oral cavity tissues may not be sufficient enough for lesion detection [13, 16]. The primary property of tissue that affects US wave propagation and scattering is bulk modulus, which, for biological tissue, only differs from that of water by less than 15%. Because of this close similarity, US also fails to provide sufficient contrast in distinguishing lesions from background noise generated by the tissue in acute situations [13, 14, 16].

## 1.3.Elastography Imaging Methods

In 1991, Ophir *et al.* introduced the idea of elastography, which utilizes strain and elastic moduli properties of soft tissue to map the aforementioned properties of tissues in a high-resolution fashion. The method uses an external static stimulus at the surface of the tissue and by comparison of the pre and post-compressional echo signals, the system generated axial strain profiles (elastogram). Elastography converts the strain profiles to an elastic modulus profile by measuring the applied stress from the compressing device while using correction factors to accommodate for

the non-uniformity of the applied stimulus [17]. Since Ophir *et al.'s* system was in its preliminary state, signal distortion from pre to post-compression states, the sampling frequency, SNR, detection scheme of harmonic motion, time-delay and displacement estimation, and achievable axial resolution were not optimized and remained to be further investigated. However, more sophisticated signal processing and error suppression techniques such as use of Kalman filter and use of various spline-base algorithms, along with other resources, have been introduced to increase the accuracy of this technique [18-20]. Two of the main conventional elastography methods, transient and shear-wave, will be introduced and discussed in this section.

### 1.3.1. Transient Method

Transient elastography uses an excitation-focused ultrasound probe to produce localized distortion to the tissue, resulting in a transient deformation of the object, which is measured by another transducer (Doppler probe). This technique is known as a pulse-echo ultrasound, which uses a pulsed ultrasound probe to induce deformation, and a Doppler probe to detect the transient relaxation response of the object, illustrated in Figure 1. The generated images are a function of viscoelastic parameters of the tissue, providing one-dimensional images of tissue stiffness, bulk modulus [14]. This technique is used mainly by the FibroScan system for liver assessment [21]. Moreover, this method obeys Hooke's law, and the main contrast mechanism is the bulk modulus of the object. However, the amplitude of the generated compressional wave within the object only highlights few elastic variations, ~ one order of magnitude within the object. Additionally, transient elastography has poor sensitivity as a result of low contrast and the invasiveness of the procedure, deeming this technique not suitable for intra-operative imaging of viscoelastic properties of tissue [13, 14, 16].

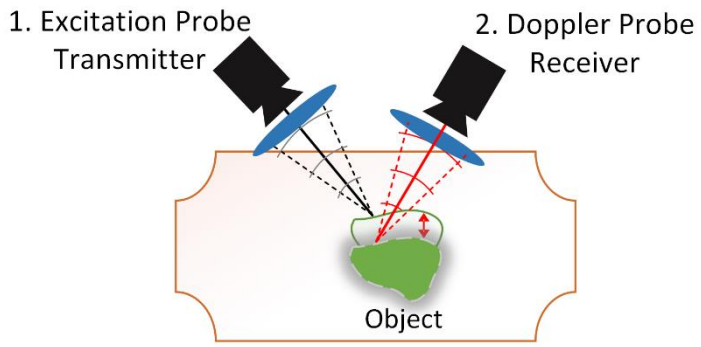


**Figure 1**: Transient elastography technique. An excitation ultrasound probe (1) is used to perturb the object and causes a small displacement, and Doppler ultrasound probe (2) is used to measure the deformation.

### 1.3.2. Shear-wave Method

Another emerging technique used in the field is shear-wave elastography (SWE), illustrated in Figure 2. SWE utilizes an amplitude-modulated focused ultrasound beam to produce a localized radiation stress that causes the object to be deformed, and as a result, provides deformation propagations in the form of shear waves through the object. The generated shear waves travel at very low speeds, a few meters per second through tissue, and are detected by a phase-sensitive MRI to further map the spatial distribution of the resulting displacement in the object in a three dimensional fashion [13, 16, 22]. However, SWE has limits on the intensity used for imaging, in order to avoid both mechanical and thermal bio-effects, which may cause difficulties in analyzing deeply located tissues. Moreover, the generated shear waves are highly attenuated within soft tissue, approximately 2-3 orders of magnitude higher than that of compressive waves, which as a result can limit the depth of penetration [14]. Also, long duration of scan time, patient discomfort, and the bulkiness of the MRI system are other problems that have limited the use of this technique in evaluating viscoelastic properties of tissue during intra-operative surgical procedures.

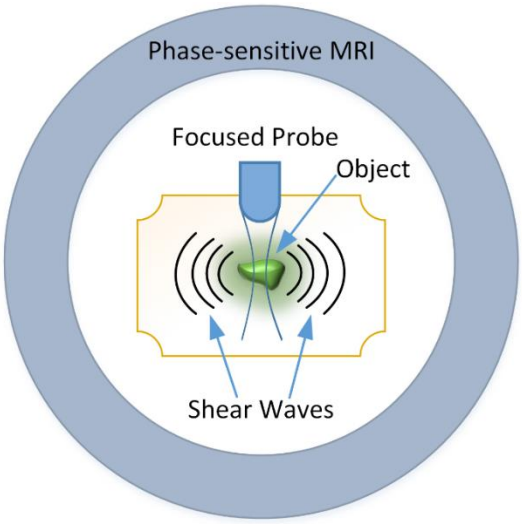


**Figure 2**: Shear-wave elastography technique. A focused ultrasound probe is used to perturb the object and produces deformation in the form of shear waves. The resultant oscillating shear wave displacements from within the object are detected by a phase-sensitive MRI.

## 1.4.Other Imaging Systems

Other imaging systems rely on vital dye injections, optical coherence tomography (OCT), combinations of acoustic and optical techniques, and visual assessments during surgeries [8, 9]. Vital dyes and radiolabeled colloid dye injection techniques are adept at detecting tumors. However, prior knowledge about the tumors is necessary, and diagnosis based on these images are associated with lower identification rates, more false negatives, and less tumor detection, especially in the neck and axilla [23]. OCT is an optical medical modality that utilizes near-infrared light to detect high resolution, sufficient depth of penetration, and three-dimensional images of biological tissues, especially in the retina of the eye. This technique uses low-coherence interferometry to provide tomographic visualization of biomolecules, subcellular components, cells, and internal tissues [24]. OCT systems can provide high spatially resolved information about tissue; however, the depth of penetration and field of view (FOV) are very limited and can make clinical usage of such devices difficult without prior knowledge about the target.

Photoacoustic technique is another modality system that uses electromagnetic energy, *i.e.* lasers, to locally induce thermal gradient tissue and detect the generated acoustic waves from the thermal expansion/contraction by a separate ultrasonic transducer. Since tissue encompasses viscoelastic behavior, there is a phase lag between the excitation stage and the thermal expansion/contraction stage. Thus in order to map the tissue in terms of these viscoelastic properties, an ultrasonic transducer is used to map the pressure waves generated from the thermal expansion/contraction of the tissue [25, 26]. Equation 1.11 relates the generated surface stress ($\sigma$) in terms of elastic modulus, $E$, coefficient of linear expansion, $\alpha$, Poisson's ratio, $\vartheta$, modulation frequency, $\omega$, and temperature, $T$, $T = T_0 e^{j\omega t}$:

$$\sigma = -\frac{E\alpha T_0 e^{j\omega t}}{(1-\vartheta)} \tag{1.11}$$

$$\sigma = E\varepsilon + \eta\dot{\varepsilon} \tag{1.12}$$

$$\varepsilon(t) = \varepsilon_A e^{j(\omega t+\delta)} \tag{1.13}$$

$$\delta = \arctan(\frac{\eta\omega}{E}) \tag{1.14}$$

Moreover, using the rheological Kelvin–Voigt model, the stress–strain relationship can be expressed by equation. 1.12 [27]. Combining equations. 1.11 and 1.12, we can express the generated strain response in terms of the surface acoustic stress by equations. 1.13 where the amplitude of the complex strain is $\varepsilon_A = \frac{-E^2\alpha T}{(E^2+\eta^2\omega^2)[cos\delta(1-\vartheta)]}$. The strain phase delay, , is calculated by equation. 1.14, which relates the viscosity, , and elastic modulus, $E$, to the phase delay, the main contrast mechanism in this technique.

Gao *et al.* demonstrated Phase Resolved Photoacoustic (PRPA) by using an intensity-modulated CW laser, with a wavelength of 808 nm and frequency of 50 kHz, as an excitation source, and an

ultrasonic transducer as a detector with the same center frequency as the modulation rate. A lock-in amplifier was used to detect the signal and calculate the phase lag between the detected acoustic wave and the reference signal [28]. Even though, the generated images have high resolution, sub-micrometer, shallow depth of penetration (~ 100 μm), high light scattering, and attenuation are crucial factors that make this technique non-ideal for intra-operative surgical procedures.

Optical Coherence Elastography (OCE), first introduced by Jacques *et al.* and Schmitt in 1998 [29, 30], is a derivative of the optical coherence tomography technique to detect depth-resolved sample deformation induced by quasi-static compression. The technique uses various compression schemes to estimate the local mechanical properties, *i.e.* viscoelasticity, throughout the tissue. In this technique, the surface acoustic phase velocity, $c_p$, is directly proportional to the elastic modulus in an elastic homogeneous half-space by equation. 1.15, where $\rho$ for soft tissue is assumed to be ~1000 kg/m$^3$:

$$c_p = \frac{0.86 + 1.12\vartheta}{1 + \vartheta} \sqrt{\frac{E}{2\rho(1 + \vartheta)}} \tag{1.15}$$

The first of the two most conventional OCE methods is compression OCE, which implements a local quasi-static external loading compression to the tissue. The elastic modulus is then calculated from the local stress at the sample surface and the generated strain (inverse approach) by the OCT system [26].

The second method uses dynamic load surface acoustic waves (SAW) from an actuator, typically at a lateral distance of ~ 0.5–20 mm, to compress the tissue. The resulting dispersion is detected by the OCT system. SAW is frequency dependent in a way that at higher frequencies it depends more heavily on the elasticity of top layer (soft layer) and as the frequency decreases, it becomes dependent on both (soft and hard) layers [26].

The third method employs internal loading by the distribution of magnetic nanoparticles (MNPs) in the tissue and excitation using an external magnetic field to produce localized, nanometer-scale tissue displacements, which are then detected by the OCT system [26].

OCE has illustrated high lateral resolution, ~ micron and submicron, due to its OCT detection scheme and dissection of elastic properties of materials due to its excitation scheme. This high resolution, non-invasive imaging modality allows OCE to evaluate the mechanics of intact tissue *in vivo* and on a scale that cannot be attained by pure elastography techniques. The current research area for OCE imaging is to investigate the microscopic deformation of porcine muscle and human skin as a function of depth and to develop intravascular OCE for rupture-prone (vulnerable) plaque detection. However, shallow depth of penetration, ~ 200 μm, coupled with high light scattering and attenuation have challenged this technique as a viable modality for real-time applications [26, 31].

## 1.5. Vibroacoustography

In 1957, Westervelt, introduced the idea of vibroacoustography (VA) by illustrating theoretical work on collinear plane waves. He illustrated in his historic article, “The Scattering of Sound by Sound”, that if two plane waves travel collinearly in free-space, they will produce propagating sum and difference frequency waves only locally in the interaction region of the two primary waves [32]. It was until the late 1990s when Fatemi and Greenleaf proposed the idea of vibroacoustography technique as an imaging method that utilized the nonlinear properties of acoustic waves to generate a map of what was inferred to be the mechanical response of a target to a dynamic force. The acoustic response is hypothesized to be a function of the mechanical properties of the target, through acoustic waves in the low kHz range, which can further be used

to produce a high contrast, sufficient SNR, and high resolution image of the intended target [1, 33].

In theory, the mechanical response of an object to a dynamic radiation force, *F*, is in terms of vector drag coefficient, $d_r$, the projected area on the target, *S*, and average energy density of the incident wave, $\langle E \rangle = \frac{p(t)^2}{\rho_0 c^2}$ and can be shown by equation 1.16:

$$F = d_r S \langle E \rangle \tag{1.16}$$

### 1.5.1. Generation of Pressure Waves

For this VA technique, two sinusoidal ultrasound beams are focused at two slightly different frequencies ($f_1$ and $f_2 = f_1 + \Delta f$) in low MHz range shown by equation 1.17:

$$p_1(r,t) = P_1(r)\cos\big(\omega_1 t + \varphi_1(r)\big) \; and \; p_2(r,t) = P_2(r)\cos\big(\omega_2 t + \varphi_2(r)\big) \tag{1.17}$$

where $P_1(r)$ and $P_2(r)$ are the amplitude of the two pressure waves, $\omega_i = 2\pi f_i$ is the angular frequency of both waves, $\varphi_1(r)$ and $\varphi_2(r)$ are the arbitrary phase function of the two pressure waves, and $r = \sqrt{x^2 + y^2 + z^2}$ is the position vector. For generation of these two tunes, two techniques can be used: 1. Summation of two amplitude modulated ultrasonic waves with small difference in frequency, $f_1$ and $f_2 = f_1 + \Delta f$, with two different focused ultrasound probes, and 2. Generation of two co-focused ultrasonic waves, $f_1$ and $f_2 = f_1 + \Delta f$, with a confocal ultrasound probe that focuses the two beams at a focus volume where they constructively interfere to vibrate the region.

As a result of either technique a stress field at the beat frequency and the totaling frequency are generated within the object at the focus volume. The combination of both pressure waves are shown by equations 1.18 and 1.19 where 1.19 illustrates the calculated total radiation force at the focus region. Since we are only interested in the dynamic part of the pressure wave at the focus

region, equation 1.20 uses short-term time average of the energy density, $\langle \xi(t) \rangle = \frac{1}{T}\int_{t-\frac{T}{2}}^{t+\frac{T}{2}} \xi(\tau) d\tau$ where $\frac{2\pi}{\omega_1} \ll T \ll \frac{4\pi}{\Delta\omega}$ to retain the first three terms and eliminate the other terms. Therefore, equation. 1.20 only shows the difference frequency at the surface of the object:

$$F_{total}(\mathrm{r,t}) = \frac{d_r S}{\rho_0 c^2}(\mathrm{p_1(r) + p_2(r)})^2 \tag{1.18}$$

$$F_{total}(r,t) = \frac{d_r S}{\rho c^2}\left\{\frac{P_1^2(r)}{2} + \frac{P_2^2(r)}{2} + P_1(r)P_2(r)cos\big((\Delta\omega)t + \Delta\varphi(r)\big) + \right.$$

$$P_1(r)P_2(r)cos\big((\omega_1+\omega_2)t + (\varphi_1+\varphi_2)(r)\big) + \frac{P_1^2(r)}{2}cos\big(2\omega_1 t + 2\varphi_1(r)\big) + \tag{1.19}$$

$$\left.\frac{P_2^2(r)}{2}cos\big(2\omega_2 t + 2\varphi_2(r)\big)\right\}$$

$$F_{\Delta\omega}(r,t) = \frac{d_r S}{2\rho c^2}P_1(r)P_2(r)cos\big((\Delta\omega)t + \Delta\varphi(r)\big) \tag{1.20}$$

### 1.5.2. Detection of Pressure Waves

In response to the applied oscillating radiation force, the object vibrates and produces an acoustic emissions field at the difference frequency ($\Delta f$ ). This emissive wave is measured at a distance away from the focus spot using a highly sensitive hydrophone near the object and is demonstrated by equation 1.21:

$$P_{(\Delta\omega)} = \rho_0 c^2 H_{(\Delta\omega)}(l) Q_{(\Delta\omega)} F_{(\Delta\omega)} \tag{1.21}$$

where the detected pressure, $P_{\Delta\omega}$, is in terms of medium density, $\rho_0$, speed of sound in the medium, $c$, medium transfer function, $H_{(\Delta\omega)}(l)$, the radiation force, $F_{(\Delta\omega)}$, and total acoustic outflow by an object per unit force, $Q_{\Delta\omega}$. The function $Q_{\Delta\omega}$ relates the mechanical response of the object to the dynamic radiation force applied to the object, based on its parametric effects, and is illustrated by

equation 1.22 where $Y_{\Delta\omega}$ is the admittance, ability to allow vibration to flow which is $Y \stackrel{\text{def}}{=} \frac{1}{Z}$ and $\pi b^2$ is the vibrating area:

$$Q_{\Delta\omega} = 2\pi b^2 Y_{\Delta\omega} = {}^{2\pi b^2}/_{Z_{\Delta\omega}} \tag{1.22}$$

Moreover, a nonlinear relationship between ultrasound waves and received acoustic pressure amplitude exists and that depends on the object's shape, size, and mechanical properties within the focus volume at the beat frequency [34, 35]. By scanning the focused beam spot over an object, an image is created of the spatially varying signal intensity and phase of the tissue's emitted acoustic wave in response to the transducer's beams [1, 33]. VA uses either continuous wave (CW) or tone-burst ultrasound, and due to the high sensitivity of hydrophone detectors, it has been demonstrated that a sub-millimeter object can be detected at ultrasound intensities far below the FDA limit, 720 mW/cm$^2$ [36]. Figure 3 demonstrates vibroacoustography method in imaging targets.

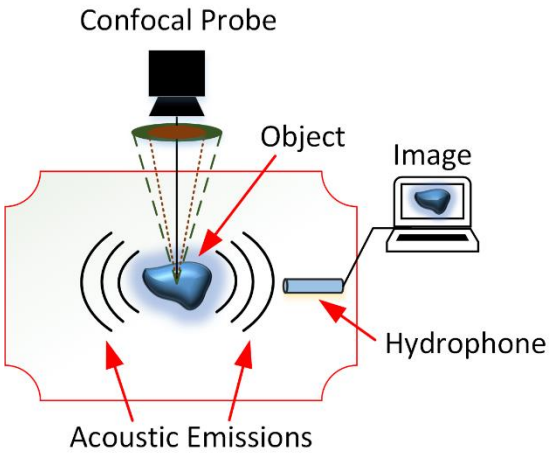


**Figure 3**: Vibroacoustography method. An object is vibrated by a confocal transducer, two slightly different frequencies in the low MHz range, and the emitted acoustic waves, based on the viscoelastic properties of the object, are collected by a nearby hydrophone to produce an image.

### 1.5.3. Potential Applications of Vibroacoustography

VA furnishes high contrast maps of tissues in response to a localized, low-frequency acoustic radiation force [16, 33]. In comparison to palpation, the transverse spatial resolution of VA is in the sub-millimeter range and the depth resolution is in the sub-centimeter range, making the technique more suitable for high-resolution detection and imaging for real-time, non-contact applications than the previously described imaging methods [22]. Moreover, in comparison to conventional ultrasound, VA provides speckle-free images. In conventional ultrasound, the scatterers are roughly the same size as the wavelength of the ultrasound (MHz) and as a result, the generated images are convoluted by speckle-noise. On the other hand, the generated acoustic emissions for VA are low kHz, and thus there is a beneficial mismatch between the wavelengths of the scatters and the incoming ultrasonic waves, which allows for production of speckle-free images [37]. The VA technique has been used for microcalcification identification for distinction of benign and malignant regions in breast tissues [38, 39], arterial plaque visualization in animals as well as humans [34, 40], viscoelastic parameter characterization on tissue mimicking phantoms (TMPs) and solid targets [1, 33, 41, 42], prostate tissue imaging for diagnostic and therapeutic applications, particularly in detecting brachytherapy seeds and monitoring cryotherapy [43, 44], topological sensitivity evaluations [45], small partial-thickness rotator cuff tears diagnosis [46], total hip arthroplasty assessment [47], and boundary detection in TMPs and various organs by multiple groups such as liver and thyroid [35, 48, 49].

Although spatial and depth resolutions of the modality are extensively characterized, the source of contrast behind VA imagery remains to be further investigated for this technology to gain traction as a diagnostic tool. Much theoretical work has been performed, using wave principles that suggests the acoustic response of the object, usually in the low kHz range for biological material,

is a function of the material properties of the target, [1, 33, 50, 51]. However, the amplitude and distribution of object motion is also related to the boundary conditions, such as coupling and the loading effects of the surrounding medium, as well as power absorption and scattering due to the object, which remains to be further investigated [1]. In addition, many of the aforementioned applications rely on the application of either static or spatially wide external forces -using a dynamic force is preferred to measure the dynamic characteristics of the material- rendering static and spatially wide forces inaccurate. Moreover, based on wave theory, VA images depict information that not only includes the dynamic, or mechanical, characteristics of the object but also the ultrasonic properties of the object, which may be beneficial for other imaging applications.

## 1.6. Thesis Overview

The main objective of this dissertation is to confirm and validate viscoelastic properties as the dominant contrast mechanism for VA, a novel imaging method for non-invasive detection of defined boundaries between malignant and normal tissues for intra-operative applications. This technique will provide greater specificity due to its sensitivity to viscoelastic properties of the targets than aforementioned technologies can provide. Despite many advances in VA imaging technique, there are still shortcomings in providing quantitative imagery for estimating the viscoelastic properties of tissues. Understanding the fundamental mechanism of the non-linear relationship between acoustic emissive signal intensity, phase variations, and the mechanical properties of tissues is a crucial first step in directing this technique into clinical settings. Due to complexity of the involved variables, *i.e.* viscosity, elasticity, acoustic properties, and surrounding area effect, generated acoustic emissions are at times difficult to interpret, and because of this, sometimes a combination of various imaging modalities can be beneficial in for making clear the details of tissue mechanical properties. Therefore, to investigate and further develop this VA

technology, this dissertation will explore other imaging techniques as well as theories that rely on mechanical properties, *i.e.* viscoelasticity, of targets to further help with the facilitation of this technology into operating rooms and hospital settings.

This dissertation outlines the development, construction, characterization, investigation, calibration, and verification of a VA medical imaging system in mapping viscoelastic properties of tissues by:

I. Construction and development of VA imaging system for modeling and evaluation of tissue mimicking phantoms (TMPs) and *ex vivo* tissue viscoelastic properties

II. Development and optimization of the system parameters such as point spread function (PSF) of the system, modulation transfer function (MTF), lateral and axial resolution of ultrasound beam, sensitivity and specificity specifications for biomedical imaging applications by utilizing tissue mimicking phantoms (TMPs) and *ex vivo* cancer specimens.

III. Investigation of the feasibility of VA system in imaging viscoelastic properties of targets by performing parallel viscoelasticity measurements in isotropic homogeneous phantoms and *ex vivo* pre-clinical models by basic contact mechanical testing, *i.e.* static.

IV. Design and calibration of a compact VA system and transducer/hydrophone design for *in vivo* applications to enhance tissue boundary between normal and malignant regions with sufficient contrast, necessary resolution, and high signal-to-noise ratio (SNR).

In addition, we will present empirical inputs on the relationships between VA's signal intensity and phase variations and the mechanical properties of biological material to generate a mathematical model to highlight the findings. If successful, these efforts will provide the groundwork to identify a promising intervention that warrants larger scale research efforts or multi-site clinical trials.

# 2. Vibroacoustography System Construction and Development

Vibroacoustography (VA) is a novel imaging modality that generates a map of the acoustic response of a target to a dynamic force. The acoustic response of the target, usually in low kHz range, is a function of its mechanical properties and can further be used to produce a high contrast, high resolution, and sufficient SNR image of the intended target [1]. By focusing two sinusoidal ultrasound beams at two slightly different frequencies ($f_1$ and $f_2 = f_1 + \Delta f$), a stress field at the beat frequency is generated within a small volume of the target. In response to the applied oscillating force, the target vibrates and produces an acoustic emissions field at the difference frequency ( $\Delta f$ ). This emissive wave is measured at a distance away from the focus spot using a highly sensitive hydrophone near the target. The received amplitude is theoretically correlated to the mechanical properties in the focus volume of the target at the excitation frequencies. By scanning the focused beam spot over an object, an image is created of the spatially varying signal intensity of the tissue [1, 33]. This chapter will delve into the VA system's design, construction, and experimental confirmation of the system's feasibility in imaging soft targets.

## 2.1. System Components and Construction

Two function generators (Agilent (Currently Keysight) 33220A, Santa Clara, CA) are used to generate the required tones (3.16 MHz for the inner transducer and 3.198 MHz for the outer transducer), which are split using a 3dB splitter (Minicircuits, Inc., Brooklyn, NY) into a frequency mixer to generate the reference signal for the receiver and the input signal for the power amplifiers (PA), (AR Modular, Inc., Bothell, WA), as illustrated in Figure 4. The PAs drive the curved confocal piezoelectric transducer element (Boston Piezo-Optics, Bellingham, MA). On the detection side, the target is placed in a water tank, for maximum coupling of the acoustic wave, at the focal region of the two ultrasound beams and the acoustic generated emission from the target,

typically on the order of 0 dBm, is detected using a sensitive hydrophone (TC4014-5, Teledyne Reson Inc., Goleta, CA) with a sensitivity of -180 dB re 1V/µPa. The hydrophone is placed at approximately 2 cm away from the target in a water tank, which couples the generated acoustic waves from the transducer to the object in addition to coupling the emitted acoustic waves from the object to the hydrophone. The output of the hydrophone is directly connected to a low noise amplifier (LNA), programmable bandpass filter (SRS 650, Stanford Research Systems Inc., Sunnyvale, CA), and a Lock-in Amplifier (SRS 844, Stanford Research Systems Inc., Sunnyvale, CA) for quadrature detection of the emitted difference frequency.

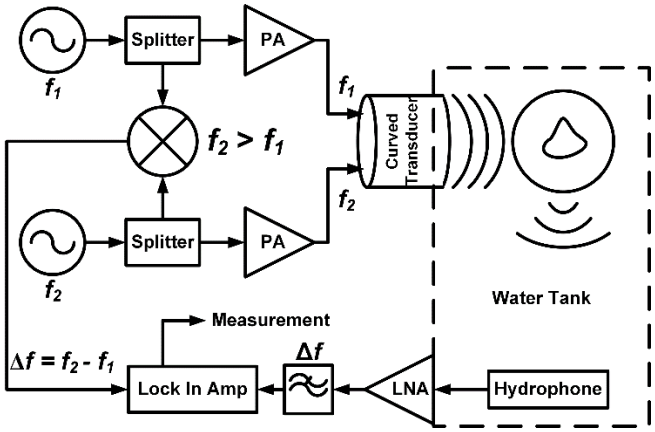


**Figure 4**: Block diagram of the vibroacoustography system. $f_1$ and $f_2$ represent the two ultrasonic tone generators, PAs represent the power amplifiers that are used to amplify the input signal into the curved confocal transducer, LNA signifies low noise amplifier that is used to amplify the input signal of the hydrophone. The target is interrogated by a radiation force in the water tank and the acoustic emission (in low kHz) generated by the target is collected by a nearby sensitive acoustic hydrophone.

The focused beams from the curved transducers are mechanically scanned over the surface of the target at $\Delta f$, and at each point, the peak amplitude of the emission is measured and used to construct an image. Each pixel value is normalized to the peak amplitude during image processing and analysis. This system has been used to image targets in a water bath with sufficient volumetric resolution. Figure 5A represents the assembly of all the aforementioned main electronic components into a portable cart and figure 5B illustrates Acoustic Measuring Tank System (AMS)

(Sonora Inc., Longmont, CO) which allows for system characterization, calibration, development, and tissue mimicking phantoms (TMPs) and *ex vivo* tissue imaging.

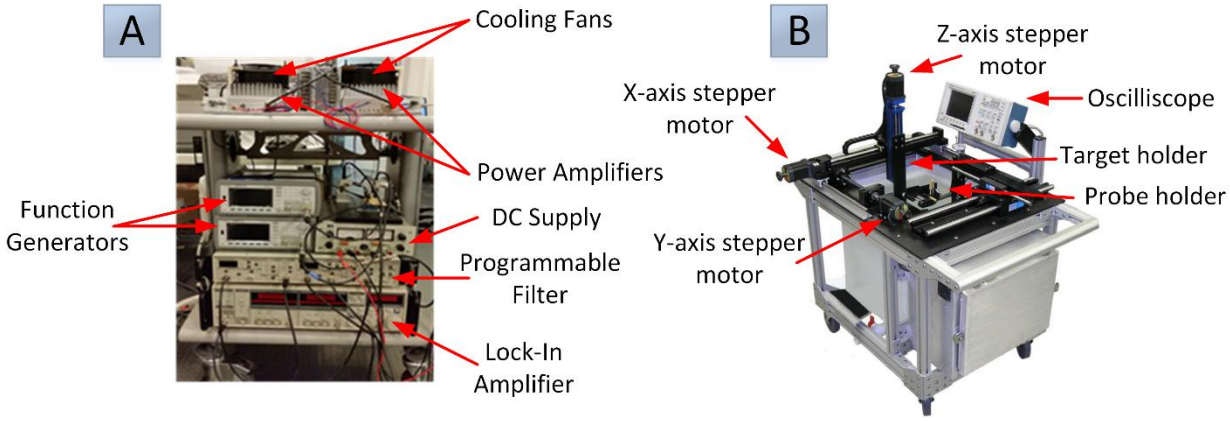


**Figure 5**: A) System receiver with active components. B) AMS Sonora water tank used for system characterization and optimization as well as tissue mimicking phantom imaging.

Moreover, the AMS is a test system consisting of hardware and software designed to measure the acoustic energy emitted from targets inside the tank. The test system utilizes a Three Axis Stepper Motor control to position the hydrophone relative to the device under test (acoustic source), but for our case, since the hydrophone is larger than the standard size, we developed our own mount presented in figure 6. The hydrophone output is sampled and digitized by a Lock-in Amplifier (SRS 844, Stanford Research Systems Inc., Sunnyvale, CA) and recorded to a personal computer via a GPIB-IEEE488 communications line.

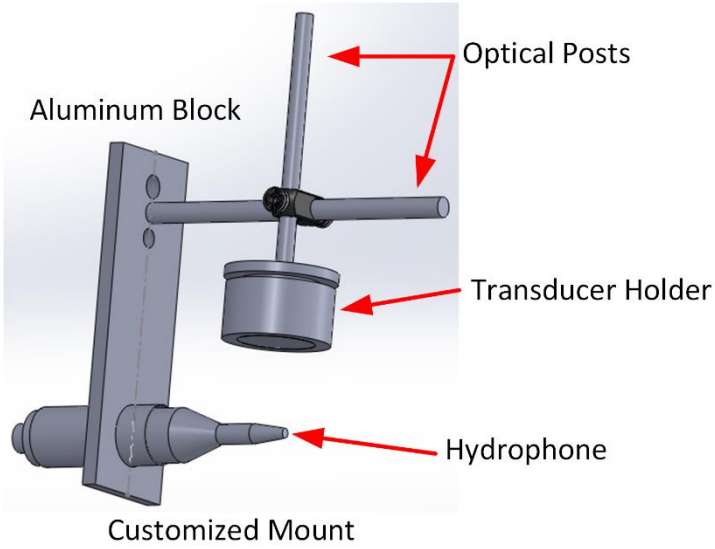


**Figure 6**: Customized mount for our transducer and hydrophone. The transducer aluminum housing is held in place by ½″optical posts and is free to rotate by a right angle clamp (Thorlabs, Newton, NJ). Both hydrophone and transducer are connected to an aluminum block that are screwed into the probe holder of the AMS tank.

### 2.1.1. Transducer

The transducer was assembled and etched using high coupling coefficient piezoelectric half-dome ceramics Navy Type VI (PZT-5A) (Boston Piezo-Optics Bellingham, MA) The radius of curvature (ROC) of approximately 6 cm was used to focus the acoustic waves onto the target. The following table illustrates the specific details about the transducer:

**Table 1**: Confocal transducer specifics. It highlights the longitudinal velocity, $d_{33}$ piezoelectric charge constant, $g_{33}$ piezoelectric voltage constant, density, center frequency, and acoustic impedance.

| Piezoelectrics | Longitudinal Velocity (cm/μSec) | $d_{33}$ $10^{-12}$(C/N) | $g_{33}$ $10^{-3}$(Vm/N) | Density (g/cm$^3$) | Acoustic Impedence (g/cm$^3$.Sec)x$10^5$ | Center Frequency (MHz) |
|---|---|---|---|---|---|---|
| Lead Zirconate Titanate (PZT)-5A | 0.44 | 380 | 24.8 | 7.75 | 33.7 | ~ 3.0 MHz |

The confocal transducer is constructed by dividing the back electrode of the piezoelectric ceramic into an inner and outer ring, such that the elements have identical beam axes and focal lengths. The diameter and the area of the inner element are ~ 28.5 mm and ~ 650 mm$^2$, respectively, the outer elements are ~ 45.0 mm and ~ 890 mm$^2$, respectively, and the focal distance is ~ 60 mm.

The f-number of the transducer for the inner and outer elements was calculated as ~ 2.10 for inner and ~1.33 for outer using the following equation:

$$f\ \#= \frac{ROC}{Transducer\ diameter} \tag{2.1}$$

Figure 7 illustrates the described confocal element. The confocal transducer is held in an aluminum housing unit, depicted in Figure 7B, where it holds the element in place for imaging a target in water and to protect circuitry and to seal the element to the casing.

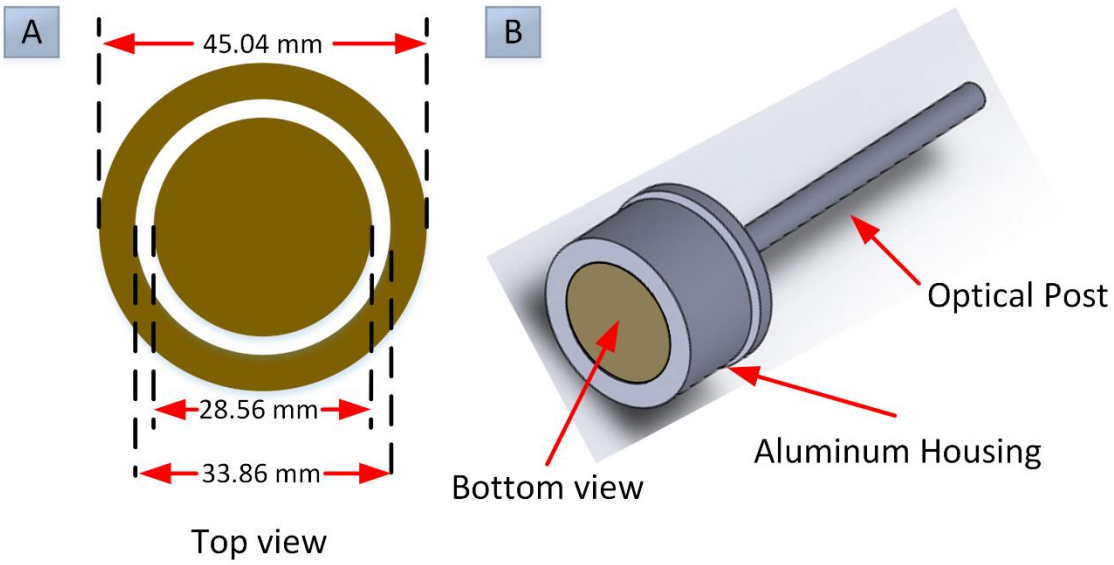


**Figure 7**: A) View of the confocal curved piezoelectric transducer with an inner diameter of ~28.5 mm and outer diameter of ~45 mm. The focal distance is ~60 mm away from the transducer. B) The housing of the element, where light brown represents the bottom face of the transducer, which is used for imaging targets.

## 2.2. Impedance Matching Network

After transducer fabrication, and assembly of the housing and the piezoelectric element, RF power delivery to the transducer became our main focus. Impedance matching networks play a major role in the power transfer between the source, RF power amplifiers, and the load, transducer element. The main goal of this network design is to maximize power transfer while minimizing the loss,

which is due to the impedance mismatch between the load and the source. A poor matching network can eventually reduce the device efficiency and increase the reflection between the two elements. Moreover, the reflected power can cause thermal damage to the amplifier and ultimately can reduce the generated signal from the transducer at its resonating peak [52, 53].

For the design of this network, matching lumped elements such as capacitors, C, and inductors, L, which ideally do not dissipate energy, were used. As shown by Bode-Fano Criterion, return loss (RL) and bandwidth are inversely proportional, so there is a tradeoff between the two quantities. Since we are focusing on single frequency and are not doing a frequency-sweep for majority of our experiments, we designed a network with a small bandwidth that covered the center frequency of the element with a return loss (RL) of at least 15 dB where Γ represents the reflection coefficient.

$$\Gamma = \frac{Z_L - Z_S}{Z_L + Z_S} \tag{2.2}$$

where $Z_L$ represents the impedance of the load, transducer in this case, and $Z_S$ represents the impedance of the source, power amplifiers. Quality factor or Q-factor is inversely proportional to the bandwidth of the designed network and because we only need to cover a narrow bandwidth, we designed a high Q circuit:

$$RL\ (dB) = -20 \log_{10}|\Gamma| \tag{2.3}$$

To start, scattering parameters (S-parameters) that describe the electrical behavior of linear networks when undergoing steady state supply of the load, transducer, were acquired using a Vector Network Analyzer (VNA) (HP 3577B Hewlett Packard Company Everett, Washington). The measured S-parameters were used to generate a matching network between the power amplifiers that have an impedance of 50 Ω and the confocal transducer, a capacitive load AWR Microwave Office CAD software was used to design the matching network. Figure 8 shows the S-

parameters for the inner and outer confocal transducer plotted on a Smith chart using AWR software.

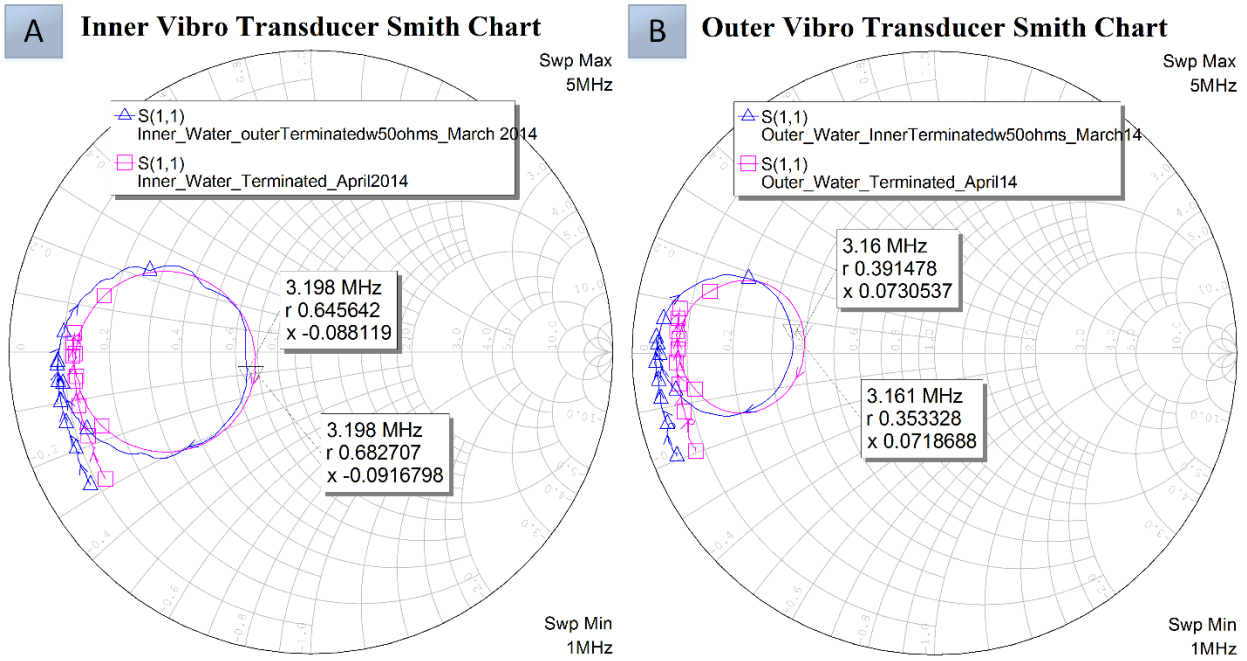


**Figure 8**: Confocal transducer S-parameters in water terminated with 50Ω graphed on the AWR software. A) Represents the inner element at center frequency of 3.198 MHz with return loss of ~16 dB. B) Represents the outer element at center frequency of 3.16 MHz with return loss of ~8 dB. For each element, two measurements, blue and pink were taken in two consecutive months to certify the elements' acoustic performance.

As shown in figure 8, the inner transducer at 3.198 MHz, intended center frequency, had a return loss of ~16 dB, so no matching network was needed for the inner transducer element. However, for the outer transducer, since the return loss was low, ~8dB, a matching network was designed, fabricated, and tested. Coplanar waveguide with ground (CPWG) transmission line was used for this purpose. It was fabricated using printed circuit board (PCB) technology that consisted of a single conducting track with a pair of ground planes on either side of the track printed onto a dielectric substrate at the same side, hence coplanar. The back side ground of the PCB was connected to the top side ground planes [54]. The follow diagram, figure 9, illustrates the network that was designed.

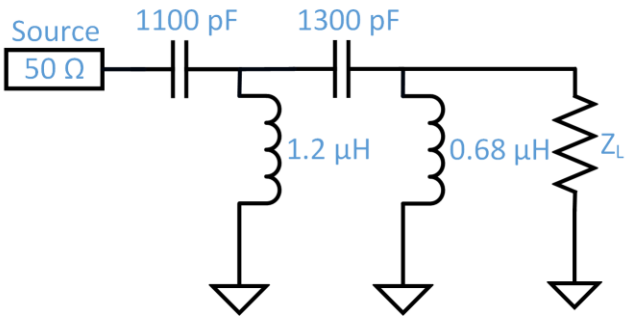


**Figure 9**: Designed CPWG matching network for the outer transducer at center frequency of 3.16 MHz. A series of capacitors and shunt inductors were used to increase the power transfer between the 50Ω source, power amplifier, and the load, confocal transducer inner portion, with unknown impedance "capacitive load".

After network fabrication, it was tested with the load on VNA to validate the return loss. Figure 10 represents the S-parameters of the outer transducer, with matching network in place, graphed in the AWR Microwave Office. As shown, the return loss, increased from ~8 dB to ~22 dB with a bandwidth of ~40 kHz centered at the center frequency, 3.16 MHz.

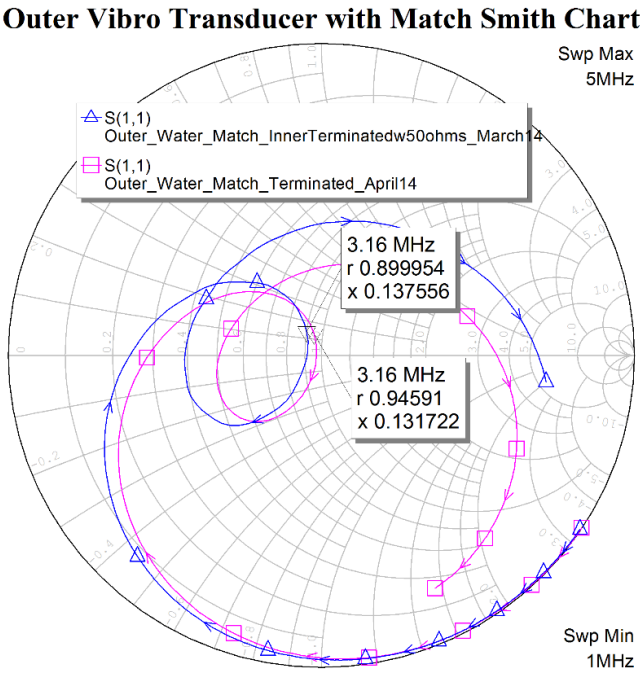


**Figure 10**: Outer transducer's S-parameters in water with matching network terminated with 50Ω are graphed using the AWR software. It represents the outer element at center frequency of 3.16 MHz with return loss of ~22 dB with two measurements, blue and pink, that were taken in two consecutive months to certify the element's acoustic performance.

## 2.3. Beam Pattern Characterization

After evaluations and optimization of the operating parameters for the electronics and key components of the VA system, including the matching network, the confocal transducer acoustic output was evaluated to check the alignment of the two ultrasonic tones in the focus region. In order to assess the acoustic output performance of the transducer, the piezoelectric element was tested in the AMS acoustic tank with a needle hydrophone (Onda HNR-1000 Sunnyvale, CA) for each individual tone from either element in the MHz range, and a low kHz hydrophone (TC4014-5, Teledyne Reson Inc. Goleta, CA) for both tones when they mix at the focal point. The needle and the Reson hydrophones were placed in the focus plane of the transducer, ~ 60 mm away, and mechanically scanned the plane to assess the acoustic performance of both inner and outer transducer laterally in the X and Y axes. As for the Z-axis, only the needle hydrophone was used in the focus plane and scanned multiple Z-planes in the same X and Y location to assess the sharpness of the focus field in the axial orientation. As shown in figure 11A and 11B, the difference between inner and outer transducer beam profiles in both X and Y axes was ~ 0.5 mm, confirming a close match between the two portions of the element. In particular, when individual beam patterns were compared to both elements, Y-axis had a better alignment than the X-axis. Full Width Half Maximum (FWHM) of beam profiles for both X and Y axes were ~ 1.0 mm, confirming the sharpness of the peaks. As illustrated in figure 11C, the difference between inner and outer beam profiles was ~ 1.0 mm in the Z-axis. Since the needle hydrophone was calibrated for 1-10 MHz signal range, it did not detect any signal when both portions were on. Overall, this characterization illustrated that the transducer was fabricated properly and is ready for future experiments.

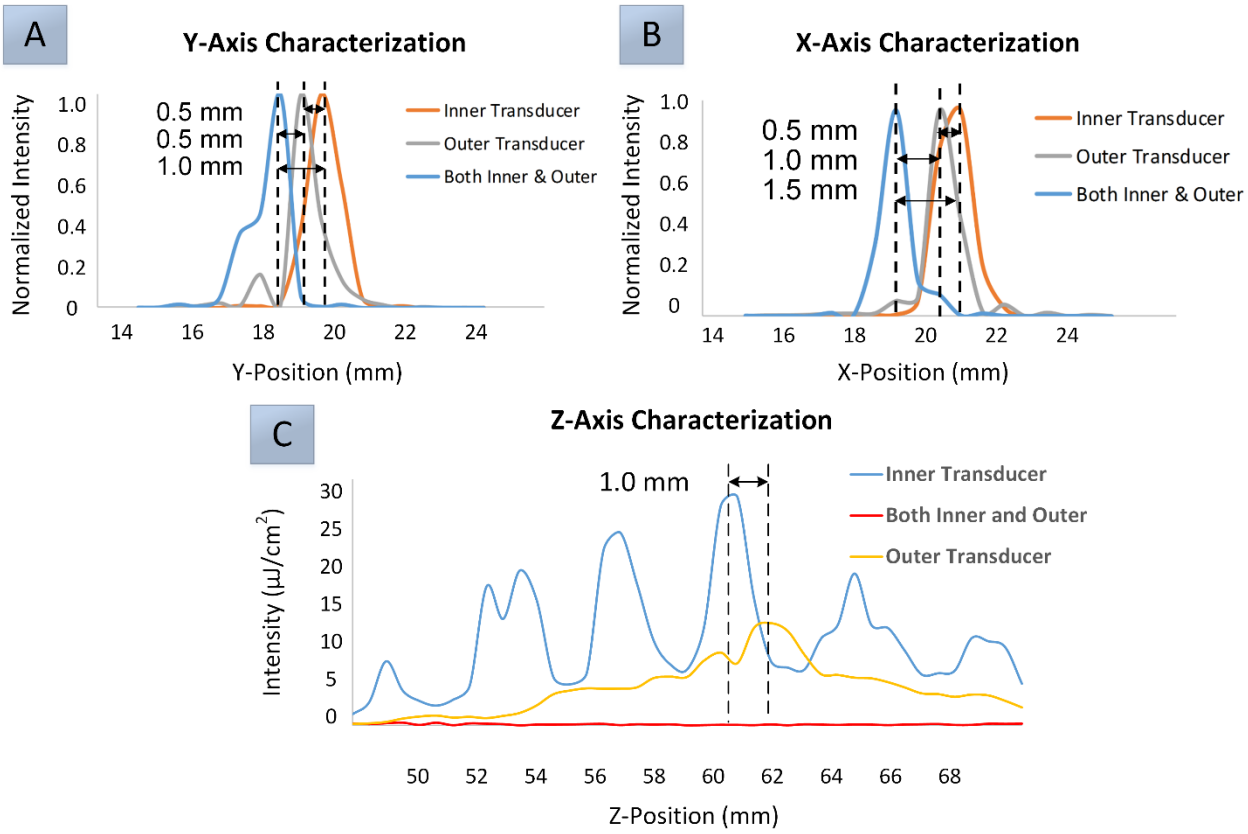


**Figure 11:** 1-D beam pattern profile of the confocal transducer in X (A), Y (B), and Z (C) axes. For each axis, inner, outer, and both beam profiles were assessed to detect misalignment between the two portions of the element. The dotted lines represent the center for each peak and evaluates the alignment in each axes between inner, outer, and both transducers.

## 2.4. Depth of Field Evaluation

After acoustic evaluation of the confocal transducer, the depth of focus was assessed. Objects (fishing weights) with various dimensions held by a fishing line (~ 1mm thick) were placed in a sample holder into the AMS acoustic tank to be imaged using our developed VA system at $\Delta f$=38 kHz. Figure 12 represents a visible image of the 5 fishing weights with various dimensions held by a series of fishing lines in a custom mount sample holder.

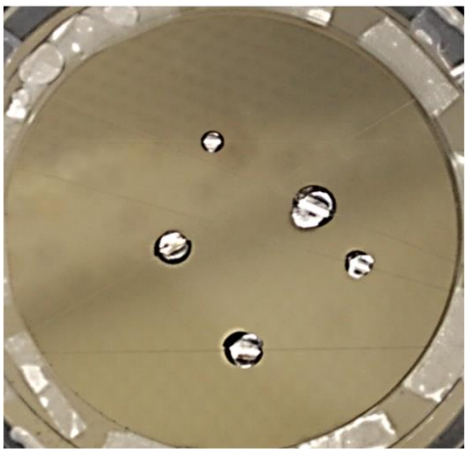

**Figure 12**: Top view of fishing weights held by a series of fishing lines in a sample holder. The fishing weights dimensions from smallest to largest are 4.19/5.38 mm, 4.73/6.00 mm, 6.23/7.97 mm, 6.88/8.71 mm, 8.17/9.79 mm. Since fishing weights change width as they increase in height, the first numbers represent the top width and the second numbers represent the bottom width.

After placing the sample holder in the imaging plane, the fishing weights were imaged using our VA system at the focus plane, 4 mm on top, and 4 mm on the bottom of the focus plane in an area of 60 x 60 $mm^2$. The generated amplitude was extracted from the sample's emitted acoustic waves and was graphed with respect to position in the X and Y axes. Following these graphs, Fast Fourier Transform (FFT) of these images was calculated and graphed vs. position to assess the images and determine the sharpest image among the three. Figure 13 represents the VA amplitude images (top) and FFT images (bottom) of the fishing weights. As shown, the sharpest image from the VA amplitude images and the most detailed one from the FFT images of the fishing weights were collected at the focus plane, as expected. Moreover, the fishing lines that held the weights in place were more apparent in the middle image (the focus plane) confirming our deduction about the focus plane. However, the out of focus plane images illustrated all 5 objects and showed sufficient SNR in the VA amplitude images and in some cases, the fishing lines were clear enough to be picked up from the background. Overall, this evaluation showed that the depth of focus of the fabricated transducer is as expected and can demonstrate sufficient depth to image targets with embedded objects that are at least 8 mm thick for future experimentations.

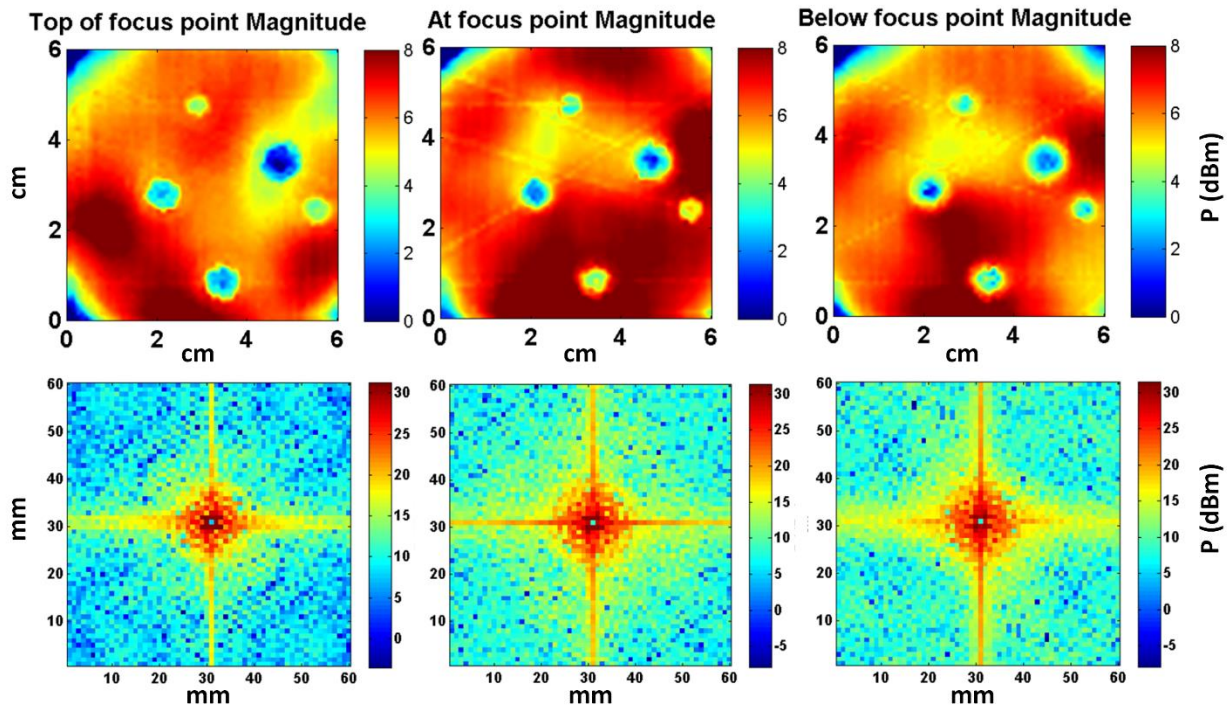


**Figure 13**: VA amplitude images (top) and FFT calculated plots (bottom) of three imaging planes: top of the focus plane, focus plane, and bottom of focus plane are graphed. As illustrated by the VA amplitude images, the sharpest image occurs at the focus plane and also the most detailed image occurs at the focus plane in the FFT calculated graphs.

## 2.5. Vibroacoustography Feasibility Experiment with Tissue Substrate

In the absence of an imaging technique that can image diseased tissue with high diagnostic accuracy and contrast, surgeons must often excise excess healthy tissue surrounding neoplasms to ensure complete removal of malignant tissues. Additional approaches that are commonly used in the detection of tumor regions include palpation and conventional ultrasound to locate the affected area. However, these techniques suffer from limitations such as minimal specificity and lack of depth penetration. Lack of specificity results in the production of unclear diseased tissue regions, and therefore fails to offer surgeons a reliable and accurate image guidance tool. We demonstrate selective imaging using phantom tissue samples of polyvinyl alcohol that are altered and arranged into unique geometries of varying elastic topology and percent-by-weight (%wt) to assess the feasibility of our generated vibroacoustography system. Determining the precision and sensitivity

of the VA imaging system in identifying boundary regions as well as intensity ranges associated with tissue phantom targets will provide additional important information to allow for a non-invasive tool to distinguish diseased tissues from normal tissues in an *in vivo* setting.

### 2.5.1. Background

Due to locoregional recurrence and a high incidence of metastases, patient outcomes in Head and Neck Squamous Cell Carcinoma (HNSCC) depend heavily on complete surgical resection with negative margins [55]. However, a significant challenge in surgical treatment is the difficulty in selective excision of malignant cells while minimizing damage to healthy tissue. Thus, there is a pressing need for the use of real-time, high-resolution imaging to accurately differentiate between benign and malignant tissues beyond the capacity of manual palpation. Palpation is the sole intra-operative technique that surgical oncologists rely on to assess the region of interest. In palpation, a static force is exerted on the tissue and tissue elasticity estimation and comparison is determined by a physician. This technique suffers from major limitations, including lack of depth penetration and sensitivity. Other approaches, such as conventional ultrasound, are used to investigate malignancies; however, they are limited by low resolution and lack of depth penetration within the region of interest. VA, a relatively new imaging modality that creates images solely based on the viscoelastic properties of the tissue, has been developed and investigated to overcome these aforementioned challenges [16, 34]. In this section, a feasibility study was performed to report the use of vibroacoustography (VA) as an imaging modality dependent on the elastic profile, one of the fundamental aspects of mechanical properties, of targets. Raster-scanning of samples with a low kHz VA beam and recording the amplitude of their resonant acoustic emissions resulted in data relating to tissue elastic composition at sub-mm resolution. Phantom tissue samples of polyvinyl alcohol that were modified and arranged into unique geometries of varying percent mass

concentration were utilized. Given tissue elastic properties, VA imaging demonstrates potential in generating an acoustic profile of tissue specimens *in vivo* to guide margin selection by surgical oncologists in clinical settings.

### 2.5.2. Methods and Materials

The VA setup consisted of a confocal transducer, as mentioned in previous sections, that emits ultrasound waves at two distinct low MHz frequencies to produce a focused ultrasound beam of $\Delta f$ = 38 kHz to irradiate the sample at one particular Z-plane. An acoustic hydrophone is then used to receive the acoustic emission, generated by the irradiated sample, and feed it to a computer for signal processing. The VA system raster scans the sample that is mounted in the water tank at a particular Z-plane at 500 µm step size. The acoustic emissions, based on the object's viscoelastic properties, generated by the sample are used to reconstruct an image. After assembling the system, this experiment was used to validate the developed system in imaging phantoms. The $\Delta f$ for this experiment was set at 38 kHz primarily due to our system's electronic components, the transducer, and also based on literature findings in tissue mimicking phantoms, which will be elaborated on in future sections and *ex vivo* human cancer specimens [33].

#### 2.5.2.1. Tissue Substrate Preparation

Polyvinyl Alcohol, PVA, gels were introduced as photoacoustic phantoms by Kharine *et al.* and are used by many acoustic groups for photoacoustic imaging and elasticity measurements [56-58]. An aqueous solution of 5% and 13% PVA is obtained by dissolving PVA powder in deionized (D.I.) water at 95 $^{o}$C with continuous stirring to maintain a homogeneous solution. After degassing the solution in a vacuum chamber, the solution was poured into a mold and held at -20 $^{o}$C for 12 hours to congeal [33, 35, 56].

### 2.5.3. Results and Discussion

PVA samples of elastic properties comparable to that of native tissue were imaged and analyzed using the VA system. Figure 11 illustrates a visible as well as a VA image of a 5% PVA prism phantom. As shown in the figure, the phantom has an enhanced boundary region that clearly distinguishes it from its surrounding area. The image also shows the phantom is characterized by a higher acoustic response as compared to the surrounding area, DI water, based on the power level measurements from the VA image color bar. For registering the generated VA image to the visible image, fiducial markers (*i.e.* geometry of the targets) relating visible to VA images, were utilized. For this process, a series of steps were followed in order to register the VA image to the visible image. First the phantom was photographed in the tank, *in situ* phantom. The phantom was then imaged using the VA system, vibro phantom. After that, *in situ* phantom was registered to vibro phantom using fiducial marker, the asymmetries of the actual phantom.

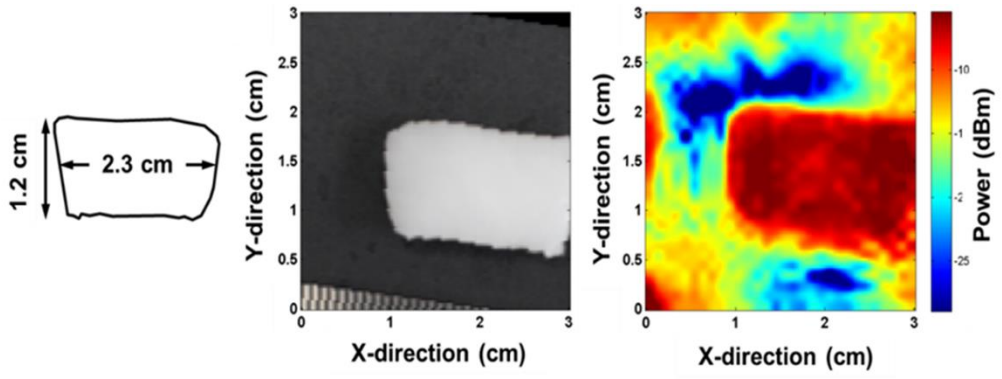


**Figure 14**: Diagram (left), Visible (center), and VA (right) images of a 5% PVA phantom prism. The phantom illustrates clear delineation of its boundary with respect to the surrounding media.

After establishing the system's feasibility in imaging simple phantoms, embedded phantoms composing of multiple smaller ones implanted into a larger phantom were imaged to investigate the sensitivity of our imaging system in imaging embedded objects. Figure 12 depicts a visible image of three 5% prisms and one 5% cylinder into a 13% PVA cylinder phantom and its

corresponding VA image. In this figure, the outline of the 5% prisms can be differentiated from the 13% cylinder background phantom. However, thee prisms and middle cylinder illustrate different intensity due to their z-plane location within the main phantom and thus they cannot be clearly distinguished from the background. Moreover, the background noise will need to be identified and minimized for future imaging trials which will be discussed in following sections.

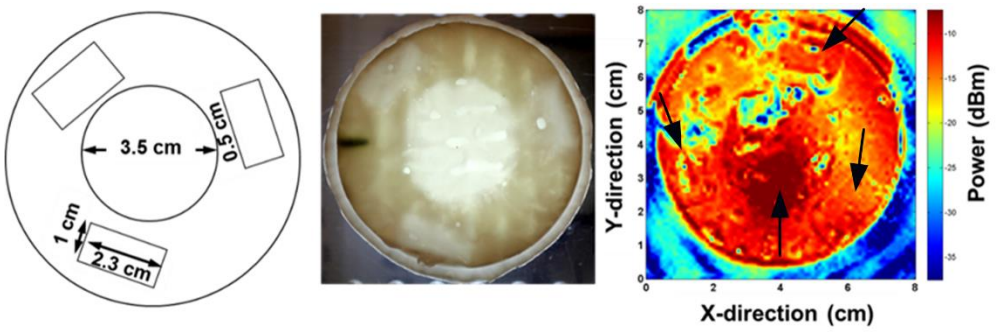


**Figure 15**: Diagram (left), visible (center), and VA (right) images of three 5% PVA prism and one 5% cylinder embedded into a 13% cylinder mold that enhances the 3 prisms and 1 cylinder boundary regions relative to the surrounding media.

### 2.5.4. Conclusion

This feasibility experiment with PVA phantoms demonstrated the capability of our developed vibroacoustography system in imaging soft targets and embedded phantoms, based on inherent viscoelastic properties of the materials. However, further development and advancement, which will be discussed in the next chapters, are necessary to produce high contrast, high resolution images of targets for non-invasive detection of the boundary between malignant and normal tissues for intra-operative applications. This experiment offered insight for the development of our imaging system for imaging *ex vivo* human tissues, such as oral cavity cancers. Additionally, this experiment can be used to optimize system parameters and increase contrast for generated images.

# 3. Characterization of Vibroacoustography System Parameters

In this chapter, we will characterize our developed vibroacoustography system parameters. We evaluate the generated acoustic emission by examining the point spread function (PSF), modulation transfer function (MTF) in tissue substrates. We also analyze the lateral and axial resolution as well as sensitivity and specificity of this technique with tissue substrates that mimic acoustic properties of human tissues, tissue mimicking phantom (TMP).

## 3.1. Overview

The increasing need for screening techniques that can non-invasively and accurately evaluate biological tissue has drawn attention to medical imaging modalities such as vibroacoustography (VA) and other tissue characterization techniques. Among acoustic radiation force techniques, VA non-invasively utilizes tissue mechanical properties to generate native, pathology-specific image contrast. In this method, VA utilizes two non-destructive radiative forces in the low MHz range to produce an acoustic wave in the low kHz range. This resulting low frequency force perturbs the target, and as a result, the target responds by producing emissive waves as a function of its mechanical properties and is detected by a nearby sensitive hydrophone to form an image of the target. The aim of this chapter is to evaluate the sensitivity and resolution limits of our system in pre-clinical targets, specifically TMPs. Lateral and axial resolution, as well as material characterization, studies were performed in isotropic two-layered and multiple-layer TMP targets. The resolution studies resulted in ~1 mm lateral and ~12 mm axial which were confirmed and validated by the theory for a confocal transducer geometry. Our VA system showed to be sensitive enough to detect regions with stiffness difference of at least 10 kPa and lateral width of at least 4 mm. This result, coupled with high imaging contrast, further supports VA as an emerging method with potential applications in *in vivo* medical imaging and tissue assessment.

## 3.2. Background

Changes in elasticity of soft tissues are closely related to tissue pathology. However, estimation of this mechanical parameter for tissue characterization remains difficult in clinical practice. Palpation, the traditional method by which a physician uses touch to sense differences in elasticity between suspicious tissue and normal tissue, requires considerable clinical expertise and is very difficult to assess when deeper tissues are involved [9]. Early, intra-operative detection and characterization of potential tissue lesions, therefore, specifically calls for more accurate and sensitive diagnostic tools.

In recent years, ultrasonography, a quantitative method that measures acoustic wave scattering and impedance differences in tissue, has extensively been used to image and resolve the depth of soft tissue malignancies [13, 59]. However, sufficient visualization of lesions for surgical resection can only be provided by ultrasonography when knowledge of the lesion's location and tissue properties is available. Moreover, ultrasonography generally underestimates the size of the tumor, which precludes the use of this technology in cases where the tumor tends to be smaller, well-differentiated and less palpable [13, 16, 22].

Adjunct imaging methods, such as shear-wave elastography (SWE) and optical coherence tomography (OCT), offer high image contrast and resolution as described in the previous sections, but possess their own limitations [14]. In SWE, MRI essentially maps the spatial distribution of the resulting displacement in the target; however, it measures an absolute physical parameter (*i.e.* stiffness) of the target which further limits its image contrast to similar, proximal tissues [36, 59]. OCT has similarly been used to investigate soft tissues properties and provides spatially resolved information about targeted tissue [60, 61]. Due to light scattering and attenuation, the depth of penetration and field of view (FOV) of OCT are limited [61]. Additionally, the need for prior

knowledge of the target makes standard clinical use of OCT difficult.

Early evidence suggests that VA, a non-invasive imaging technique, could be used to characterize tissue and potentially guide intra-operative tumor excision procedures. VA is a relatively new, real-time imaging technique that maps the mechanical response of tissue subjected to a focused acoustic radiation force [16, 42]. Unlike SWE, which applies mechanical waves to the entire surface of the target, VA *locally* perturbs specific regions of the tissue. VA further reduces complex interference patterns and depth of penetration-related issues, lending this technique as an ideal tool for soft tissue examination [22, 62]. In comparison to palpation, the transverse spatial resolution of VA is reported to lie in the sub-millimeter range and the axial resolution (*i.e.* slice thickness) is in the sub-centimeter range [41]. VA, therefore, is better suited for high resolution detection of tumors during intra-operative imaging procedures [16, 42].

Herein, we evaluate the sensitivity and resolution performance limits of a VA system in two-layered and multiple-layered TMPs for sensitivity and specificity limits, and a TMP with an embedded bead for resolution limits. Line pair phantoms composed of agar and gelatin, n = 1 for each experiment, were imaged to generate the point spread function (PSF) and sensitivity of the VA system. These results may further support VA as an accurate and sensitive tool for *in vivo* tumor boundary detection during intra-operative surgical procedures.

## 3.3. Systems and Methods

### 3.3.1. Vibroacoustography System

Vibroacoustography generates a map of the mechanical response of a target to a dynamic radiation force. In response to the applied oscillating force, the object vibrates and produces an acoustic emissions field at the difference frequency ($\Delta f$ ). This emissive wave is collected from the object

using a highly sensitive acoustic hydrophone. An image is created of the spatially varying signal amplitude and phase of the target by scanning the focused beam spot over the object [16, 33, 41].

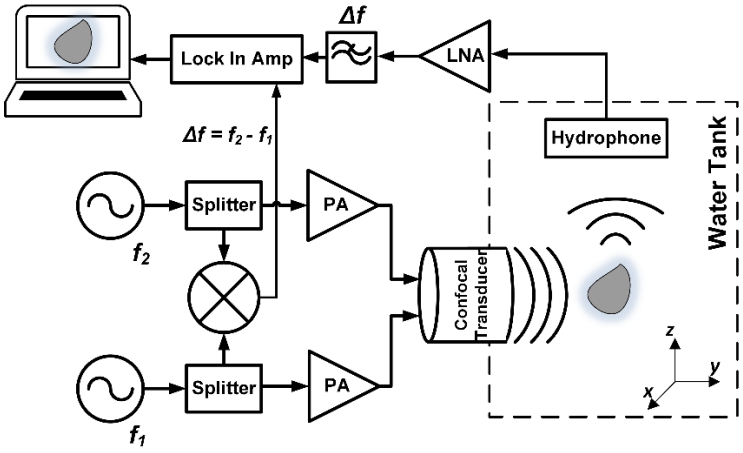


**Figure 16**: A block diagram of the vibroacoustography (VA) system. The object is vibrated by an acoustic force and the acoustic emission (in low kHz) generated by the object is collected by a nearby sensitive acoustic hydrophone.

Two function generators were used to generate 3.16 MHz and 3.198 MHz tones and were combined using a 3dB splitter (Minicircuits, Inc. Brooklyn, NY). Half of the signal was amplified using power amplifiers (PA) (AR Modular, Inc. Bothell, WA), while the other half was fed into a mixer (Minicircuits, Inc. Brooklyn, NY) to be used as the reference signal for the Lock-in Amplifier (SRS 844, Stanford Research Systems, Inc. Sunnyvale, CA). The generated acoustic emission signal was detected using a highly sensitive hydrophone (TC4014-5, Teledyne Reson Inc. Goleta, CA) in AMS ultrasonic testing water tank that coupled the generated acoustic waves from the transducer to the object, and the emitted acoustic waves from the object to the hydrophone. The output of the hydrophone was directed into a Low noise amplifier (LNA), programmable filter (SRS 650, Stanford Research Systems, Inc. Sunnyvale, CA), and a Lock-in Amplifier (SRS 844, Stanford Research Systems, Inc. Sunnyvale, CA) to detect the peak amplitude and phase difference of the frequency emission.

### 3.3.2. Confocal Transducer

The focused beams from the curved confocal transducer as discussed in previous sections, with a radius of curvature (ROC) of ~60 mm, interferes at a focal region placed on the target. The two elements are excited with two slightly different frequencies of $f_0$ = 3.16 MHz and $f_0 + \Delta f$ = 3.198 MHz, in continuous wave (CW) form. Using derivations shown by Chen *et al.* [62], the pressure field along the Z-axis is modeled by:

$$\mathrm{p(z,t)} = \mathrm{P_1(z)\cos\left(2\pi f_1 t + \varphi_{21}(z)\right) + P_2(z)\cos\left(2\pi f_2 t + \varphi_{22}(z)\right)} \quad (3.1)$$

where

$$P_1(z) = Zu_0 \frac{R}{|z|}\left|1 - \exp\left(\frac{j\pi a_1^2}{\lambda_1 R}\cdot\frac{z}{z+R}\right)\right| \quad (3.2)$$

and

$$P_2(z) = Zu_0 \frac{R}{|z|}\left|1 - \exp\left(\frac{j\pi a_{21}^2}{\lambda_2 R}\cdot\frac{z}{z+R}\right) - \exp\left(\frac{j\pi a_{22}^2}{\lambda_2 R}\cdot\frac{z}{z+R}\right)\right| \quad (3.3)$$

$P_1(z)$ and $P_2(z)$ are amplitude functions, and $f_1$ and $f_2$ are frequencies. $Z = \rho c$ is the acoustic impedance, where $\rho$ and $c$ are the density and propagation speed, respectively. $\lambda_1$ and $\lambda_2$ are ultrasound wavelengths, $u_0$ is the amplitude of the particle velocity at the transducer surface, and $a$ is the transducer radius. $\varphi_{21}(z)$ and $\varphi_{22}(z)$ are phase functions, and $R$ is the ROC. The beam was raster scanned over the target surface at $\Delta f$ = 38 kHz. At each point, the peak amplitude and the phase of the emission were measured and used to generate an image. Each pixel value in the image is mapped to a maximum value of the peak amplitude and phase difference. The scanning resolution in the AMS water tank is 0.04 mm for the lateral scan (X and Y axes) and 2.0 mm for the axial scan for the first part of the study. The oscillatory radiation force on a point target at $(x_0, y_0)$ on the focal plane is given by equation 3.4 and the oscillatory radiation force on a unit target at $z_0$ on the transducer axis is illustrated by equation 3.5.

$$F_{\Delta\omega}(x_0, y_0) = \frac{1}{c^2\rho} P_1(r_0) P_2(r_0)\, cos(\Delta\omega t + \varphi_{12} - \varphi_{11}) =$$

$$\frac{\rho u_0^2 \pi^2 a_1^2}{\lambda_1 \lambda_2 R^2} jinc\left(\frac{r_0 a_1}{\lambda_1 R}\right)\left[a_{22}^2 . jinc\left(\frac{r_0 a_{22}}{\lambda_2 R}\right) - a_{21}^2 jinc\left(\frac{r_0 a_{21}}{\lambda_2 R}\right)\right] cos(\Delta\omega t + \varphi_{12} - \varphi_{11}) \quad (3.4)$$

$$F_{\Delta\omega}(z_0) = \rho u_0^2 \frac{R^2}{z_0^2}\left|1 - \exp\left(\frac{j\pi a_1^2}{\lambda_1 R} . \frac{z_0}{z_0 + R}\right)\right| x \left|1 - \exp\left(\frac{j\pi a_{21}^2}{\lambda_2 R} . \frac{z_0}{z_0 + R}\right) - \right.$$

$$\left. \exp\left(\frac{j\pi a_{22}^2}{\lambda_2 R} . \frac{z_0}{z_0 + R}\right)\right| \cos(\Delta\omega t + \varphi_{22} - \varphi_{21}) \quad (3.5)$$

### 3.3.3. Image Generation

#### 3.3.3.1. Point Spread Function

Imaging systems are typically characterized by resolution performance limits, which can be studied through the point spread function (PSF) and modulation transfer function (MTF). PSF relates a generated image of a target to its physical (*i.e.* actual) appearance. Image formation in VA is based on the acoustic emission of the target in response to a radiation force perturbation. The emission is a function of the dynamic component of the radiation force and the object's physical characteristics, such as size, shape, mechanical properties, and geometry [16, 49, 63]. To calculate the PSF of our developed VA system, we consider a point source with a unit mechanical response at position ($x_0$,$y_0$), analogous to an impulse response in the XY plane. A point source is used because it is represented in a single pixel as an "ideal" image. However, using our system, it will be portrayed as more than one pixel, a "real" image. We define the PSF of the imaging system as:

$$g(x, y) = h(x, y) * f(x_0, y_0) \quad (3.6)$$

where $g(x, y)$ is the output image, and $h(x, y)$ is the PSF convolved with $f(x_0, y_0)$, the input object.

#### 3.3.3.2. Modulation Transfer Function

Modulation transfer function (MTF) is another way to measure the frequency response of the system and provide the spatial resolution response of an imaging system. MTF demonstrates the system's ability to transfer contrast to a resolution from the target to its image. Moreover, MTF is another way to incorporate resolution and contrast into a single parameter. While PSF represents system performance in the spatial domain, MTF represents it in the frequency domain. They can further be related by the Fourier transform:

$$MTF = \mathcal{F}(PSF) \tag{3.7}$$

where $\mathcal{F}$ represents the Fourier transform.

### 3.3.4. Image Acquisition

For image acquisition, a Lock-in Amplifier (SRS 844, Stanford Research Systems, Inc. Sunnyvale, CA) was used to detect the amplitude and phase of the output acoustic emission from the target, which was collected by the acoustic hydrophone (TC4014-5, Teledyne Reson Inc. Goleta, CA) and filtered with a programmable filter (SRS 650, Stanford Research Systems, Inc. Sunnyvale, CA). The point source target used for the first part of our resolution testing was a 1 mm stainless steel bead embedded in a 15% (% weight) gelatin TMP, measuring 20 x 20 x 30 $mm^3$. The phantom was submersed in an Ultrasonic Testing water tank and secured by 4 teflon screws in a sample holder. 15% gelatin was utilized as an accurate analog to human tissue due to the nearly identical acoustic properties between the soft tissue and the TMP [64]. Based on the two ultrasonic frequencies used, the minimum spot size of the VA system is predicted to be slightly larger than 500 µm, which is sufficient to directly measure the PSF [16, 63]. Additionally, the viscoelastic coefficient of stainless steel is high, thus providing efficient conversion from high frequency to difference frequencies [16]. Due to the viscoelastic properties of the sphere, an ideal emissive

signal was detected. Spot sizes, defined as full width half maximum (FWHM) about the peak signal, were calculated from the scans. The bead in the phantom was imaged and its effect on the beam geometry (*i.e.* spot size) was ascertained. A similar set-up was used for the second part of this study: Evaluation of the VA system's sensitivity and specificity in line-pair phantoms.

### 3.3.5. Tissue Mimicking Phantoms

Tissue-mimicking phantoms (TMP) have been used for characterization and calibration of ultrasound (US) imaging systems since the 1960s [65]. They are commonly used to evaluate the performance of ultrasound systems during the development of new ultrasound transducers, systems, and diagnostic techniques. Phantoms are ideal tissue models as they can be constructed with well-defined dimensions and acoustic properties to reduce potential confounding variables during imaging [64]. Moreover, phantoms used for ultrasound imaging modalities possess acoustic properties, such as characteristic acoustic impedance, attenuation, backscattering coefficient, and compressional and shear wave speeds of sound, near those of the mimicked tissue [42, 65, 66].

Agar blocks (Agar, Sigma-Aldrich St. Louis, MO) of differing water/agar concentrations were fabricated. These blocks of agar, containing either 2% or 4% agarose (% weight), were mixed and heated above 90 $^{o}$C to maximize cross-linking between polymers. Increasing the amount of agarose in the mixtures leads to a corresponding increase in the elasticity of the phantom [42]. Gelatin blocks (Porcine Gelatin, Sigma-Aldrich St. Louis, MO) possessing water/gelatin concentrations of either 10% or 20% (% weight) were used as a second type of tissue substrate. To remove air bubbles from the final mixture, each gelatin solution was placed in a centrifuge at a rotation speed of 2 rcf (relative centrifugal force) for a period of 30 seconds. Increasing the gelatin concentration also increases the elasticity of the phantom.

For the evaluation of our system's axial and lateral resolution, a 20 x 20 x 30 $mm^3$ 15% (% weight) gelatin TMP with an embedded 440C grade 24 stainless steel bead (NEMB, Norfolk, CT) with 1mm in diameter was used. The bead was embedded ~9 mm into the gelatin phantom. It was raster scanned in the XY and XZ planes multiple times.

For sensitivity and specificity evaluation of our system, line-pair phantoms were used. Two-layered line-pair phantoms of either agar or gelatin were synthesized to evaluate the ability of our VA system in distinguishing boundary regions in two-layered, isotropic targets. These two-layered line-pair phantoms were created from one type of material (*i.e.* agar or gelatin), but split into two regions of different concentrations with varying widths to simulate proximate, homogeneous tissue regions. 30 x 30 x 30 $mm^3$ phantoms of 1.) 10% and 20% gelatin and 2.) 2% and 4% agar phantoms with n=1 for each experiment were chosen for the first part of this study. These TMP concentrations and types were chosen due to the Elastic Modulus difference between them: 10% and 20% gelatin ~65 kPa, and 2% and 4% agar is ~85 kPa. This difference make these TMPs ideal candidates for sensitivity evaluation of the VA system [42]. Additionally, these particular types of TMPs were synthesized due to their similarity to human soft tissues (*i.e.* prostate, breast, liver, and head and neck) in terms of acoustic properties such as speed of sound, density, and signal attenuation [42] and resulted in mechanical property differences of the same material type that can be distinguished by our VA system [11].

The second part of our study utilized multiple-layered (*i.e.* agar/gelatin) line-pair phantoms of varying layers with n=1 for each experiment to emulate human tissue. The line-pair phantoms were fabricated to investigate the sensitivity and specificity of our developed VA system for future *in vivo* work. To do this, we synthesized multiple-layered phantoms in which regions of agar and gelatin were combined into one phantom. We synthesized one three-layered phantom, 35x35x35

$mm^3$, with a region of 2% agar sandwiched between two regions of 10% gelatin and 15% gelatin with different widths. Additionally, one four-layered phantom, 25x25x25 $mm^3$, with alternating regions of 3% agar and 20% gelatin with different widths, was synthesized. These phantom sizes were chosen to stabilize the structural integrity of the phantom during the synthesis, fabrication, and imaging process.

The elastic modulus difference between 3% agar and 20% gelatin is ~50 kPa, creating distinct viscoelastic contrast, and hence making the four-layered phantom suitable for VA system sensitivity evaluation. The identical regions were chosen to check for system's repeatability and accuracy in detecting regions with identical mechanical parameters. However, the three-layered phantom possesses both high and low differences in Elastic Modulus, which helped capture the full scope of sensitivity detection limits of the VA system. The differences in elastic moduli in the three-layered phantom are as follows: between 10% and 15% gelatin ~ 55 kPa, 15% gelatin and 2% agar ~ 10 kPa, and 10% gelatin and 2% agar ~ 75 kPa [42, 67]. The mentioned concentrations were used to mimic the heterogeneity environment common to *in vivo* settings during intra-operative procedures. The visual representation of the multi-layered phantoms are illustrated in the next section.

## 3.4. Results and Discussions

### 3.4.1. Axial and Lateral Resolution

The VA system's performance in imaging targets and boundaries within the FOV were evaluated. To first assess the resolution of the VA system, we evaluated the normalized transverse amplitude component of the collected signal from the 1 mm diameter stainless steel bead embedded in the 15% gelatin phantom, at $\Delta f$ = 38 kHz. To extract the acoustic signal at this difference frequency from the hydrophone, a programmable bandpass filter, with a bandwidth of 10 kHz, and a Lock-

in Amplifier, with reference signal of 38 kHz, were used. For each raster scan in the AMS water tank a step size of 0.4 mm in the lateral direction and 2 mm in the axial direction were taken and the TMPs were initially positioned 59 mm away from the transducer. MATLAB was utilized to calculate the average dBm value of a 3x3 $mm^2$ square of pixels centered on the bead, corresponding to an area of 1.2x1.2 $mm^2$ in the actual phantom. The larger area was used to avoid any conforming error due to translating stage or phantom movement, resulting from multiple scans in the Ultrasonic Tank.

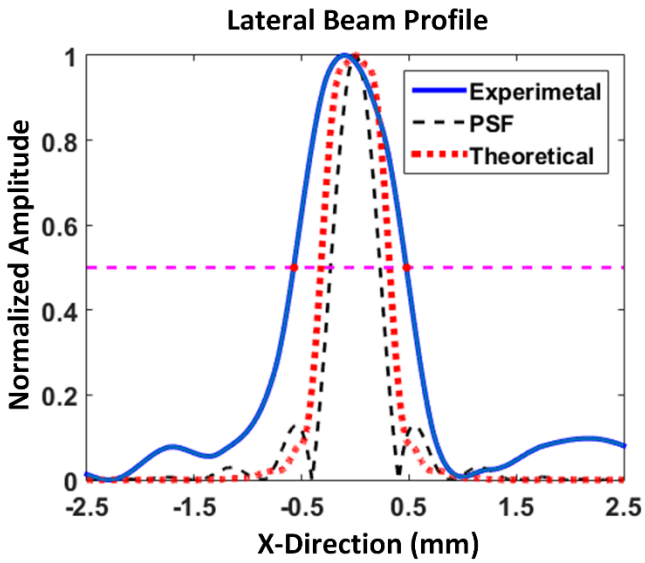


**Figure 17**: Normalized transverse beam profile at $\Delta f$ =38 kHz for a confocal transducer. The blue line represents the experimental PSF beam profile of a 1 mm diameter stainless steel bead embedded in 15% gelatin phantom. The red line and black line represent the theoretical beam profile and the PSF, respectively. The pink dashed line denotes the FWHM of the experimental PSF.

Figure 17 displays the theoretical and experimental results of the lateral beam profile of the transducer's confocal geometry. The dashed line delineates the calculated PSF. Given the curved geometry of the transducer, its stress field is symmetrical about the Z-axis; therefore, only the X-axis profile is verified [62]. In Figure 17, the theoretical curve represents the convolution of the confocal transducer's PSF with an ideal profile (width of 1 mm), which is equivalent to the sphere's diameter. The experimental graph, blue, illustrates the beam profile in x-axis of the same

1 mm diameter of the embedded stainless steel bead and is in good agreement with the theoretical curve of a 1 mm in diameter stainless steel ball. The calculated FWHM suggests that our VA system measured the bead's diameter to be 1.05 mm. The actual and measured value of the bead's diameter are very close, ~4.9% difference, which demonstrates our system's high resolution performance limit.

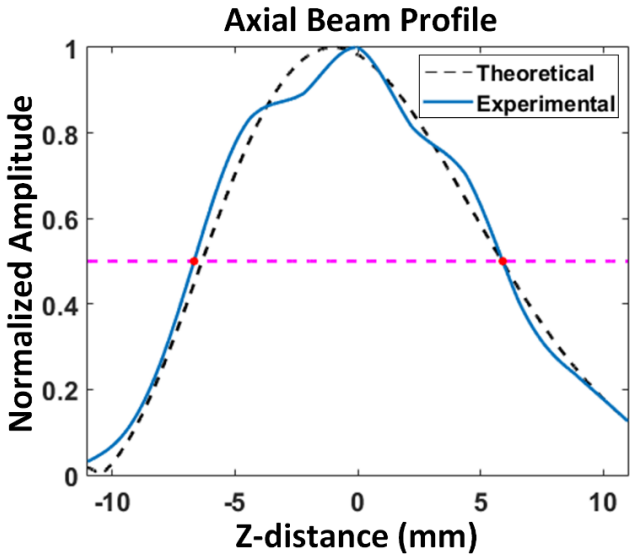


**Figure 18:** Normalized axial beam profile at $\Delta f$ = 38 kHz for a confocal transducer. The blue, solid line represents the experimental axial profile in the z-direction of a 1mm stainless steel ball embedded in 15% gelatin phantom cube. The black dashed line represents its theoretical axial resolution. The pink dashed line denotes the FWHM of the experimental axial beam profile.

Figure 18 presents the normalized amplitude plot of the axial beam profile as a function of axial distance. The calculated axial resolution, illustrated by the black dashed line in figure 18, at FWHM was 12.5 mm, which is very close to the reported literature value of 12.2 mm [62]. Although the lateral profiles were relatively close, the overall axial resolution profile of the intensity field is somewhat different from the theoretical expectation [16, 62]. This deviation can be due to the transducer's construction, such as alignment fabrication errors in the two confocal parts. Another possible source of error can occur from the presence of the transducer's side lobes. In most confocal transducers, beam interference only occurs at the focus region where the two

beams meet. Thus, the length of the focal region and the generation of side lobes can be potential reasons for the discrepancy in the results. Additionally, any signal with the same frequency (*i.e.* mechanical motors on the tank) that falls within the bandwidth of the receiver can cause interference with the collection scheme and may reduce the signal to noise ratio (SNR) [16, 62]. Moreover, another way to interperate the system's resolution performance limit is the modulation transfer function (MTF). As displayed in figure 19, the axial MTF of the experimental plot closely matches that of the theoretical; however, for the lateral profile, the theoretical plot contains more of the signal as the spatial frequncy increases in comparision to the experimental plot.

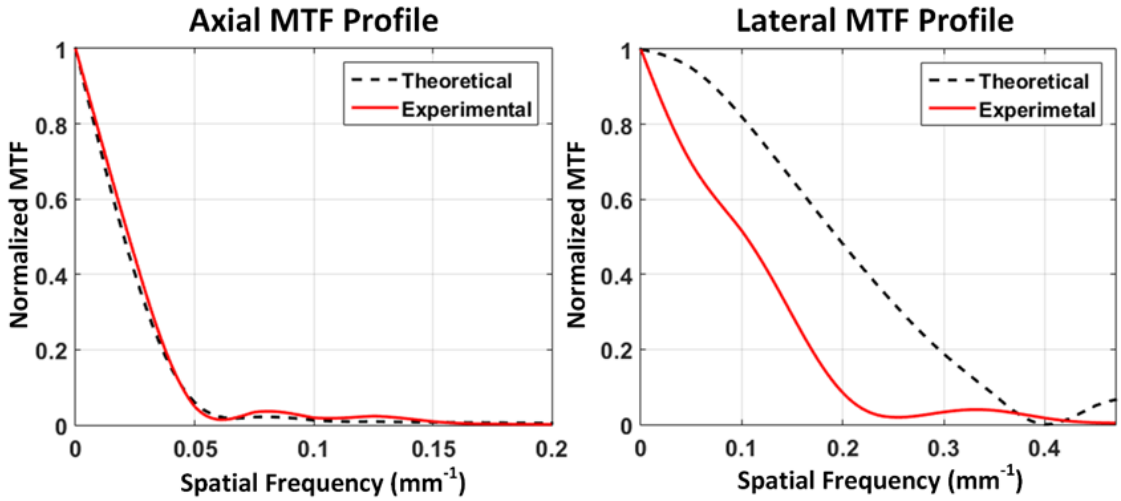


**Figure 19:** Normalized axial (left) and lateral (right) modulation transfer function (MTF) as a function of spatial frequency at $\Delta f$ =38 kHz for a confocal transducer. The black dotted line represents the theoretical MTF beam profile of a 1 mm diameter stainless steel bead embedded in 15% gelatin phantom in both the lateral and axial positions. The red line represents the experimental MTF beam profile.

Since the MTF is typically calculated from the PSF, as the width of the beam profile decreases, the corresponding values in the MTF plot will fall to higher values at the same spatial frequency This is the case when the axial MTF profile is being compared to the lateral MTF profile. The cutoff spatial resolution is usually considered to be the frequency at which the MTF crosses the 10% level [68]. As depicted in Figure 19, the cutoff frequency for the axial MTF profile is ~ 0.045 $mm^{-1}$ for both theoretical and experimental but ~0.34 $mm^{-1}$ for the theoretical and ~0.19 $mm^{-1}$ for

the experimental lateral MTF profile, respectively. For the axial MTF profile, both experimental and theoretical have about the same behavior and cutoff frequency; however, this is not the case of the lateral MTF profile. Since the lateral PSF is much smaller than the axial PSF, the behavior along with the cutoff frequency for the lateral MTF profile between the experimental and theoretical are larger. This is likely a result from the small FWHM in the PSF of lateral direction.

### 3.4.2. Sensitivity and Specificity Evaluation in Two-Layered TMPs

The main goal of this section is to determine the VA system's sensitivity in differentiating regions of varying concentrations of the same material. This VA system has previously been shown to be sensitive and dependent on the mechanical properties of targets [42, 69]. The phantoms in this section were imaged using our VA system with a similar set-up as the previous resolution experiments, but were laterally scanned only in one XY plane in 0.5 mm step size at the focus plane. The average intensity and lateral distance of each region in the two-layered TMPs were calculated using MATLAB. The following tables, 2 and 3, display the average intensity (dBm) and lateral distance (mm), both empirically measured and theoretically calculated, for the two regions in each line-pair phantom. A ruler was used to measure the lateral distance of each region prior to imaging, and the measurements were compared to the VA-measured lateral distance generated using MATLAB.

**Table 2:** Agar two-layered phantoms, possessing one layer of 2% and another of 4%, results are presented. The calculated average intensities (dBm) and lateral displacements (mm), both measured and calculated, are illustrated.

| Line Pair Type | Agar Type Concentration (%) | Average Intensity (dBm) | Measured Lateral Distance (mm) | Calculated Lateral Distance (mm) |
|---|---|---|---|---|
| 15 mm and 15 mm | 2 | -4.78 | 15.0 | 15.2 |
| | 4 | -7.93 | 15.0 | 15.2 |
| 12 mm and 19 mm | 2 | -1.22 | 12.0 | 11.7 |
| | 4 | -2.75 | 19.0 | 18.5 |
| 6 mm and 25 mm | 2 | 0.02 | 6.0 | 5.4 |
| | 4 | -2.19 | 25.0 | 24.2 |
| 4 mm and 27 mm | 2 | 0.19 | 4.0 | 3.5 |
| | 4 | -1.52 | 27.0 | 27.1 |

**Table 3:** Gelatin line-pair phantoms, possessing one layer of 10% and another of 20%, results are presented. The calculated average intensities (dBm) and lateral displacements (mm), both measured and calculated, are shown.

| Line Pair Type | Gelatin Type Concentration (%) | Average Intensity (dBm) | Measured Lateral Distance (mm) | Calculated Lateral Distance (mm) |
|---|---|---|---|---|
| 17 mm and 15 mm | 10 | -10.80 | 17.0 | 16.5 |
| | 20 | -17.58 | 15.0 | 15.0 |
| 12 mm and 20 mm | 10 | -7.12 | 12.0 | 11.0 |
| | 20 | -20.01 | 20.0 | 21.0 |
| 7 mm and 24 mm | 10 | -3.14 | 7.0 | 7.8 |
| | 20 | -6.42 | 24.0 | 22.2 |
| 6 mm and 25 mm | 10 | -11.66 | 6.0 | 5.0 |
| | 20 | -12.26 | 25.0 | 25.0 |

The line-pair TMPs for both agar and gelatin illustrated an inverse trend between concentration and average signal intensity. The signal intensity appeared to be higher for the lower concentration of each two-layered line-pair phantom. This result is believed to be due to the elasticity differences between the two regions in each line-pair phantom. 2% agar and 10% gelatin have the lower elastic modulus in each of their respective line-pair phantoms, and, therefore, they are more easily perturbed by an ultrasonic wave from the VA system. This lack of stiffness induces an increased magnitude of emission from the lower concentration portion of the line-pair phantom, resulting in a higher average intensity for the lower concentration in each line-pair phantom. In contrast, a lower average intensity is observed in the stiffer, higher concentrated portion.

Although proximate regions in each line pair phantom can be definitively distinguished based on average intensity, we also sought to quantify the lateral distance of each region using our VA-generated images. Our VA-calculated lateral distances fell within ±1mm of the measured (actual) lateral distances obtained prior to imaging with a ruler. The results are promising, as the minute differences between calculated and measured lateral distance reinforce the potential of VA for acute boundary detection.

### 3.4.3. Sensitivity and Specificity Evaluation in Multiple-Layered TMPs

After establishing the VA system's efficacy and sensitivity in two-layered line-pair phantoms, similar experiments were conducted on three-layered and four-layered phantoms. This was done to more accurately simulate the complexity and variety of human soft tissue during intra-operative surgical procedures. The phantoms were imaged using our VA system with a similar set-up as the two-layered TMPs. The average intensities and lateral distances of regions with differing concentrations were calculated using MATLAB. Figure 20 shows the acquired amplitude and phase images of three-layered and four-layered TMPs. Figures 20A and 20D display the visible images of the three-layered and four-layered phantoms, respectively. Figures 20B and 20E display the amplitude of the detected signal, and 20C and 20F display the phase image.

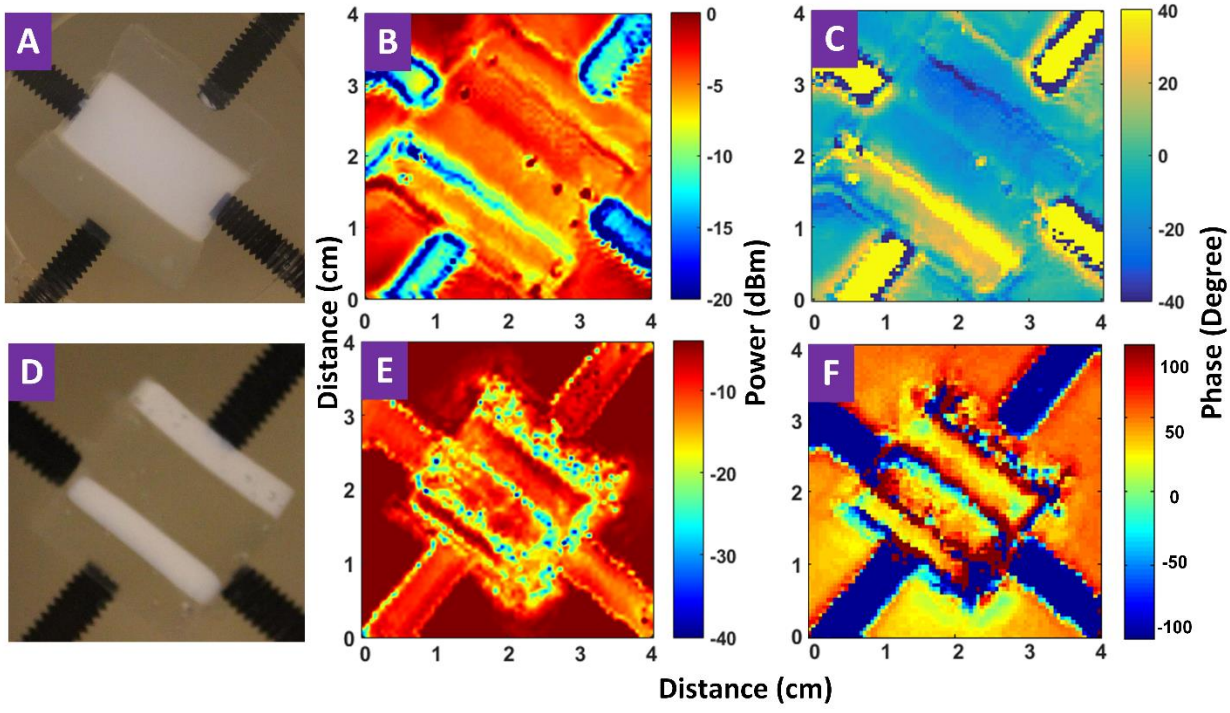


**Figure 20:** A and D illustrate the visible images of the three-layered and four-layered phantoms, B and E display the amplitude of the detected signal, and C and D present the phase image. TMP types of 15% gelatin, 2% agar, and 10% gelatin (from bottom to top) are illustrated in A. Altering 3% agar and 20% gelatin types are shown in D. The white, opaque regions are agar and the translucent regions are gelatin in both cases.

Table 4 shows the average intensity and the measured and calculated lateral distance for each region of the multiple-layered phantoms. The first region listed is at the bottom of the TMP and the last region is at the top of the phantom shown in the visible images (figures 20A and 20D). A ruler was again used to measure the lateral distance of each region and the results were compared to the VA-calculated lateral distances generated using MATLAB.

**Table 4:** Three-layered and four-layered phantoms results are presented. The calculated average intensity (dBm) and lateral displacement (mm), both measured and calculated, for gelatin and agar (of varying concentrations) are shown.

| Phantom Type | 3- Layer | | | 4-Layer | | | |
|---|---|---|---|---|---|---|---|
| Concentration | 15% Gelatin | 2% Agar | 10% Gelatin | 20% Gelatin | 3% Agar | 20% Gelatin | 3% Agar |
| Average Intensity (dBm) | -6.17 | -4.75 | -4.77 | -13.51 | -15.03 | -11.95 | -14.67 |
| Measured Lateral Distance (mm) | 10.0 | 14.0 | 10.0 | 5.0 | 4.0 | 10.0 | 4.0 |
| Calculated Lateral Distance (mm) | 9.8 | 13.6 | 10.3 | 4.2 | 3.3 | 10.7 | 3.8 |

Upon visible inspection of figure 20, VA can distinguish between agar and gelatin phantom types by detecting the boundaries between each region. The amplitude image of the three-layered phantom (figure 20B) and the phase image of the four-layered phantom (figure 20F) illustrate the best contrast between different phantom regions. However, the contrast in figures 20C and 20E is not as clear. The presence of undefined boundaries in amplitude imagery of the four-layered phantom (figure 20E) could be attributed to similarities in the emitted acoustic intensity between 3% agar and 20% gelatin. On the other hand, the inability to detect the phase changes at the boundary of the 2% agar and 10% gelatin may be accounted for by the deficient contrast in the phase image of the three-layered phantom (figure 20B). Both the amplitude and the phase images have valuable information about the target, and thus both images might need to be considered to provide improved contrast in VA imaging.

Another important factor that was examined included the relative difference in mechanical properties of the line-pair phantoms. The difference in elastic modulus between each region in both multiple-layered phantoms were examined by comparing the detected emissive acoustic signal. Regions with small and large elastic moduli differences in the case of multiple-layered phantoms were evaluated. In instances of both large (~ 50 kPa) and small (~ 10 kPa) differences in elastic modulus, a clear boundary in both amplitude and phase images were apparent. Moreover, in the case of the four-layered TMP, the average intensity difference between identical regions, of 20% gelatin and 3% agar, were approximately the same (± 1.5 dBm). Similar to trends that were previously observed, softer regions were characterized by higher acoustic signals compared to stiffer regions. In the case of three-layered TMP, the trend between 10% gelatin and 15% gelatin portions of the TMP was the same as before. In contrast, the 2% agar region of this three-layered TMP did not illustrate the lowest signal as originally expected. This discrepancy may be due to the orientation of the phantom. Since the 2% agar layer was sandwiched between two gelatin layers with lower elastic moduli, the potential interference from neighboring layers could have affected some of the generated acoustic signal. This variable must be further evaluated by varying the thickness and concentration of each layer in the TMP.

The VA-generated images of the TMPs generated relatively high signal to noise (SNR) with their respective background; however, within the TMPs, there were a few regions with speckles within the phantom that may cause discrepancies. First, in VA imagery of the three-layered TMP, a semi-superficial line in the middle of the 3% agar layer appeared. This artifact likely resulted from the fabrication process due to the use of a divider. Second, the transducer itself generates a sound field that interferes with the acoustic emission of the object. Lastly, air bubbles that form on the ground surface of the transducer during scanning and defects that occur in the TMP fabrication process

are two other potential factors that need to be considered as sources of noise in VA imagery. The manner in which the phantom is secured during scanning is another possible source of noise. Teflon screws are used to secure the TMP, and these can exert external forces to the phantom that can either attenuate or cause interference in the acquired signal. Moreover, it might be faster, more accurate, and more advantageous to use an array of elements with phase manipulations to perturb the target when utilizing VA for tissue resection purposes in an operating room.

Lateral measurement was another area that was examined in line-paired TMPs. The VA-calculated lateral distances were close to the measured (actual) distances; each length differed by no more than 1 mm in every data set as seen in table 4. This result illustrates the high precision of VA in boundary detection of proximate regions within a section of a multiple-layered TMPs. The high efficacy of experimental distance measurement coupled with high image contrast, based on mechanical properties (*i.e.* elastic modulus), makes VA a promising technique for further use in intra-operative surgical resection procedures.

This work has important implications, VA not only distinguish between two proximate material types but also can identify regions with different concentrations of the same material. These system capabilities will be essential for future clinical use of VA in an intra-operative setting. In a hypothetical situation, where surgeons are placed in similar scenarios in which healthy and abnormal tissue are positioned next to each other, and the abnormal tissue must be excised from the area, our VA system may be helpful in the determination of clear boundaries between specified regions.

## 3.5.Conclusion

The sensitivity and resolution performance limits of our VA system were evaluated. Confocal geometry for the VA transducer was utilized and its feasibility in imaging targets was evaluated.

The beam profile of the emitted radiation amplitude for a point target, a 1 mm stainless steel bead embedded in 15% gelatin TMP, on the lateral and axial planes, were derived and validated by the experimental findings. Moreover, the system sensitivity and specificity in distinguishing regions with different mechanical properties in line-pair tissue-mimicking phantoms (TMPs) were examined. Two-layered TMPs of same material type but differing concentration, and three and four-layered TMPs of a combination of agar and gelatin concentrations were imaged using our VA system. The results illustrate that the VA system is sensitive in boundary detection of both homogeneous materials with dissimilar concentrations, as well as heterogonous materials. Both amplitude and phase images demonstrated our VA imaging system ability to image multiple-layered TMPs by providing detailed information about the target; thus, for future *in vivo* experimentation, both images should be utilized for accurate tissue boundary delineation. Moreover, the fabrication, alignment, and design of the confocal transducer are other system parameters that warrant future investigation, whilst the current beam-scanning rate may need to increase for potential clinical use of VA. The theory and experimental techniques described in this work may be useful for beam forming design and system evaluation in future applications of VA.

# 4. Investigation of the Vibroacoustography System Contrast Mechanism

VA-based systems have been developed and tested primarily through imaging objects embedded in soft materials, *i.e.* imaging calcified arteries in breast tissue, and detecting and monitoring brachytherapy seeds and cryotherapy [13]. Although multiple studies have utilized VA to detect abnormal tissue regions from normal regions with enhanced boundaries [13, 63], parallel studies with other imaging modalities that utilize a comparable contrast mechanism based on absolute measurements have yet to be accomplished. The main objective of this chapter is to verify the contrast mechanism of the VA imaging system in imaging pre-clinical models with high contrast. In this chapter, images of the first *ex vivo* human head and neck squamous carcinoma (HNSCC) tissues with VA will be presented and analyzed. After establishing VA system's capability in imaging *ex vivo* specimens, parallel measurements using VA imaging and a muscle motor system for elastic property examination will be used to develop a relationship between the VA signal and target's mechanical properties. After formulation of a relationship between dynamic properties of VA and static properties of mechanical testing machines, more quantitative characterization of viscoelastic behavior will be performed on various homogeneous and heterogeneous tissue-mimicking phantoms (TMPs) and *ex vivo* animal hepatic tissues using Hertzian model. If successful, these research efforts will lay the groundwork for use of VA as a promising intervention that warrants larger scale animal studies or multi-site clinical trials.

## 4.1. *Ex vivo* Viscoelastic Characterization of HNSCC using Vibroacoustography

### 4.1.1. Overview

An imaging technique that offers a highly dynamic range detection of malignant tissue intra-operatively has not been fully established, so surgeons are often forced to excise excess healthy tissue to ensure clear margins of resection. Techniques that are currently used in the detection of

tumor regions include palpation, optical coherence tomography (OCT), elastography, dye injections, and conventional ultrasound. These techniques are used to pinpoint the affected area, but they all suffer from limitations such as minimal specificity, low contrast, and poor depth of penetration. Lack of specificity and low contrast result in the production of vague disease margins and fail to provide a reliable guidance tool for surgeons. This section demonstrates selective imaging using *ex vivo* tissue samples of head and neck squamous cell carcinoma (HNSCC) with the presence of both malignant and normal areas. Spatially resolved maps of varying acoustic properties were generated and show good contrast between the areas of interest. While the results are promising, determining the precision and sensitivity of the VA imaging system in identifying boundary regions as well as intensities of *ex vivo* tissue targets may provide additional information to non-invasively assess confined regions of diseased tissues from healthy areas and guide surgical oncologists in intra-operative settings.

### 4.1.2. Background

Head and neck squamous cell carcinomas (HNSCC) are typically aggressive tumors with a high risk of regional spread and metastases, making complete surgical resection with negative margins critical to patient outcomes [34, 55, 70]. However, a significant challenge in treatment is the complex histology of the regions surrounding the malignancy. The primary goal of surgical treatment is to completely remove malignant tissue while preserving as much surrounding healthy tissue as possible. Thus, there is a pressing need for the use of a real-time, high-resolution imaging modality to accurately differentiate between healthy and malignant tissues. Currently, the most commonly used methods for estimating tumor boundaries are dye injections, conventional ultrasound, manual palpation, and OCT elastography [13, 14, 49, 71]. Vital dyes and radio labeled colloids dye injection techniques are adept at detecting tumors. However, prior knowledge about

the tumors is necessary and the generated images are characterized by lower identification rates and false negatives at tumor detection. OCT systems can offer depth information with high resolution but the depth of penetration and field of view (FOV) are very limited and can make clinical use difficult without prior knowledge about the target [30]. Conventional ultrasound evaluates tumor regions through acoustic wave propagation and tissue scattering, which are then correlated to an approximate region depth and tissue properties, but its main disadvantage is low contrast between the different tissues. At this time, palpation is the main intra-operative technique that surgical oncologists rely on to assess the region of interest. However, this technique suffers from major limitations, including poor depth of penetration and sensitivity, and it is subject to high variability between surgeons. VA uses a dynamic acoustic force to radiate the region and receives the acoustic response of the object solely based on the viscoelastic properties of the tissue [13, 16, 34].

The above-mentioned techniques suffer from major limitations such as poor sensitivity, low specificity, and small fields of view. Major factors such as contrast, sensitivity, and spatial resolution are critical system parameters for the determination of a boundary for diseased regions with highlighted borders. Therefore, there is pressing need for a sensitive yet efficient imaging modality with the ability to rapidly and accurately provide a focal region with accurate boundaries. In this section, vibroacoustography technique will be used to accurately distinguish healthy regions from malignant regions in HNSCC. Head and neck *ex vivo* tissue samples were sectioned and arranged into samples with both healthy and malignant regions to check the system's feasibility in distinguishing various regions in the sample as well as the environment.

### 4.1.3. Materials and Methods

The VA system operated with two amplitude modulated continuous wave (CW) ultrasonic beams at slightly different frequencies (3.16 and 3.198 MHz) that were generated with a confocal transducer. This configuration produced a focused ultrasonic beam at beat frequency of $\Delta f$ =38 kHz in the focus plane. The generated radiation force caused the object to vibrate at the beat frequency. The resulting acoustic emissions were detected by a nearby acoustic hydrophone that was within close range (~ 2 cm). A band pass programmable filter followed by a lock-in amplifier was used to eliminate noise and other unwanted or interfering signals from the main signal, the same set-up as mentioned in previous sections. An image of the tissue was generated by raster scanning the focused beam across the XY plane at a 500 µm step size. The specimens were sealed in a container and were placed between the transducer and the hydrophone in a custom mount sample holder in the AMS acoustic tank. The detected acoustic emissions from the object, which are based on the object's viscoelastic properties, was used to spatially map the different regions of the sample within the FOV.

#### 4.1.3.1. Tissue Preparation

Tissue samples were procured from patients undergoing resection of primary squamous cell carcinomas (SCC) of the head and neck at the Ronald Reagan UCLA Medical Center under UCLA IRB#11-002858. Resected samples included the tumor and all surrounding epithelial and mesenchymal structures isolated by the margin selection of the surgeon and were placed in a saline solution for transfer. *Ex vivo* imaging was performed prior to tissue processing by head and neck surgical pathologists of the Department of Pathology and Laboratory Medicine at UCLA. For the specimen imaging period, since samples were fresh, they were placed in a container to mitigate tank contamination and were laid flat to decrease potential topographical effects from specimens.

All imaging was performed within two hours of resection to ensure sample integrity representative of *in vivo* conditions.

### 4.1.4. Results and Discussions

*Ex vivo* head and neck tissue were sectioned and imaged using the VA setup. The VA image and visible image of the samples are illustrated in figures 21 and 22. Photographs were taken of the specimens prior to and after being placed in the imaging system for image processing. The images of the specimens within the imaging system were then co-registered to the VA images via a non-reflective rigid affine transform using MATLAB. Vibroacoustography images were displayed using a false color map where the lowest intensity within the specimen is mapped to blue and the highest intensity within the specimen is mapped to red. In detail, figure 21 represents histology section, A, graphical representation of the sample, B, visible image prior placing into the tank, C, and VA magnitude image, D, of SCC tongue sample. As shown in this figure, the specimen can be delineated from the background with sufficient SNR; however, within the specimen, there are some ambiguities with regards to the boundaries between malignant and normal regions based on histology image. Since the specimens were placed in a container, extra layer between the specimen and the transducer as well as the hydrophone may potentially cause unwanted vibrations and/or signal attenuation. Moreover, clutter and reverberation were amongst other problems that contributed to the background noise, so better isolation in the testing tank was used for the following samples. Figure 22 represents visible as well as co-registered VA magnitude images of the HNSCC human samples. The VA image illustrated better SNR between the specimens and the background, partly due to the geometry and the type of the specimen that was imaged since better matting was used to reduce the clutter as well as the reverberation effect in the AMS acoustic tank. However, the ambiguity within the specimen remained a potential concern. Moreover, suppression

of elastic properties of tissues due to the extra container layer as well as uncertainty in tissue response were other factors that may have played a major role in the background noise as well as signal ambiguity within the specimen. Mechanical properties of targets, *i.e.* viscoelasticity, was hypothesized to be the main contrast mechanism for VA imagery, but due to complexity in various human tissue types, the fundamental contrast mechanism needs to quantified for more detailed distinction between tissue types. This study provided the basic groundwork for future quantification and characterization of the VA system for accurate boundary detection between various tissue types.

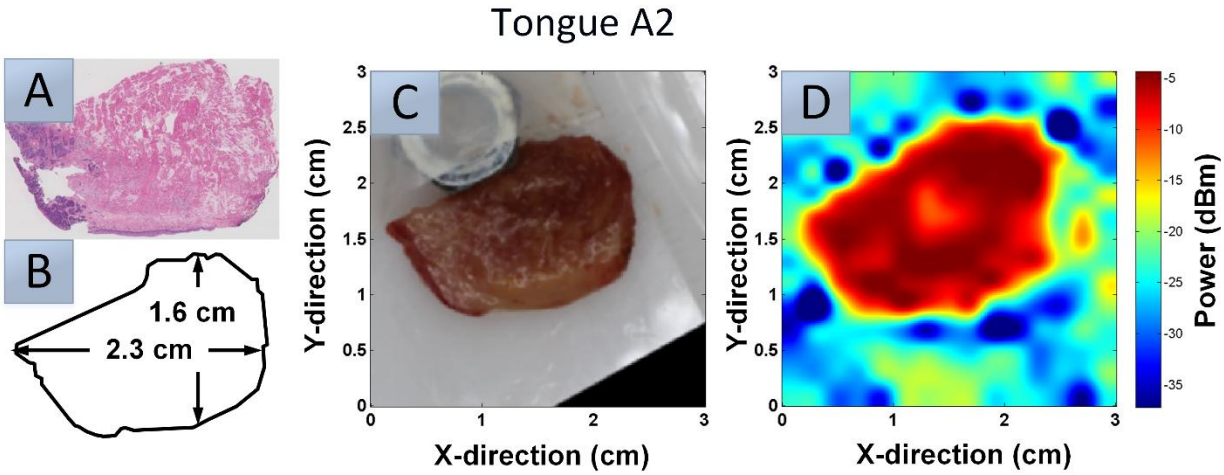


**Figure 21**: *Ex vivo* SCC image of the human tongue. A, the histological section of the specimen where darker regions represent tumor areas within the tissue (left side), B, graphical representation of the target for image registration, C, visible image of the sample with a knot as a fiducial marker for co-registration, and D, VA magnitude image of the *ex vivo* SCC of the human tongue.

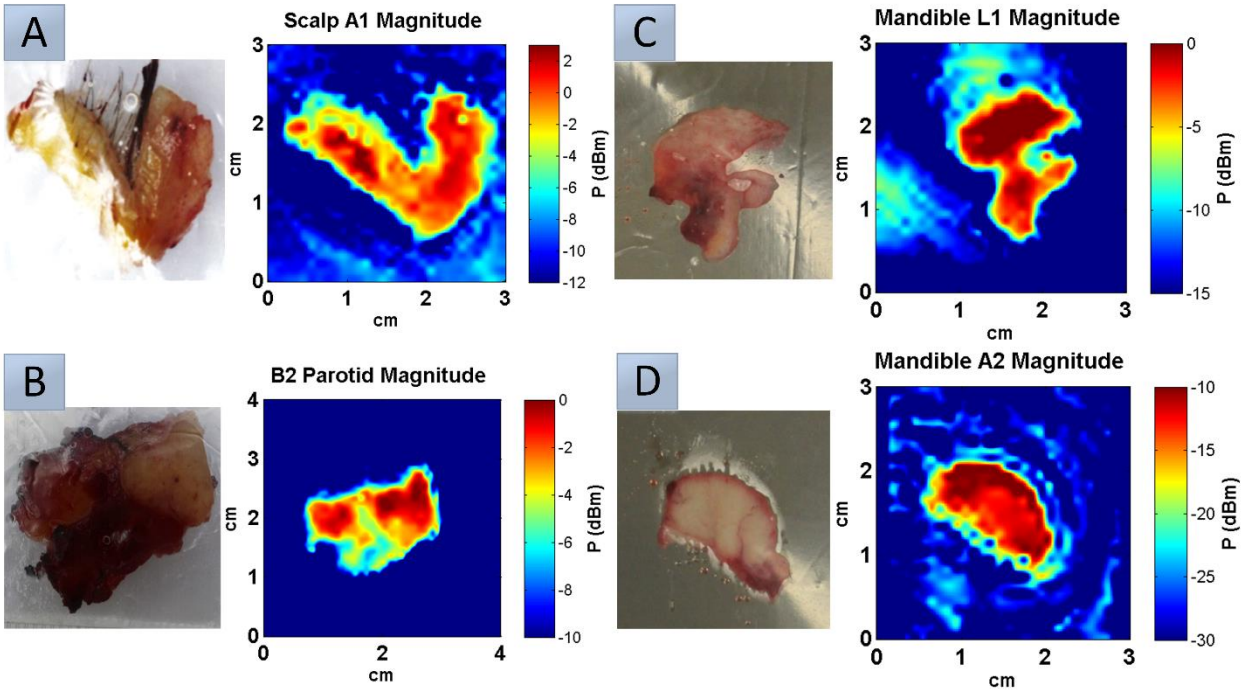


**Figure 22**: Ex vivo SCC image of the human Specimens. **A**, SCC of human scalp, **B**, SCC of human parotid, **C**, SCC of human mandible, and **D**, SCC of human mandible where left represents visible image and right represents VA magnitude image for each case. All VA images were co-registered to their visible images.

### 4.1.5. Conclusion

VA is a new imaging modality that spatially maps boundary regions within objects, solely based on their acoustic response to the radiation force, by using their viscoelastic properties. Current technologies, such as manual palpation, conventional ultrasound, and dye injections, suffer from major limitations that include low contrast, lack of specificity, and dependency on other imaging modalities. These other modalities do not provide reliable assistance for intra-operative use; however, with increasing demands for a non-invasive, novel imaging technique, VA could be a promising modality that may address the aforementioned challenges. Absolute measurements as well as accurate detection are other parameters of this imaging technique that need to be addressed for better differentiation of the boundary region between malignant and healthy tissues for intra-operative surgical needs. VA is in its preliminary stages and therefore additional development and research is required. The next sections deal with the main contrast mechanism, viscoelastic

properties, of this technique, and will validate this mechanism for absolute, quantified measurements in various tissue substrates as well *ex vivo* tissues.

## 4.2. Examination of the Elastic Properties of TMPs using VA and a Muscle Motor System

### 4.2.1. Overview

Tissue hardness, often quantified in terms of elasticity, is an important differentiating criterion for pathological identity and is extensively used by surgeons for tumor localization. Delineation of malignant regions from benign regions is typically performed by visual inspection and palpation. Although practical, this method is highly subjective and does not provide quantitative metrics. We have previously reported on vibroacoustography (VA) for tumor delineation. VA is unique in that it uses the specific, non-linear properties of tumor tissue in response to an amplitude modulated ultrasound beam to generate spatially resolved, high contrast maps of tissue. Although the lateral and axial resolutions (sub-millimeter and sub-centimeter, respectively) of VA have been extensively characterized, the relationship between static stiffness assessment (palpation) and dynamic stiffness characterization (VA) has not been explicitly established. In this section, we perform a correlative exploration of the static and dynamic properties of tissue-mimicking phantoms (TMPs), specifically elasticity, using VA and a muscle motor system. Muscle motor systems, commonly used to probe the mechanical properties of materials, provide absolute, quantitative point measurements of the elastic modulus, analogous to Young's modulus, of a target. For phantoms of varying % weight (%wt) concentrations, parallel VA and muscle motor studies conducted on 18 phantoms reveal a negative correlation ($p < -0.85$) between mean signal amplitude levels observed with VA and calculated elastic modulus values from force vs. indentation depth curves. Comparison of these elasticity measurements may provide additional

information to improve tissue modeling, system characterization, as well as offer valuable insights for *in vivo* applications, specifically surgical extirpation of tumors.

### 4.2.2. Introduction

Stiffness of soft tissues is related to their composition, and its change is often correlated to pathology and treatment; many malignant tissues, like cancers of the breast or prostate, appear as lesions of higher stiffness [3].

Despite easy access to examine the oral cavity and oropharynx, most oral lesions are detected by palpation (tactile assessment of stiffness) only after they become symptomatic [72]. Differentiating abnormal tissue from normal tissue using subjective tactile determination of tissue elasticity is suboptimal, and sensitivity and specificity may vary depending on the surgeon [73]. Consequently, there is a clinical need for more accurate and sensitive quantitative diagnostic tools that use elasticity as a contrast mechanism to differentiate normal tissue from diseased tissue. Such technologies could be applied to early detection of malignancy as well as intra-operative margin determination.

In previous chapters, we reported on VA, an imaging technology that utilizes the acoustic response of tissues to a localized, low frequency radiation force to generate spatially resolved, high contrast images [33]. VA is unique in that it relies on multiple ultrasound beams of slightly different frequencies to characterize the physical response of the target of interest. Moreover, the acquired imagery does not exhibit the speckle inherent to images of conventional B-mode ultrasound [70]. The technology utilizes the non-linear scattering properties of tissue at high frequencies to mix two ultrasonic tones and detect the difference frequency.

The lateral (-6 dB from peak) and axial (-6 dB from peak) spatial resolution of our current VA system is ~ 1 mm and ~ 1 cm, respectively. These are primarily limited by the wavelength of the

tones, and the emitting area of the focused transducer. Based on the ultrasonic scattering and absorption properties of the tissue and the monostatic configuration of our system, we estimate a 6 cm penetration depth. These operating parameters were selected to match the current limits of clinical practice [16, 22].

VA has demonstrated high sensitivity in detecting rigid objects embedded in soft materials, *i.e.* calcified arteries in breast tissue, with contrast similar to that of X-ray but without the adverse effects of ionizing radiation [38, 39, 69]. Importantly, this technology affords images of what are inferred to be spatially dependent variations in viscoelasticity. Steps toward understanding the source of contrast in VA signal have previously been undertaken primarily using inverse problem approaches [74]. The inverse problem approach for vibroacoustics involves estimating the spatial distribution of elastic moduli using the steady-state dynamic response of the objects being excited by the acoustic radiation force. While this approach offers proof-of-principle, the amplitude and distribution of the target's emission are also related to the boundary conditions, including coupling and the loading effects of the surrounding medium, as well as power absorption and scattering due to the object [74]. Therefore, based on these numerical calculations by Aguilo *et.al.*, VA images depict information that includes not only the dynamic, or mechanical characteristics of the target but also its ultrasonic properties, *i.e.* surface velocity response. So, to isolate and validate viscoelasticity as one of the primary contrast mechanism of VA, it is imperative to use a parallel modality that relies only on the mechanical properties (*i.e.* viscoelasticity of materials) of the object to generate contrast. To date, such a study remains to be performed. Given the large scope and complexity of viscoelasticity and also for practical reasons, we will only investigate the elasticity component of viscoelasticity to understand the contributions of a single component of this parameter to the image contrast observed in VA. The goal of this section is to perform a novel

study to explore the relationship between VA signal intensity and the *elasticity* of tissue mimicking phantoms (TMPs) using VA and a muscle motor system. TMPs will be used as targets to simulate relevant anatomical structures both in terms of acoustic and mechanical properties. Specifically, this study includes water-based gels to satisfy the acoustic properties of human tissues, including the speed of sound (about 1540 $m/s^2$), attenuation (about 0.5 $dB^{-1}$ $cm^{-1}$ $MHz^{-1}$) and backscatter coefficient (between $10^{-5}$ and $10^{-2}$, between 2 and 7 MHz) [67].

These TMPs consist of agar, gelatin, and polyvinyl alcohol (PVA) because they emulate the primary constituents of tissue - specifically water and protein and, therefore, are hypothesized to provide mechanical and acoustic properties equivalent to that of tissue. For each type of phantom, three distinct concentrations were synthesized, where the middle concentrations (15% gelatin, 3% agar, and 17% PVA) simulates the stiffness of human tissues *i.e.* prostate, oral cavity, liver, and breast [65, 67, 75-77]. Literature value for young's modulus of these types of phantoms fall under the same range as the respective tissue they mimic [5, 67], making our phantoms again ideal candidates for modulus and other types of mechanical properties quantifications (*i.e.* shear modulus, viscosity, and Poisson ratio). Moreover, these materials are well-characterized in the scientific community and their use may offer clinically relevant information for intra-operative applications.

A muscle motor system, analogous to the Instron Mechanical Testing Machine, is used as a quantitative method to probe the absolute elasticity by evaluating the dynamic elastic properties of targets, tissue-mimicking phantoms in this case, to which parallel VA signal measurements are compared [5]. Moreover, this correlative study investigates the responses of various homogeneous isotropic tissue-mimicking phantoms under dynamic force (from VA) and static force (from the

muscle motor system) and evaluates the hypothesis that differences in the elastic properties of targets can be used as a key contrast mechanism in VA to differentiate target regions.

### 4.2.3. Materials and Methods

#### 4.2.3.1. Vibroacoustography System

VA typically uses low MHz frequency illumination beams to probe and map the mechanical response of a target to a dynamic acoustic radiation force in the 10-100 kHz range [16]. In typical vibroacoustrographic systems, two continuous wave (CW) ultrasound beams at two slightly offset frequencies are focused on the interrogated area in the target of interest. A stress field at the beat frequency ($\Delta f$ ) is generated at the focus region of the transducer, and the target absorbs the illumination beams and re-emits ultrasonic energy at the beat frequency. Consider the two ultrasonic beams ($x_1$, $x_2$) in equations 4.1 and 4.2 where $A_{1,2}$ is the beam amplitude, $f_{1,2}$ is the frequency, and $\varphi_{1,2}$ is an arbitrary phase offset.

$$x_1 = A_1 \cos(2\pi f_1 t + \varphi_1) \tag{4.1}$$

$$x_2 = A_2 \cos(2\pi f_2 t + \varphi_2) \tag{4.2}$$

In the most general case, the target responds to the modulus of the two beams and produces harmonics of the difference frequency which has been reported with spectral analysis of VA signals [16, 22]. In the case of this work, we only consider the fundamental of the difference frequency corresponding to the ultrasonic beam modulus. This output is written as:

$$y_1 = (\alpha(x_1 + x_2)^2 * h)(t) \tag{4.3}$$

where the constant $\alpha$ corresponds to the nonlinearity of the tissue, and $h$ represents an ideal band pass filter convolved with the product of α and sum of the two waves squared. This function selects the difference frequency component from the product of $x_1$ and $x_2$ and rejects DC.

$$y_1 = \alpha A_1 A_2 \cos(2\pi \Delta f t + \Delta\varphi) \tag{4.4}$$

The measure output is given in equation 4.4 where $\Delta f$ corresponds to the fundamental difference frequency of $f_1$ and $f_2$ and $\Delta\varphi$ is differential phase offset. The difference frequency acoustic emission is related to the mechanical and physical properties of the target. This emissive wave is measured at a close distance, ~ 2 cm, away from the object using a sensitive acoustic hydrophone. Due to bandwidth constraints engineered into the hydrophone and receiver electronics, the residual high frequency ultrasonic beams are not detected and the output is only dependent on the power of the envelope frequency. By mechanically scanning the focused beam spot over our target, an image is created of what is hypothesized to be spatially varying mechanical properties- the viscoelasticity- of the target [16, 33]. Thus, materials with different elastic properties have different responses and may potentially provide intrinsically unique contrast within the field of view.

Two ultrasonic tones of 3.16 MHz for the inner transducer and 3.198 MHz for the outer transducer were used in a continuous wave (CW) fashion to drive the curved confocal transducer with a radius of curvature (ROC) of 6 cm. This was used as the source to produce an acoustic radiation force to vibrate the target of the interest. The target was placed at the focal region of the ultrasound beams from the transducer in a water tank and the acoustic generated emission from the target, typically on the order of ~0 dBm, is detected using a sensitive hydrophone (TC4014-5, Teledyne Reson Inc., Goleta, CA) with a sensitivity of -180 dB re 1V/µPa. The hydrophone was placed at ~2 cm away in a water tank to couple the generated acoustic waves from the transducer to the object and the emitted acoustic waves from the object to the hydrophone. The output of the hydrophone was directly connected to a programmable bandpass filter (SRS 650, Stanford Research Systems Inc., Sunnyvale, CA), low noise amplifier (LNA), and a Lock-in Amplifier (SRS 844, Stanford

Research Systems Inc., Sunnyvale, CA) for quadrature detection of the emitted difference frequency. The focused beams from the curved transducers were mechanically scanned over the surface of the target at $\Delta f$ = 38 kHz, and at each point the peak amplitude of the emission is measured and used to construct an image. Each pixel value was normalized to the peak amplitude during image processing and analysis. The $\Delta f$ for this experiment was set at 38 kHz primarily due to our system's electronic components, the transducer, and also based on our previous experimental findings in tissue mimicking phantoms and *ex-vivo* human cancer specimens [33].

#### 4.2.3.2. Muscle Motor System

A dual mode muscle motor system (Aurora Scientific Inc., 305C-LR, ON, Canada) is used to measure the static physical properties of targets and to further evaluate the tissue-mimicking phantoms' mechanical properties. This technique measures and controls both the applied displacement and force. The system is operated isometrically, in which the displacement is held constant while resultant forces are measured. Figure 23 is a block diagram of the system, its main components, and the experimental setup that is used for this study.

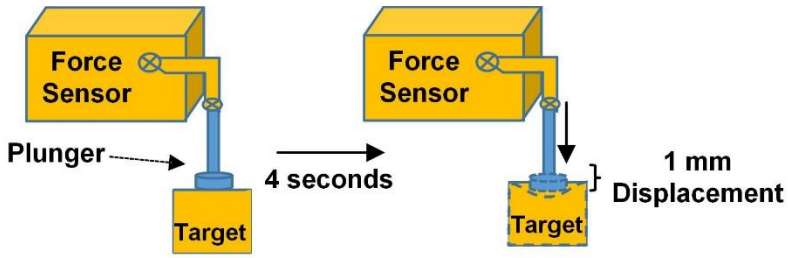


**Figure 23**: Block diagram of the plunger connected to the force sensor of the muscle motor system. It displaces by 1mm in a period of 4 seconds on the target as depicted in the figure on the right.

An acrylic plunger (diameter = 4mm) is used to apply uniform stress as an indenter to the TMPs at a given displacement (1mm) in a time frame of 4 seconds; this duration allows adequate time

for the target to respond to the applied pressure from the plunger. The sensor is used to record the response force from the target to the plunger.

#### 4.2.3.3. Phantom Synthesis

Two sets of three phantom types with three varying percent-by-weight (%wt) concentrations were fabricated to generate a total of 18 phantoms. VA images of these phantoms were obtained and compared to elasticity measurements acquired with a muscle motor system on the same phantoms. Agar, PVA, and gelatin materials at %wt concentrations detailed in the following paragraphs were chosen due to their similar acoustic properties to human tissues (*i.e.* prostate, oral cavity, liver, and breast) [5, 65, 74, 76].

Agarose blocks (Agar, Sigma-Aldrich, St. Louis, MO) of varying deionized water/agarose concentrations were fabricated in a 2 x 2 x 2 $cm^3$ plastic mold. Three rectangular blocks of agarose containing 2, 3, and 4 %wt concentrations of agarose were mixed and heated above their gel point (90 $^oC$) to maximize cross linking between the polymers. The final mixture was placed in a centrifuge at a rotation speed of 2 rcf (relative centrifugal force) for a period of ~25 seconds to remove air bubbles from the solution. Increasing the amount of powder, in each case, in the mixtures was predicted to result in a corresponding increase in the elastic modulus of the phantom. Gelatin blocks (Porcine Gelatin, Sigma-Aldrich, St. Louis, MO) of 10, 15, and 20 %wt concentrations were used as a second type of tissue mimicking phantom. The same protocol used to form the agarose blocks was used to form the gelatin blocks using the previously described protocol.

Finally, a third type of tissue mimicking phantom, polyvinyl alcohol (PVA), was fabricated. Three rectangular blocks of PVA (99% hydrolyzed, Sigma-Alrich, St. Louis, MO) containing 14, 17, and 20 %wt concentrations of PVA were chosen. Unlike the agarose and gelatin phantoms, the final

PVA mixtures were left at room temperature to cool down for ~ two hours and were then placed in a freezer at -20 $^{0}$C for a period of 24 hours. Prior to imaging, the PVA phantoms are allowed to thaw only once, equivalent to one freezing-thawing cycle.

Based on the previous studies, 3% agar, 15% gelatin, and 17% PVA provide a good approximation of healthy human tissue in terms of acoustic velocity, acoustic impedance, and acoustic attenuation, while elastic modulus is an important parameter for elasticity characterization of human tissue [66, 75-79]. For instance, the acoustic velocity in the chosen PVA phantoms were shown to vary from 1520–1540 m/s, which is within the typical range for human tissue. Also, PVA phantoms ranging 14% to 20% are characterized by acoustic impedances that are similar to human breast and skin tissue. For agar TMPs, the 2% to 4% range matches the acoustic properties of human prostate tissues. Lastly, the selected gelatin phantom concentrations mimic the acoustic attenuation of human tissues, specifically breast, liver, head and neck, and prostate [65, 66, 75, 76].

The phantoms are placed in a sample holder and are mechanically scanned while the transducers, placed on top of the sample, and the hydrophone, placed 2 cm below the sample, are fixed in position. Each target is submerged in the water tank and fixed in place using 4 Teflon screws to avoid movement, to increase acoustic coupling, to minimize background noise, and further to enhance the signal-to-noise ratio (SNR) during VA high contrast image acquisition [16, 33]. The VA system scanned a 3x3cm$^2$ field of view (FOV) across the surface of all phantoms in 500 μm increments at the focus region in the z-axis.

### 4.2.4. Results and Discussion

The investigation of the contrast mechanism of the VA system was tested by imaging 3 different types of homogeneous isotropic TMPs and comparing these results to those observed with a parallel muscle motor system. Since, each phantom measured 2 x 2 x 2 $cm^3$, the phantom thickness in both VA intensity measurements and muscle motor system elasticity measurements were negligible because they had the same height. A raw magnitude VA image for all concentrations of each phantom type was generated. The middle phantom in each material category by the aforementioned references was shown to mimic the acoustic properties of healthy human tissue, whereas the low and high concentrations for each TMP reflect those of abnormal human tissues. These images are displayed in a standard false color map in Figure 24. Each image has its own gray scaled dynamic range and was normalized with respect to itself not to other %wt concentrations in that type. In each image, a region of interest (ROI) outlined by a white box is used for comparison of mean VA signal intensity amongst phantoms. Based on visual inspection of all types of synthesized TMPs, those with higher %wt concentration appear to demonstrate decreased VA intensity, denoted by darker colors in the color bar.

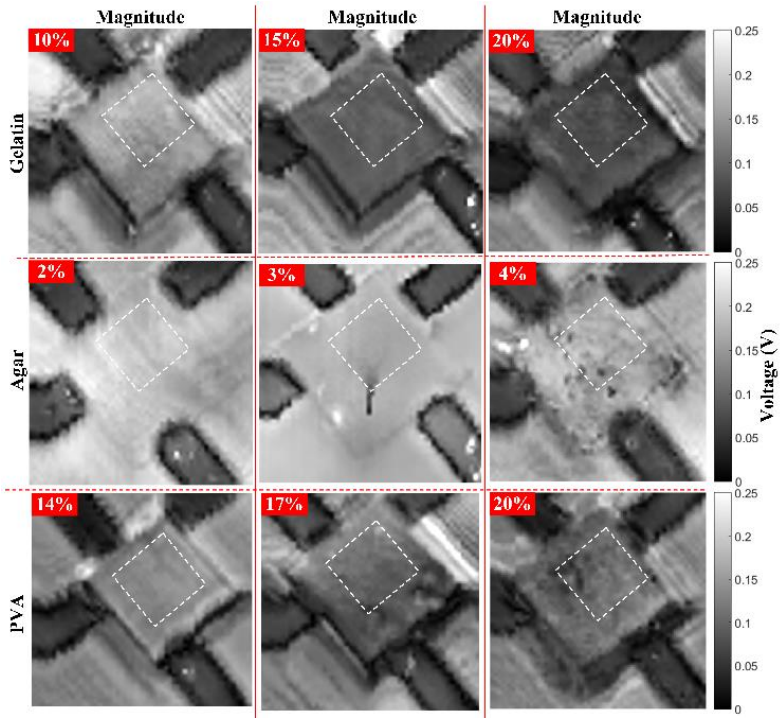


**Figure 24**: Vibroacoustographic images of gelatin, agar and PVA with varying %wt concentrations, displayed from left to right. Images are reconstructed on the basis of the magnitude of the acoustic emission at 38 kHz. The white box in the images indicates the region that was selected from each image to evaluate the mean signal intensity.

These observed changes in image contrast are confirmed by quantitative assessment in figure 25, which shows the normalized mean amplitude emission associated with ROIs at the difference frequency, 38 kHz, with respect to the %wt concentration for each type of phantom with an inverse relationship between %wt concentrations and mean acoustic emitted amplitude. It has previously been suggested that image contrast observed in VA is due to the shape, size, and mechanical properties of the target [16, 22]. However, since geometry and size are held constant across all phantom types, we are confident that their contributions to contrast were minimal and the primary difference in elastic properties of the target dominate VA image contrast. Previous publications illustrate that as the material becomes stiffer, the generated acoustic emission becomes stronger; however, the exact opposite is observed here [13, 22]. At about the same density, stiffer materials (*i.e.* higher concentrated TMPs) exhibit faster speed of sound than softer materials (*i.e.* lower

concentrated TMPs); however, medium property (*i.e.* elasticity) is another factor that can affect the propagation and thus that may be the reason for our generated VA trend. Stiffer materials are associated with larger %wt concentrations, and therefore are characterized by more cross-links between the constituents of the material. Another hypothesis is that stiffer materials become more immobile, and hence are characterized by lower acoustic emissions. Moreover, the surrounding medium may affect the acoustic emission, specifically by attenuating the detected response.

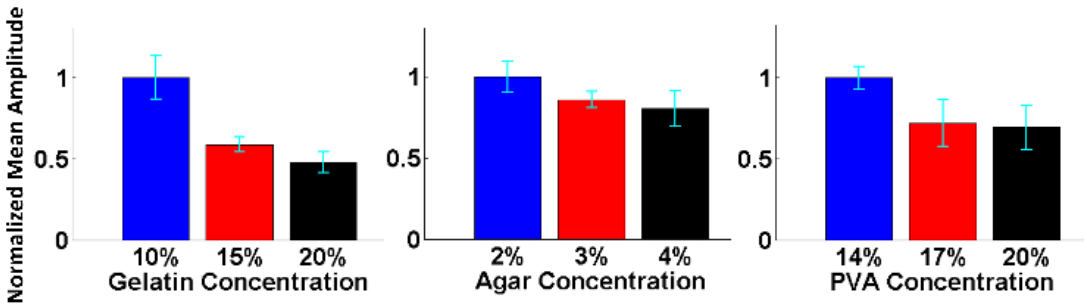


**Figure 25**: Normalized mean VA amplitude values associated with gelatin, agar, and PVA phantoms at different concentrations, respectively. The phantom with the smallest concentration in each type has the largest normalized mean amplitude.

As was illustrated in figure 25, it was confirmed that as the concentration of the targets increases, their mean intensity VA signal level decreases. After acquiring images using the VA system, the same phantoms' elastic properties were evaluated using the muscle motor system. The strain applied in this setup is sufficiently small enough (less than 10%) such that the phantoms can be assumed to be elastic. Qi *et.al.* also reported a similar observation using their Optical Coherence Elastography (OCE) system [80, 81]. They illustrated that axial displacement, movement of the target after radiative force perturbation, increases for soft materials as opposed to hard materials, and this was demonstrated to be a function of pre-amplified voltage to the transducer, *i.e.* generated radiative force. The differences in elastic properties of the phantoms are also demonstrated in the force vs. indentation depth curves in Figure 26.

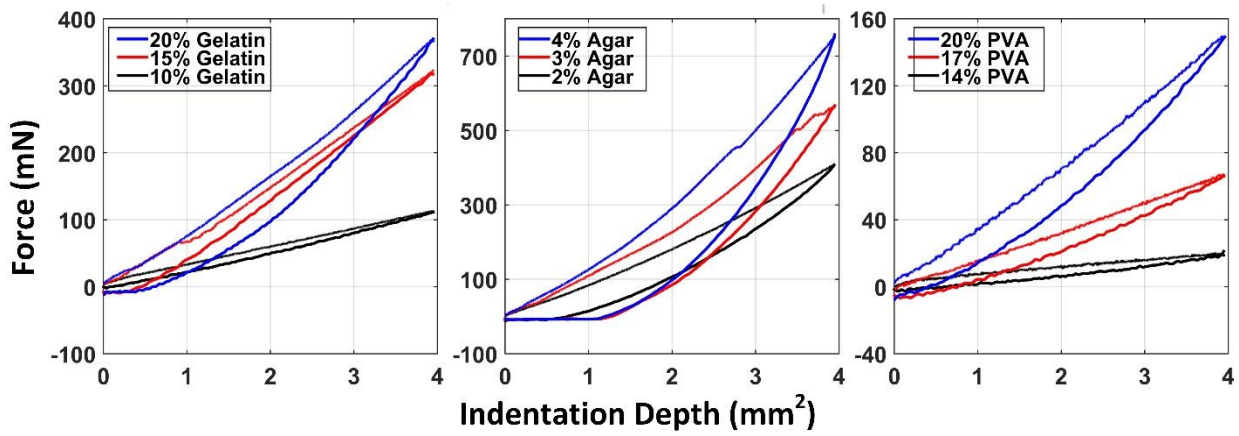


**Figure 26**: Force vs. indentation depth curves of gelatin, agar, and PVA phantoms, respectively, were generated using the muscle motor system where the force is in mN and the indentation depth is the product of the diameter of the plunger (mm), *i.e.* indenter, and the displacement (mm).

Phantoms with larger %wt concentrations have larger force vs. indentation depth curves, as expected. For the three types of phantoms tested, elastic modulus, analogous to young's modulus, values were calculated from the loading cycle curve for each concentration [5, 67]. In our case, contact between a rigid cylinder with flat-ended plunger and an elastic half-space (*i.e.* the surface area) of each phantom were taken into considerations for the following calculations [82]. Since the plunger is acting as an indenter to the phantom, the following equation was used for the modulus calculations:

$$F = 2rdE \tag{4.5}$$

where $F$ represents the recorded force in mN, $2r$ is the diameter of the indenter (*i.e.* plunger) in mm, $d$ is the recorded displacement in mm, and $E$ is the modified elastic modulus, analogous to young's modulus of solids, in kPa, while the product of the plunger's diameter and the reordered displacement is the indentation depth in $mm^2$. Based on the elastic assumptions discussed earlier, a first-order approximation was used to quantify the relative elastic modulus of the phantoms (table 5).

**Table 5:** Calculated elastic modulus, analougous to young's modulus of solids, values from the slope of force vs. indentation depth plots for each phantom.

| Agar | | PVA | | Gelatin | |
|---|---|---|---|---|---|
| | Modulus (kPa) | | Modulus (kPa) | | Modulus (kPa) |
| **2%** | 491.10 | **14%** | 21.22 | **10%** | 128.90 |
| **3%** | 694.00 | **17%** | 82.28 | **15%** | 391.50 |
| **4%** | 897.00 | **20%** | 178.90 | **20%** | 441.20 |

Based on these findings, changes in mean VA acoustic emissions are realted to changes in VA elasticity measurements as a function of %wt concentration for all phantom types. There appears to be a very strong inverse trend between concentration and VA response with correlation coefficients of -0.998, -0.965, and -0.857 for gelatin, agar, and PVA, respectively. These correlation coefficients were calculated by correlation test. As mentioned earlier, this correlation, though not originally predicted, makes physical and acoustic sense: physically, as the material becomes stiffer, its elastic modulus increases and as material becomes softer, its constituents become more mobile; thus, softer material appear to have an increase in the acoustic emission. The VA mean amplitude values and their companion modulus measurements demonstrate a monotonic trend that appears to describe the unique elastic properties and acoustic response of each phantom type. To the best of our knowledge, this study illustrates a direct comparison of elasticity as a potential contrast mechanism of VA. With regards to the clinical relevance of these results, the observed modified elastic modulus values appear to be within the same order of magnitude as those reported of various types of human tissues: ~ 10 kPa for parenchyma, ~ 1-100 kPa for muscle, ~ 50 kPa for connective tissue, ~ 65 kPa for prostate, and ~ 10 kPa for liver [5, 67]. Therefore, the TMPs explored in this study may be ideal candidates for the characterization of moduli as well as other relevant mechanical properties (*i.e.* shear modulus, viscosity, and Poisson's ratio). More

importantly, VA can be used to spatially map regions with different elastic properties and may help clinicians to distinguish tissue types with different elastic properties.

Without denying the significance of these results, additional experimental trials with protocols of increasing complexity, specifically changes in applied amplitude and the elapsed time associated with the test, are required to more accurately examine the elastic properties of the target as a key source of contrast in VA.

### 4.2.5. Conclusions

Tissue-mimicking phantoms were used to investigate the contrast mechanism of a VA system by comparing mean signal amplitudes associated with VA generated images to elasticity measurements acquired with a muscle motor system. As demonstrated, the phantoms with smaller % concentration, 2 %wt agar, 10 %wt gelatin, and 14 %wt PVA, demonstrated larger signal amplitude levels, but smaller elastic moduli values. Both the VA and muscle motor systems were able to distinguish phantoms with differing % concentrations from one another and an inverse-correlation was observed. These experiments represent a first step in utilizing this methodology for quantification of the elastic properties of materials. The next step entails an investigation of multi-layered phantoms with different elastic properties (*i.e.* young's modulus) that more accurately represent human tissues in clinical settings (illustrated in chapter 3). Since most biological materials are viscoelastic, studying TMPs characterized by both elasticity and viscosity will also be necessary to understand biological materials and how they function in healthy and diseased states (will be discussed later in this chapter). Such an investigation of the viscoelastic behavior of a target takes into consideration how the environment will react to the forces imposed by VA, and therefore ensures the effective and successful performance of VA-based technologies.

Tissue and materials characterization is another area that can benefit from the spatial mapping capabilities of VA; however, the current system needs to be upgraded to move vibroacoustography closer to clinical use. For instance, changing the detection scheme by combining the hydrophone with the transducer, similar to a conventional ultrasound, is an approach that may make the system more robust for *in vivo* applications (will be discussed in chapter 5).

## 4.3. VA System Characterization using Parallel $\Delta fs$ and Elasticity Measurements

Despite high contrast observed in VA imaging of tumor tissue, viscoelasticity has yet to be verified as the primary source of image contrast [42]. An investigation of the contrast mechanism of VA is necessary to interpret VA data for potential, accurate tumor margin assessment. This section focuses on establishing a relationship between VA signal intensity and elasticity of the targets by using multiple $\Delta f$ frequencies and elastic modulus measurements. Due to complexity of tissue viscoelasticity, only the elastic component of viscoelasticity was investigated to better understand the contributions of a single mechanical component in VA imagery. To model biological tissue, tissue mimicking phantoms (TMPs) were synthesized and used as targets in the VA study. In parallel to VA imaging of the targets, spherical-tip indentation, was performed on the phantoms to calculate the elastic modulus and their results were compared to explore the contributions of elasticity to VA image contrast.

### 4.3.1. Materials and Methods

VA system, consisting of a confocal piezoelectric transducer and an acoustic hydrophone, along with the TMPs were placed in AMS acoustic tank to achieve minimal signal loss as the acoustic wave propagates. System electrical parameters and components are identical to the previous sections. The targets were placed at the focus plane of the curved confocal transducer, ~5.9 cm from the end of the transducer. As a result of the interference between the two MHz waves, low

kHz difference frequency wave ($\Delta f$) was generated to perturb the TMP. Human tissue constituents such as muscle, adipose tissue, connective tissue, collagen, elastin, and extra cellular matrix have different responses when undergoing radiation force in the low kHz regime. Their responses can be characterized not only from their geometry and mechanical properties, but also from their acoustic response to an optimal $\Delta f$ frequency. Thus, $\Delta f$ manipulation can be used as a distinguishing criteria in delineating boundaries in intra-operative procedures [83]. Each phantom in this study was imaged at a $\Delta f$ of 28 kHz, 38 kHz, and 48 kHz in order to isolate an optimal, possibly resonance, difference frequency (with sufficient SNR) for each TMP. These three $\Delta f$s were chosen due to our system's constraints and based on the literature. The average power (dBm) of the emitted acoustic vibration response for each TMP at each $\Delta f$ was calculated and compared to the elastic modulus for each TMP.

Elastic modulus of each TMP was calculated with a spherical-tip indentation method [84]. This was done by gradually inserting a 2mm diameter stainless steel sphere for 600 μm into the surface of each TMP without causing rupture. The responding force that the TMP exerted on the sphere was recorded with respect to time as the sphere penetrated the surface of the TMP. Using the following equation, elastic modulus was calculated:

$$\mathrm{E} = \frac{3\mathrm{F}(1-\vartheta^2)}{4\sqrt{\mathrm{R}}\mathrm{h}^{3/2}} \tag{4.6}$$

where R is the radius of the sphere indenter, h is the displacement of the indenter, and ϑ is the TMP's Poisson's Ratio. 0.5, a typical value for incompressible soft tissue, was assumed for our calculations for Poisson's Ratio [5]. Three types of TMPs were synthesized for VA imaging: 1) gelatin 15 %wt mimicking the acoustic attenuation and elastic modulus of human breast, liver, head, and neck tissues; 2) agarose 3 %wt, mimicking the aforementioned properties of human prostrate tissue; and 3) polyvinyl alcohol (PVA) 17 %wt mimicking the aforementioned properties

of human skin tissue [67, 75, 76]. The TMPs were synthesized by mixing a powdered extract with deionized water over a steaming water bath at ~90° C to allow for cross-linking of the polymers. Each solution was then removed, poured into a 2 x 2 x 2 $cm^3$ mold, and allowed to cool and solidify two hours prior to imaging. The PVA phantom required one freezing and thawing cycle to be completed prior to imaging to properly retain mechanical properties observed in human breast and skin tissue [75]. Since the geometry of each phantom was kept the same, the geometric effect can be ignored for signal intensity measurements and elastic modulus calculations.

### 4.3.2. Results and Discussion

The mean power of each TMP as well as calculated elastic modulus is presented in Table 6. The targets with higher elastic moduli exhibited lower intensity signal overall when they were subjected to radiative force as illustrated in the previous section. Change in the radiation force frequency, however, may allow a target to vibrate at its resonance frequency. As shown in the following table, 17 %wt PVA TMP presented highest VA signal intensity at 38 kHz whereas 3 %wt agar and 15 %wt gelatin demonstrated this phenomenon at 48 kHz. As seen in the PVA TMP, if the difference frequency is raised above the resonance value, the signal intensity of the TMP decreases. In this case, the target was no longer in its resonance range of vibration, resulting in a less powerful acoustic emission [85, 86].

**Table 6**: The mean power (dBm) of the emitted acoustic vibration and calculated elastic modulus for 15 %wt gelatin, 3 %wt agar, and 17 %wt PVA after subjection to three difference frequencies. Elastic modulus values (kPa) for 15 %wt gelatin, 3 %wt agar, and 17 %wt PVA were calculated with a spherical-tip indentation method with indentation depth of 600 μm. The values for Elastic Modulus obtained here are similar, and fall within the same magnitude of our previous values in the last section.

| TMP Type | Power 28 kHz (dBm) | Power 38 kHz (dBm) | Power 48 kHz (dBm) | Elastic Modulus (kPa) |
|---|---|---|---|---|
| **Gelatin 15%** | -8.05 | -5.88 | -5.34 | 43.52 |
| **Agar 3%** | -5.24 | -2.99 | -1.32 | 199.05 |
| **PVA 17%** | -19.37 | -16.65 | -16.84 | 9.55 |

17 %wt PVA was the softest (*i.e.* 9.55 kPa, lowest elastic modulus) amongst the other two phantoms. The low elasticity of PVA causes a greater excitation at a lower difference frequency from the VA system. From the decrease in power from 38 kHz to 48 kHz, it is evident that the PVA phantom likely experienced its optimal difference frequency prior to 48 kHz. An increase in $\Delta f$ thus caused the PVA phantom to leave its resonance range of vibration. In fact, the decrease in power at 48 kHz further validates this presumption that targets exhibit different resonant ranges based on their mechanical properties.

Furthermore, the elastic modulus of gelatin and agarose are 5 and 20 fold greater than that of PVA, respectively. Thus, theoretically, both gelatin and agarose should require a higher difference frequency during VA imaging to reach optimal power output (*i.e.* reach their respective resonance states). As shown in table 6, the gelatin and agarose TMPs both display an increase in signal intensity as the difference frequency increases and show peak average power at the highest difference frequency (*i.e.* 48 kHz). However, the power output of the gelatin TMP increases at a lower rate from 38 kHz to 48 kHz compared to agar. Given the elastic Modulus for gelatin, 43.52 kPa, it is evident that it would require a lower difference frequency than agarose, which possesses a much greater elastic modulus of 199.05 kPa. This difference in elasticity is seen in the power trend between the two phantoms; gelatin reacts less to the 10 kHz increase from 38 kHz to 48 kHz, as it only experiences a 9.2% increase in power output. In comparison, the agar phantom experiences a 55.9% increase in power output. Due to agar's high elastic modulus, it should theoretically require a higher difference frequency to perturb it for an optimal power output [42]. While gelatin appears to level towards maximum power near 48 kHz and PVA reaches an optimal difference frequency prior to 48 kHz, possibly at around 38 kHz, the 3% agar TMP shows the most constant increase in power output throughout all three difference frequencies.

### 4.3.3. Conclusions

Comparison of vibroacoustography (VA) signal intensities and elasticity measurements acquired in TMPs suggest that the VA system is dependent on the mechanical properties of the intended target. To acquire maximum power output, it is imperative to image the target at, or near, its resonance frequency. Moreover, the optimal difference frequency ($\Delta f$ ) of each material, when using VA, is dependent on the mechanical properties of the target, specifically the elastic modulus amongst others (*i.e.* viscosity and shear modulus). TMPs with a higher elasticity exhibit higher signal intensity at higher difference frequencies, while TMPs with lower elasticity reach peaks in intensity at lower difference frequencies. Using both elastic modulus and difference frequency to distinguish tissue, VA may gain traction as an intra-operative imaging modality for surgical resection procedures. In addition, by assigning optimal $\Delta f$ to different types of biological tissue, a more informative scan with a high signal to noise ratio (SNR) can be acquired with VA imaging. Although a precise optimal difference frequency for each TMP was not isolated, our goal for future research is to create a database of difference frequencies that create the highest mean power for common biological tissue as well as TMPs with various viscoelastic values. Since there are no previously reported optimal difference frequencies for biological tissue available in the literature, it is feasible to estimate a $\Delta f$ to provide maximum signal intensity. Specifically, optimal difference frequency can be estimated based on the elastic modulus of the biological tissue, given the observed relationship that suggests an increase in elastic modulus may result in an increased optimal difference frequency. Even though the sample size for this study was low, the generated results can be used as a potential guideline for formulation of a mathematical model involving VA system characterization, which will be examined in chapter 6. This study provides a means for potential quantitative identification of malignant biological tissue amongst normal tissues with

accurate detection schemes based on the relative difference in their mechanical properties. Further experimentation, which will be covered in the next sections will focus on establishing a quantitative correlation between tissue mechanical properties (*i.e.* viscosity and elasticity) and the optimal VA difference frequency. Lastly, a model that will relate these two variables will be developed toward the end of this dissertation to accurately produce the optimal difference frequency for any given value of mechanical properties for unclassified biological targets.

## 4.4. Quantitative Characterization of Viscoelastic Behavior in pre-clinical Models

### 4.4.1. Overview

Viscoelasticity of soft tissues is often related to pathology, and therefore, has become an important diagnostic target in the clinical assessment of suspected disease and injury in the field of medicine. Palpation -the estimation of tissue elasticity obtained via touch- is the current gold standard used by surgeons intra-operatively in distinguishing tumorous tissue from healthy tissue. This detection method, however, is highly subjective, qualitative, and often fails for abnormalities that lie deep in the tissue, or those that are too small to be resolved by hand. Local estimation and regional imaging (*i.e.* vibroacoustography) of mechanical properties of tissue offer new means of discriminating between tissues with high contrast. However, because literature on the mechanical properties (*i.e.* both elasticity and viscosity) of abnormal tissue is very limited, a firm understanding of the contrast behind these elastography methods still remains elusive. These observations provide the motivation for this section to further investigate viscoelasticity theory and to present a detailed description of viscoelastic experimental results obtained in both tissue mimicking phantoms (TMPs) and *ex vivo* tissue. The spherical-tip micro-indentation technique along with the Hertzian model were employed to acquire absolute, quantitative point measurements of the elastic modulus (E), viscosity ($\eta$), and time constant ($\tau$) in isotropic

homogeneous TMPs and *ex vivo* hepatic tissue in rat and porcine models. Liver elasticity and viscosity for porcine liver, porcine gallbladder, and rat liver were 2.55±0.09 kPa, 4.7±0.7 kPa, and 2.76±0.09 kPa for elastic moduli and 0.135±0.006 MPa·Sec, 0.18±0.03 MPa·Sec, and 0.147±0.007 MPa·Sec for viscosity, respectively with relative high $R^2$ value (> 0.9), and relative small error of the mean. The porcine liver and bile duct tissue results illustrate statistically significant difference between two proximate organs that may be used as a differentiating factor for imaging modalities that use viscoelastic properties of tissue. These results on viscoelastic properties of targets may facilitate more accurate tissue modeling as well as add information not currently available to the field of systems characterization.

### 4.4.2. Introduction

Evaluation of viscoelastic properties of materials plays a crucial role in material science, nondestructive testing (NDT), and medical diagnosis. Specifically, a target's elastic modulus, or "stiffness," and viscosity can be determined from the resultant displacement from an applied force. The change in stiffness of soft tissues is often associated with pathological state, and therefore is a diagnostic target, for example, for oral cancers to reduce the morbidity associated with this disease and to further assist surgeons with tumor excision procedures intra-operatively. Oral cavity and pharynx cancer are among the 10 most common cancers worldwide and affect approximately 42,440 people in the United States annually[87]. Based on recent studies, tumorous tissues are typically characterized by an elastic modulus that differs from surrounding healthy tissue by several orders of magnitude. Such tissue contrast can be leveraged to delineate tissue margins between diseased and normal regions [67]. Currently, standard clinical practice relies heavily on palpation in determining relative tissue stiffness. This method is based on a qualitative assessment of the region; moreover, in many cases, the size and/or the location of the lesion make palpation

an insufficient method for medical diagnosis. A non-invasive, remote, high-resolution technique that uses viscoelastic properties of tissue to generate contrast may be more appropriate to detect small tissue abnormalities that are otherwise occult.

Over the last decade, there has been growing interest in studying viscoelastic properties of soft tissues and their connection to pathological variation in biological tissue by vibrocoustography (VA) and elastography in combination with various imaging modalities (*i.e.* Magnetic Resonance (MR) and Optical Coherence Tomography (OCT)). While they are all new research imaging approaches that are used to investigate and reconstruct mechanical properties of tissue, VA has gained more attention due to its real-time imaging capability, resolution, and minimal cost [70]. In comparison to palpation, the transverse spatial resolution of VA is in the sub-millimeter range and the depth of penetration (*i.e.* slice thickness) is in the sub-centimeter range, depending on the chosen frequencies, making the technique more suitable for high resolution detection and imaging of tissue abnormalities [22]. In response to an applied oscillating force, the object vibrates and produces an acoustic emissions field at the difference frequency, which is then detected at a distance away from the focus using a highly sensitive hydrophone. Our group has previously reported on a novel VA imaging system that has been used to generate high contrast maps of tissues in response to a localized, low-frequency acoustic radiation force in both tissue mimicking phantoms (TMPs) and *ex vivo* human squamous cell carcinoma (HSCC) tissue [33, 41, 42]. Although multiple studies have investigated VA to detect abnormal regions from normal regions with enhanced tissue boundaries [22, 39, 41, 69], a direct correlation has yet to be established between acoustical signal and mechanical measurements, including both elastic moduli and viscosity, in tissue to confirm viscoelasticity as the main contrast mechanism of VA. In addition, to relate the amplitude and phase variation of the emitted vibration to mechanical properties of the

target, a mechanical model that examines the viscoelastic behavior of the target is necessary. Moreover, the existing modalities with their theoretical models fail to include either all the properties (elastic moduli, viscosity, and the time constant) or often oversimplify the model with too many theoretical assumptions for mechanical evaluation of the targets; therefore, there is a need for a model along with the modalities that utilize it to take advantage of all the properties for complete characterization of the tissue. This paper will primarily focus specifically on the mechanical modeling for modalities that use viscoelastic properties of tissues, particularly vibroacoustography, as the contrast mechanism. Based on our previous VA signal intensity and elastic moduli correlation study of TMPs, we determined that other factors such as viscosity and time constant should be considered for complete modeling of viscoelastic properties of tissues [42]. Herein, we use rheological models, particularly Hertzian model, in conjunction with a micro-indentation technique using a rigid spherical-tip to acquire absolute measurements of mechanical properties on TMPs and *ex vivo* porcine and rat hepatic tissues. Elastic modulus, viscosity, and time constant results in *ex vivo* animal tissue, a close physiological model to human tissue with well-defined literature, were compared to those in homogeneous TMPs under static force (*i.e.* spherical-tip micro-indentation technique) to explore the similarities and differences between the two. Mechanical measurements were acquired in three phantom types (agarose, gelatin, and PVA) at distinct concentrations to mimic the acoustic properties of human tissue. Moreover, porcine and rat liver along with porcine gallbladder tissues were chosen to closely correlate the findings to human tissues. Nevertheless, evaluation of these results may provide insight in better understanding the contrast mechanism of the VA system and quantitatively relating acoustical signals and mechanical measurements by mathematical modeling.

### 4.4.3. Modeling and Methods

Biological tissues are modeled as viscoelastic materials due to a manifestation of hysteresis on relaxation of the stress [88, 89]. The word viscoelastic is a combination of viscous fluidity and elastic solidity, and thus these materials under stress and strain exhibit both viscous and elastic behavior. Moreover, in modeling materials such as biological tissues, linear elastic Hookean spring, which describes elasticity behavior, and linear viscous Newtonian Dash-pot, representing viscosity behavior, are used to examine and understand the performance of these materials under spring force and displacement. The following figure shows the linear elastic spring and linear viscous Dash-pot [88, 89].

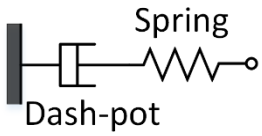


**Figure 27**: Viscous Dash-pot and linear spring lumped element model connected in series.

The linear elastic spring relates stress, exerted force per unit area, to strain, changes in length with respect to its original length, in a linear fashion by elastic modulus (*E*) for solids. During this mechanical process, the material will undergo an instantaneous deformation upon loading and an instantaneous de-straining upon unloading. The following equation illustrates the simplified relationship in 1D case:

$$\sigma = E\,\varepsilon \tag{4.7}$$

where σ and ε represent stress (force per unit area) and strain (displacement per unit length) in 1D, respectively.

The linear viscous Dash-pot contains a piston-cylinder filled with a viscous fluid and, by definition, relates stress, $\sigma$, and strain, $\dot{\varepsilon}$, by the viscosity of the material (η) in a linear fashion for fluids. The following equation represents the linear elastic spring and linear viscous Dash-pot.

$$\sigma = \eta \dot{\varepsilon} \tag{4.8}$$

Multiple models, such as Maxwell-Dash-pot model, Kelvin Voigt model, and Hertzian model, have been used to characterize the mechanical properties of biological tissues. The Hertzian model was chosen to analyze the acquired data because spherical-tip micro-indenter was used in this study. Moreover, it has previously been used in characterizing bovine ocular tissues and provided similar data to other techniques [84].

#### 4.4.3.1. Hertzian Model

The Hertzian viscoelastic contact model relates the exerted force, *F*, from a rigid sphere with a radius of R to the elastic modulus and the Poisson ratio ($\vartheta$) of an incompressible material at a given displacement, $h$. This model evaluates the relaxation behavior of the specimens by incorporating a Ramp Correction Factor (RCF) and elastic moduli. RCF illustrates the sole difference between ramp and step loading for each exponential decay and only depends on the ratio of material time constant to experimental rise time.

$$F = \frac{4E\sqrt{R}h^{3/2}}{3(1-\vartheta^2)} \tag{4.9}$$

Poisson ratio, the ratio of the transverse contracting strain to the elongation strain, of biological materials, that are incompressible, is assumed to be between 0.45 to 0.5, for TMPs, *ex vivo* porcine hepatic and bile duct tissues, and it is chosen to be 0.5 [5, 12]. The relaxation response for a step-load rigid spherical-tip indenter to the materials, as a function of time, can be illustrated by the following equation:

$$F(t) = \frac{8\sqrt{R}}{3} h_0^{3/2} G(t) \tag{4.10}$$

where time-dependent shear relaxation modulus, $G = E/3$. For real instances the actual rise time ($t_R$) is not an instantaneous step loading process. Therefore, the viscoelastic integral operator for relaxation, where $u$ is a strain function in terms of $\tau$, is used.

$$F(t) = \int_0^t G(t-\tau) \left[\frac{du(\tau)}{d\tau}\right] d\tau \tag{4.11}$$

As shown by Mattice et al. [90], Boltzmann integral method is utilized to solve the following integral by combining equations 4.10 and 4.11

$$F(t) = \frac{8\sqrt{R}}{3} \int_0^t G(t-\tau) \left[\frac{d}{du} h^{3/2}(u)\right] du \tag{4.12}$$

For ramp-loading rate $k$, displacement for ramp-hold relaxation can be written as:

$$h(t) = kt \qquad 0 \le t \le t_R \tag{4.13}$$

$$h(t) = kt_R = h_{max} \quad t \ge t_R \tag{4.14}$$

Since the load, $F(t)$, is exponentially decaying during the process, the solution is expressed as the step-loading relaxation solution adjusted by an RCF due to non-instantaneous ramp loading where only the first two terms are considered [91, 92]:

$$F(t) = A_0 + A_1 \exp(-t/\tau_1) \tag{4.15}$$

$$G(t) = B_0 + B_1 \exp(-t/\tau_1) \tag{4.16}$$

where $\tau_1$ represents the time constant for the first exponential decay, and $A_0\ and\ A_1$ and $B_0\ and\ B_1$ represent the fitting constants and the relaxation coefficients, respectively. Only the first term of both the fitting constants and relaxation coefficients are computed to compare with the Wiechert theoretical model, which represents the material relaxation in terms of applied force

[93]. Once all the fitting parameters, $A_0$ *and* $A_1$, have been determined, they are converted to material parameters, $B_0$ *and* $B_1$, using the following equations where $t_R$ is the time that it takes for the force to reach its maximum value:

$$B_0 = \frac{A_0}{h_{max}^{3/2}\left(8\sqrt{R}/3\right)} \tag{4.17}$$

$$B_1 = \frac{A_1}{\left((RCF_1)h_{max}^{3/2}\ 8\sqrt{R}/3\right)} \tag{4.18}$$

$$RCF_1 = {\tau_1}/{t_R}\,[\exp(t_R \cdot \tau_1) - 1] \tag{4.19}$$

Instantaneous $E(0)$ moduli can be computed from the fitted relaxation coefficients using the following equation:

$$E_0 = 1.5\,G(0) = 1.5(B_0 + B_1) \tag{4.20}$$

Moreover, the viscosity, $\eta$, for each type of material can be calculated as follows:

$$\eta = E \cdot \tau \tag{4.21}$$

#### 4.4.3.2. Target Preparations

The target preparation is divided into two phases: 1) TMP investigation and 2) *ex vivo* animal hepatic tissues and bile duct examination. For the first part of this study, certain assumptions such as physical geometry and size of the phantoms were chosen to satisfy homogeneity and isotropy assumptions for modulus calculations. For the second, ~flat sections as well as ideal sizes were chosen to avoid slippage and reduce any generated noise from the measurements.

Three phantom types (agar, polyVinyl Alcohol (PVA), and gelatin) with three varying percent-by-weight (%wt) concentrations were fabricated. These materials were chosen to simulate relevant anatomical structures (*i.e.* prostate, oral cavity, liver, and breast) in terms of their acoustic and

mechanical properties [10-12, 18-21]. These three types of TMPs are comprised of the primary constituents of tissue -specifically water and protein- and therefore, were hypothesized to provide mechanical (*i.e.* viscoelastic and acoustic) properties equivalent to that of tissue. Literature values for young's modulus of these types of phantoms fall under the same range as human tissue substituents [5, 93], making our phantoms again ideal candidates for modulus and other types of mechanical properties (e.g. shear modulus, viscosity, and Poisson ratio). Another advantage is that these three sets of phantoms occupy three different elasticity ranges: PVA, lower end of elastic moduli, 1-40 kPa, gelatin, slightly higher, 10-100 kPa, and agar, the highest range, 100-200 kPa, were chosen to help characterize systems in a broader range of optimal detection for abnormalities. For each type of phantom, three distinct concentrations were synthesized to provide a good approximation of healthy human tissue. 15% gelatin, 3% agar, and 17% PVA in that case were chosen due to their similarity in terms of acoustic velocity, acoustic impedance, and acoustic attenuation [66, 67, 75-79]. Furthermore, the similarity in acoustic properties between these phantoms to human tissues will make this study a crucial stepping stone for imaging modalities like VA, and will help establish that the mechanical properties of the tissues are the primary agents for creating defined boundary regions. In addition, their elastic modulus and viscosity are important parameters for viscoelastic characterization of human tissue, e.g. prostate, oral cavity, liver, and breast and can provide valuable insight for future characterizations.

Agarose blocks (Agar, Sigma-Aldrich, St. Louis, MO) of varying deionized water/agarose concentrations were fabricated in a ~ 2 x 2 x 2 $cm^3$ plastic mold. Three rectangular blocks of agarose containing 2, 2.5, and 3 %wt concentrations of agarose were mixed and heated above their gel point (~90 $^oC$) to maximize cross-linking between the polymers. Increasing the amount of

powder in the mixtures is predicted to result in a corresponding increase in the elastic modulus of the phantom.

Gelatin blocks (Porcine Gelatin, Sigma-Aldrich, St. Louis, MO) of 10, 15, and 20 %wt concentrations were used as a second type of TMP. Same steps were followed as the agar, but the final mixture was also placed in a centrifuge at a rotation speed of 2 rcf (relative centrifugal force) for a period of ~25 seconds to remove air bubbles from the solution.

Finally, a third type of TMP, PVA, was fabricated using the same procedure as stated above. Three rectangular blocks of PVA (99% hydrolyzed, Sigma-Alrich, St. Louis, MO) containing 14, 17, and 20 %wt concentrations of PVA were made, but unlike agarose and gelatin phantoms, the final PVA mixtures were left at room temperature to cool down for ~ two hours and then placed in a freezer at -20 $^{0}$C for a period of 24 hours for one freezing-thawing cycle.

Fresh *ex vivo* liver and bile ducts were harvested from porcine and male Dewey rats shortly after the animal was euthanized under an approved ARC protocol. The samples were stored in saline solution for transferring to the experimental room while maintaining it at ideal physiological conditions to avoid tissue dryness and degradation. Prior to measurements, the tissues were taken out the saline solution and were cut into smaller ideal pieces ~ 15 x 15 x 10 mm$^3$. After splitting the samples into model sizes, they were placed in a petri dish on a balance for viscoelastic measurements.

#### 4.4.3.3. Experimental Setup

A custom system is used to deliver a given stress/strain at a defined displacement, for a controlled period of time, to probe the absolute instantaneous elastic modulus, viscosity, and time constant of the targets. A 100-nm precision linear stepper motor and controller (LNR50 Series, Thorlabs, Newton, NJ) were synchronized with a 100-µg precision analytical balance (ML Model, Mettler-

Toledo, Columbus, OH) to perform the viscoelastic measurements on the targets. The stepper motor was connected to an acrylic rod that displaces a 2mm in diameter stainless steel sphere. The sphere was used for indentation depth of 300 µm and 400 µm for *ex vivo* porcine liver samples, 200 µm and 300 µm for *ex vivo* rat liver, and 100 µm for porcine gallbladder. Slightly larger sphere, 4mm in diameter, was used for 600 µm and 800 µm indentation of TMPs. For all micro-indentation measurements, much less than the radius of the sphere, was used to avoid any types of errors. These indentation distances were chosen due to the thickness of the targets and to further stay in the linear regime, ~3% strain rate, of the samples. The indenter displaces downward against the targets, which were placed on an analytical balance pan for accurate force measurements. The linear motor speed was set as 2 mm/sec. Theoretically in the relaxation test, input loading is assumed to be instantaneous; however, since our linear motor was not able to displace instantaneous step indentation, ramp loading input was applied and ramp correction factor (RCF) was used in calculations to account for that change [91, 92]. The phantoms were made at least 90 min prior to measurements to avoid any confounding errors such as dryness in the collected data. Prior to each measurement, the balance was zeroed to avoid surface tension errors on the acquired data. Shortly after, the sphere, with a given displacement and a fixed rate optimized for each target, was indented into the target and then allowed to relax for approximately 300 sec., while the applied force was recorded from the target Figure 28 illustrates the experimental setup that was used to acquire measurements. Two indentation depths were utilized to accurately compute viscoelastic behavior of each target type. Moreover, the displacement depth for all cases, except gallbladder tissues, was less than the radius of the indenter to avoid any subsequent error for the recordings.

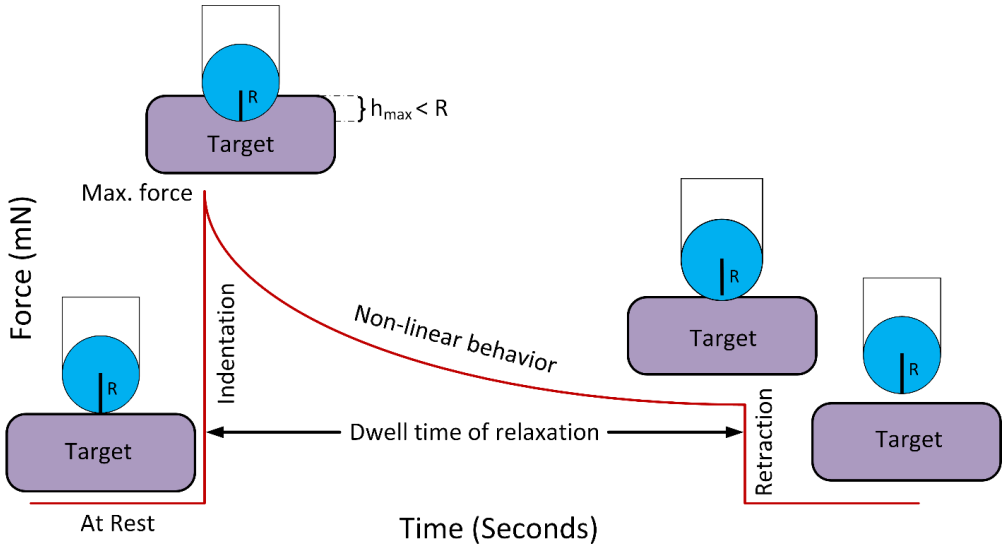


**Figure 28**: Spherical-tip micro-indentation experimental set-up. As illustrated in the figure, the sphere induces indentation into the target while keeping the indentation depth smaller than its radius (indentation period). After it reaches the maximum depth, it lets the target relax back to its original place (dwell time of relaxation period) in a period of 300 seconds. After completion of the process, the sphere is moved away from the target (retraction period).

### 4.4.4. Results

The viscoelastic behavior of tissue mimicking phantoms (TMPs) and *ex vivo* porcine and rat hepatic tissues were examined by micro-indentation technique using a stainless steel sphere. The isotropic homogeneous TMPs were fabricated in our laboratory with defined geometrical structures due to the molds they were synthesized in. Moreover, due to the controlled phantom setting, the phantom thickness, ~18 mm, did not vary among each phantom. A total of 10 measurements, 5 for each depth, were conducted on each phantom type to calculate the average, along with the standard error of the mean for each type of test. For *ex vivo* hepatic tissues, since they were excised fresh, their thickness, typically ~11mm for porcine liver, ~ 6mm for rat liver, and ~1mm for porcine gallbladder, and their geometrical arrangements were not identical to one another. However, these samples had relatively flat surfaces and were excised to have ~ similar dimensions to avoid collection/ slippage error. Moreover, a 2mm in diameter stainless steel sphere

was used for the indentation of *ex vivo* tissues to avoid non-linear behavior. A total of 13 porcine liver samples and two gallbladder samples from two different porcine subjects were examined. *Ex vivo* indentation measurements consisted of a total 34 liver indentation measurements, 17 for each depth, for porcine liver tissue, and 7 measurements for gallbladder tissue, were used to perform indentation tests on porcine hepatic tissues. For rat liver tissues, a total of 14 samples from three different subjects for a total of 38 liver indentation measurements, 19 for each depth, were used to perform these viscoelastic characterization tests.

Figure 29 illustrates the relaxation plots for tissue mimicking phantoms and table 7 shows instantaneous elastic modulus, viscosity, and time constants along with their standard error of the mean for three TMP types for two different indentation depths, 600 and 800 μm. Elastic moduli and viscosity values were calculated by fitting the collected data to a first order exponential decay and from that, the constants were calculated using the Hertzian model in MATLAB. For PVA phantoms of 14%, 17%, and 20% concentrations (% by wt), the average calculated elastic moduli were 5.66±0.16 kPa, 9.44±0.20 kPa, 33.72±1.02 kPa, and the viscosity were 0.99±0.04 MPa·Sec, 1.63±0.08 MPa·Sec, and 4.26±0.27 MPa·Sec, respectively. For gelatin phantoms of 10%, 15%, and 20% concentrations (% by wt), the average calculated elastic moduli were 16.35±0.90 kPa, 45.21±2.24 kPa, 65.96±3.09 kPa, and the viscosity were 2.77±0.13 MPa·Sec, 6.37±0.31 MPa·Sec., and 8.80±0.45 MPa·Sec, respectively. For agar phantoms of 2%, 2.5%, and 3% concentrations (% by wt), the average calculated elastic moduli were 104.64±3.91 kPa, 135.48±4.65 kPa, 195.17±4.28 kPa, and the viscosity were 5.80±0.21 MPa·Sec, 9.58±0.61 MPa·Sec, and 14.24±0.84 MPa·Sec, respectively. As calculated in table 7 and shown in figure 29, one can clearly distinguish the three phantom types since each depict a specific region based on their elastic moduli calculations. The standard error of the mean for elastic moduli and viscosity

measurements of each phantom type portray a very small deviation from the mean in both indentation depths for all of the phantoms. Moreover, as shown by the calculations in table 7 and figure 29, as the concentration of gelatin and PVA TMPs increases, the calculated time constant decreased. However, for agar TMPs, the exact opposite trend occurred, as calculated in table 7 and seen figure 29. The agar phantoms depicted an increase in their time constant as the concentrations increased

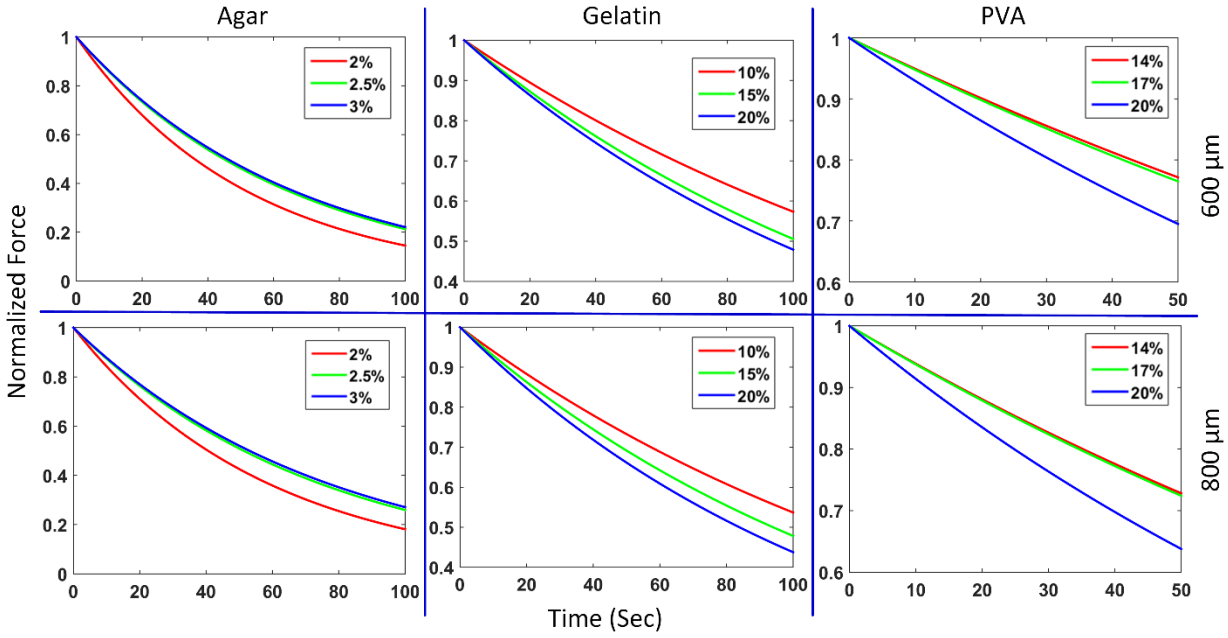


**Figure 29:** Elastic relaxation behavior plots of agar, gelatin, and PVA tissue mimicking phantoms. The plots illustrate normalized force exponential decay as a function of time. Gelatin and PVA behave the same as their concentrations increases, but for agar opposite is shown. In another word, there was a positive direct relationship between the concentration of agar TMPs and their calculated time constants.

**Table 7:** TMPs elastic modulus, viscosity, and time constant data along with standard error of the mean for each phantom type, PVA, gelatin, and agar, with given concentrations.

| Phantom Type | Elastic Modulus (kPa) | | Average (kPa) | Standard Error | Viscosity (MPa.Sec) | | Average (MPa.Sec) | Standard Error | Time Constant (Sec.) |
|---|---|---|---|---|---|---|---|---|---|
| | 600 µm | 800 µm | | | 600 µm | 800 µm | | | |
| 14% PVA | 5.722 | 5.598 | 5.660 | 0.158 | 1.105 | 0.883 | 0.994 | 0.040 | 175.657 |
| 17% PVA | 9.552 | 9.319 | 9.435 | 0.200 | 1.785 | 1.467 | 1.626 | 0.075 | 172.330 |
| 20% PVA | 33.563 | 33.866 | 33.715 | 1.015 | 4.693 | 3.824 | 4.259 | 0.273 | 126.317 |
| 10% Gelatin | 15.823 | 16.873 | 16.348 | 0.897 | 2.830 | 2.710 | 2.770 | 0.128 | 169.424 |
| 15% Gelatin | 43.518 | 46.903 | 45.210 | 2.243 | 6.390 | 6.358 | 6.374 | 0.309 | 140.988 |
| 20% Gelatin | 62.010 | 69.907 | 65.959 | 3.087 | 8.649 | 8.957 | 8.803 | 0.445 | 133.458 |
| 2% Agar | 106.497 | 102.778 | 104.638 | 3.911 | 5.595 | 6.000 | 5.797 | 0.210 | 55.405 |
| 2.5% Agar | 137.034 | 133.918 | 135.476 | 4.647 | 9.122 | 10.045 | 9.583 | 0.607 | 70.737 |
| 3% Agar | 199.049 | 191.284 | 195.166 | 4.281 | 13.575 | 14.913 | 14.244 | 0.840 | 72.984 |

Figure 30 illustrates the relaxation plots for *ex vivo* hepatic tissues and table 8 illustrates instantaneous elastic modulus, viscosity, and time constants along with their standard error of the mean for *ex vivo* specimens composed of porcine liver and gallbladder and rat liver for two different indentation depths for livers, 300 and 400 µm for porcine liver, 200 and 300 µm for rat liver, and one indentation depth, 100 µm for porcine gallbladder. For porcine tissues, the average calculated elastic moduli for liver was 2.55 kPa, and 4.73 kPa for gallbladder and the average viscosity values were 0.135 MPa·Sec. for liver, and 0.176 MPa·Sec for gallbladder. With regards to rat liver, the average calculated elastic moduli was 2.76 kPa and viscosity was 0.147 MPa·Sec with small variations in all cases. The calculated time constants for both rat liver and porcine liver were very close averages illustrating the viscoelastic similarity of the two tissue types. Moreover, as shown by the calculations in table 8 and plots in figure 30, both liver tissues demonstrate similar behaviors in terms of time constant for both indentations depths. The porcine gallbladder tissues also demonstrate a smaller decay rate, time constant, in comparison to the liver tissues.

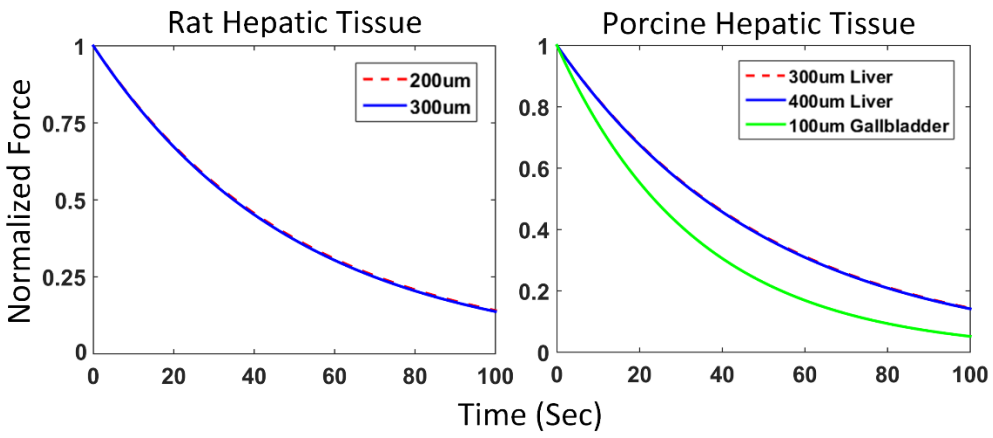


**Figure 30**: Elastic relaxation behavior plots of *ex vivo* animal hepatic tissues. As apparent, the liver tissues for both rat and porcine decay exponentially in a similar fashion for both indentation depths. For the porcine tissues, there is a clear distinction between gallbladder and liver tissues in terms of relaxation behavior.

**Table 8:** Ex vivo porcine liver and gallbladder and rat liver elastic modulus, viscosity, and time constant data along with standard error of the mean for each tissue.

| Tissue Type | Depth | Elastic Modulus (kPa) | Average | Standard Error | Viscosity (MPa.Sec) | Average | Standard Error | Time Constant (Sec.) |
|---|---|---|---|---|---|---|---|---|
| Porcine Liver | 300 µm | 2.575 | 2.553 | 0.085 | 0.138 | 0.135 | 0.006 | 52.879 |
| | 400 µm | 2.531 | | | 0.132 | | | |
| Rat Liver | 200 µm | 2.890 | 2.758 | 0.094 | 0.154 | 0.147 | 0.007 | 53.299 |
| | 300 µm | 2.626 | | | 0.14 | | | |
| Porcine Gallbladder | 100 µm | 4.730 | 4.730 | 0.735 | 0.176 | 0.176 | 0.033 | 37.209 |

### 4.4.5. Discussion

This section evaluates the characterization of the viscoelastic properties of TMPs and *ex vivo* hepatic tissues by examining the fundamental factors of their mechanical properties (*i.e.* elastic modulus and viscosity). This study utilizes Hertzian mathematical model, which involves spherical-tip micro-indentation to analyze the relaxation curves by fitting the generated curves into a first order exponential fit with relatively high $R^2$ value, above 0.9, for all cases. Other models, such as Maxwell-Dash-pot and Kelvin-Voigt, were also considered for the evaluation of the collected data; however, since spherical-tip micro-indentation was used, the Hertzian mathematical model provided the most suitable approach for the analysis.

Our results illustrate that for mechanical modeling of biological tissue with viscoelastic behaviors, both elasticity and viscosity should be considered. The TMP elasticity measurements show three unique regions in elastic properties, with ranges: 1-40 kPa (low), 10-100 kPa (medium), and 100-200 kPa (high). Along with their corresponding viscosity values, the TMPs were examined to cover a wide range of viscoelastic soft tissues which was shown by Wells and Liang [67]. Moreover, *ex vivo* hepatic tissues of porcine and rats were also analyzed in the same fashion to explore their similarities and differences with TMPs. This work originated from our previous work that correlated elastic properties of TMPs with radiation force intensity measurements from vibroacoustography system [42]. The spherical-tip micro-indentation elastic moduli results from this study were similar to those of muscle-lever indentation generated results and provided quantitative support for our calculations for viscosity and *ex vivo* hepatic tissues of porcine and rats in this study [42]. The results obtained from that work encouraged the examination of other mechanical properties of targets (*i.e.* viscosity and time constant) for development of a mathematical model to elucidate the observed behavior from the phantoms under the acoustic radiation force of ultrasound imaging modalities, *i.e.* vibrocoustography and elastography techniques. Due to our unique experimentation setup and measurement calculations, direct comparisons are not forthright for each aspect of the study; however, similar approaches have been made. Hamhaber *et al.* completed a quantitative comparison of shear wave MR elastography technique with mechanical compression tests on agar-agar gel phantoms by comparing strain generated wave amplitudes from shear-wave MR elastography to computed shear modulus by performing dynamic mechanical compression tests [94]. They computed the elastic modulus of their 2% agar-agar elastic modulus computation, by making an assumption of Poisson ratio of incompressible materials. Their results were within the same range of ours. Pavan *et al.* examined

non-linear elastic behavior of gelatin and agar phantoms by using Bose Endura TEC 3200 ELF system [95]. They used large oscillatory deformations (~25% strain rate) on 2 month old phantoms samples, whereas the phantoms used in this study were freshly made and experiments were conducted on the same day on ~3% strain rate. They reported higher values than those reported in this study, but the age along with the high deformation rates could explain the values. However, the overall trend in the aforementioned study where higher concentrations elucidate higher moduli values, is very similar to the ones generated from this study.

In addition to the parameters analyzed above, viscosity and time constant were analyzed. To the best of our knowledge, there are no straightforward comparisons with the literature, but there are related works on shear viscosity of soft tissues and solids characterizations. Catheline *et al.* performed measurement of viscoelastic properties of bovine muscle using transient elastography by comparing Maxwell to Voigt model [96] and Kobayashi *et al.* performed a similar study on viscoelastic solids with high viscosity by uniform shear stress deformation method in a temperature controlled setting [97]. However, the values reported by Catheline *et al.* are orders of magnitude smaller and Kobayashi *et al.* values are orders of magnitude higher than the ones reported on TMPs in this paper. One reason can be due to the deformation methods along with the assumptions they utilized to acquire these measurements. Kobayashi *et al.* used pure shear and mainly tensile (extensional) deformation mode and Catheline *et al.* used transient elastography with frequency ranges from 50 to 350 Hz in 25 Hz step which can be the reason of the difference of orders of magnitude in viscosity measurements. The calculated time constants for the TMPs for both gelatin and PVA followed the same trend as the one presented in this study, steady decrease as the concentration increased, but it was the opposite for the agar phantoms. This may be due to the structural properties as well as the cross-linking of the agar substituents within the phantom.

The second half of this study was devoted to the investigation of *ex vivo* porcine and rat hepatic tissues. Porcine liver and gallbladder tissues along with rat livers were tested using the same technique that was used for TMPs. For this case, the tissues were excised fresh, right after the animal was euthanized, and were kept in a saline solution during transport for freshness. Many scientists use pre-conditioning technique with cyclic deformations for their *ex vivo* sample preparations, but that technique was not used in this study, since the generated results were already in steady-state mode and the elastic moduli, viscosity, and time constant calculations were consistent with very low standard error of the mean [98]. Moreover, the duration of examination for each sample was relatively short, ~15 minutes per sample, demonstrating the perseverance of the physiological conditions and mechanical feasibility throughout the span of the measurement. Like the case of the TMPs, there is no direct comparison for our generated *ex vivo* porcine and rat hepatic tissue viscoelasticity data with the literature, but methodologies have been developed. Kerdok *et al.* characterized the effects of perfusion on the viscoelastic characteristics of liver by using indentation devices to measure the organs' creep response to applied loads [99]. Their calculated time constants, $\tau$, were very similar to the ones calculated in this study for both porcine and rat liver, demonstrating similarity in physiological structure as well the accuracy of our measurements. However, elastic moduli and viscosity were not directly calculated in Kerdok *et al.*'s study, but the calculated time constant can alone be a precursor to the viscoelastic measurements since in theory, the time constant is the product of viscosity and elastic modulus, *i.e.* Young's modulus.

Reported literature normal *in vivo* human parenchyma liver has shear modulus and viscosity of $\mu_1$ = 2.06 ± 0.26 kPa and $\mu_2$ = 1.72± 0.15 Pa·s by Magnetic resonance elastography (MRE), normal *in vivo* porcine liver obtained from 9 different Shearwave Dispersion Ultrasound Vibrometry

(SDUV) measurements are $\mu_1$ = 2.2 ± 0.63 kPa and $\mu_2$ = 1.96 ± 0.34 Pa.s, and normal *in vivo* parenchyma rat liver has $\mu_1$ = 1.76 ± 0.37 kPa and $\mu_2$ = 0.51 ± 0.04 Pa·s by MRE [100, 101]. By assuming liver to be an incompressible material, the Poisson ratio can be estimated to be 0.495 [67], and the elastic moduli can be calculated using the relationship between shear modulus and elastic modulus in the following equation:

$$\mu = \frac{E}{2 * (1 + \vartheta)} \tag{4.22}$$

Using this methodology, the approximate elastic moduli will be ~6.16 kPa for *in vivo* human parenchyma liver, ~6.58 kPa for *in vivo* porcine liver, and ~5.26 kPa for *in vivo* rat liver. Both our calculated elastic moduli and viscosity for porcine and rat livers are smaller than these reported literature values. One reason of this discrepancy could be due to the assumptions *e.g.* tissue homogeneity, density, the implemented model (Voigt model), as well as the detection scheme they used for calculating these values. Since micro-indentation was used in this study, some of these assumptions, *e.g.* density and homogeneity, can be ignored, even though liver tissue in not homogeneous [102]. Moreover, placing a tissue on a hard surface induces external forces, *i.e.* stress, that is not present in the *in vivo* state. Other factors such as capsules, blood flow, cellular association, and other *in vivo* conditions need to be taken into account for accurate measurements, and for our case, conditions for both rat and porcine liver were relatively identical. However, the mechanical properties were different when comparing the *ex vivo* values to those of TMP data and the physiological conditions explained earlier can be the reason for the dissimilarities.

Porcine gallbladder was another tissue that was characterized in this study for the purpose of differentiating its viscoelastic mechanical properties among other close organs, *i.e.* liver. As presented in table 8, the elastic modulus of gallbladder was ~2 kPa higher than the liver and there was a difference of ~20 seconds in the time constant calculations. During the tissue preparation,

excess bile was removed from the tissue to avoid slippage of the sphere indenter that could have affected the viscosity measurement. The standard error of the mean for both rat and porcine liver were very small due to consistency and the steadiness of the data; however, that value was a bit higher for the gallbladder and that could be due to the remnants of the bile that could not be removed, and the high tissue thickness of the samples. This illustrates the difference in the viscoelastic properties of the two tissues that are relatively close to one-another and can be used to differentiate the two using imaging modalities, *i.e.* vibroacoustography, that utilize tissue mechanical properties as a contrast mechanism. Clear boundary distinction can also be highlighted by the difference between viscoelastic properties of liver and gallbladder, two proximate organs to one another. This find along with imaging modalities that utilize this method, like VA, could lead to an ideal non-invasive approach for tissue identification and characterization in the field of medicine.

This study uses spherical-tip micro-indentation technique along with Hertzian model to analyze and characterize the generated data, with a relatively controlled protocol and numbers. Therefore, complete mechanical characterization that assess stress and strain rates, which bring the tissue to failure, for both *in vivo* and *ex vivo* cases are critical for establishment of mathematical models that accurately describes the viscoelastic mechanical properties for imaging modalities and material characterization.

### 4.4.6. Conclusion

This section focuses on characterization of the viscoelastic properties of TMPs and *ex vivo* animal hepatic tissues. TMPs can be synthesized to mimic the acoustic and mechanical properties of biological tissues, but accurate characterization and modeling still requires fresh biological tissues. This study investigated the mechanical behaviors of *ex vivo* hepatic tissues; however, direct

characterization and evaluation with other *ex vivo* and possible *in vivo* biological organs is still a necessity for further validation of mechanical properties. The conducted experiments in this study may bolster the possibility of using tissue mechanical properties, particularly viscoelasticity, as the primary contrast mechanism for new developing imaging modalities like VA. To this end, insights gained from assessment of animal hepatic tissues have helped researchers better understand their underlying mechanical behavior, but better *ex vivo* experimental setting, *i.e.* closer replication to *in vivo* physiological parameters, must be implemented for optimal findings. Nevertheless, characterization and evaluation of *ex vivo* animal hepatic tissues under micro-indentation techniques, among other mechanical techniques, may furnish additional information that can guide researchers and scientists in modeling and investigative approaches for tissue response under a static force. Given that biological tissues behave as viscoelastic materials, both viscosity and elasticity should be considered when examining them. In the medical field, palpation, the gold standard in detecting abnormalities, only utilizes the elasticity to characterize the tumor boundary regions and perhaps that can be the reason for the lack of quality of tissue differentiation in real-time procedures. In addition, soft target characterization may play a salient role in tissue imaging, *i.e.* vibroacoustography and elastography techniques, material characterization, and non-destructive testing (NDT), although more research needs to be completed to reinforce the potential of soft material mechanical behavior in the aforementioned fields.

# 5. Compact Vibroacoustgraphy Design

The goal of this chapter is to design a clinically versatile, compact vibroacoustography system for non-invasive boundary detection of malignant and normal tissues in intra-operative applications. Current techniques, including palpation and elastography, suffer from subjectivity, limited specificity, and lack of depth of penetration, and thus, are ineffective for real-time intra-operative use. VA has previously been used to image embedded objects in soft tissue with high contrast. However, *in vivo* compact VA systems have yet to be established for clinical use. As the first step in bringing compact quality VA imaging systems to the clinic, the proposed work in this chapter will focus on simulations of a small footprint VA system with two orientations of confocal transducer for systematic evaluation using different detection schemes.

## 5.1. Introduction

There have been key developments in medical imaging, such as elastography techniques and vibroacoustography that utilize both radiation force and mechanical properties of tissue (*i.e.* viscoelasticity) to generate contrast in detecting and characterizing tissue intra-operatively. Given the preliminary success of these technologies, there has been increasing demand for portable systems that bring imaging excellence -the ability to rapidly and reliably identify and localize tissue- into smaller operating spaces. This system requirement, however, remains to be fully realized in the medical field. Currently, surgical methods for intra-operative tissue discrimination are primarily based on palpation. Pre-operative imaging with MRI, CT, and ultrasound provide useful information but are difficult to apply in intra-operative setting. Ultrasound has a long history of intra-operative application but it also has its limitations. VA can improve over current ultrasound techniques by providing higher resolution and higher contrast images of various targets at greater depths of penetration. Several other techniques, such as Optical Coherence Tomography

(OCT) and MR Elastography (MRE), have been explored to address this issue, but lack of diagnostic efficacy renders these techniques sub-optimal for intra-operative use.

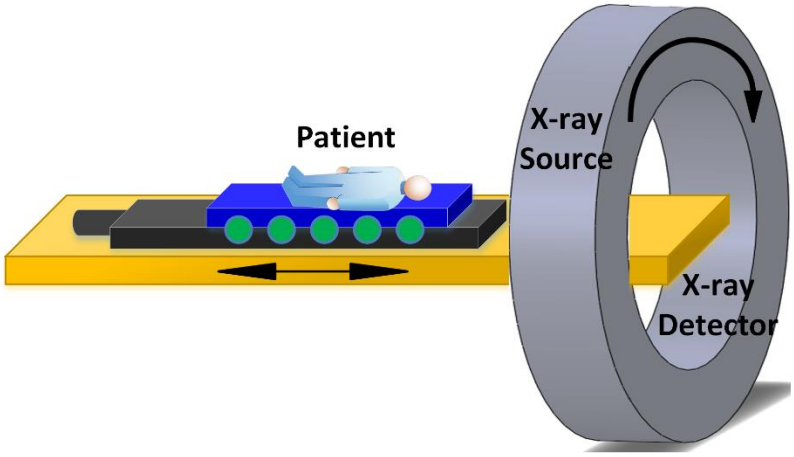


**Figure 31**: CT scan used for surgical planning during intra-operative procedures. Since an X-ray source is used to generate images, the physician and the patient need to wear a lead (Pb) vest for radiation protection which can cause discomfort for both the operator and patient.

In addition, VA is specifically designed to enhance boundary identification, making it ideal for intra-operative margin delineation. VA can be used in real-time in the surgical operating room. This could potentially save a great amount of time and effort from false margins during identification, and can increase the precision of procedures. Our group, in addition to others, has previously demonstrated the capability of VA systems for target distinction and evaluation of Tissue Mimicking Phantoms (TMPs) and *ex vivo* surgical resection specimens in an ultrasonic tank. However, a compact VA system for *in vivo* applications has not been demonstrated. This chapter will lay the groundwork for compact quality VA design by investigating confocal transducer orientations that provide both versatile and reliable detection schemes [1, 33, 42].

## 5.2. System

VA is a novel imaging modality that generates a map of the mechanical response of a target to an acoustic radiation force, usually in low kHz range. By focusing two sinusoidal ultrasound beams at two slightly different frequencies ($f_1$ and $f_2$, where $f_2 = f_1 + \Delta f$ ), a stress field at the beat frequency

is generated within a small volume of the object. In response to the applied oscillating force, the object vibrates and produces an acoustic emissions field, at the difference frequency, $\Delta f$, which is then detected by a highly sensitive hydrophone. The received acoustic emissions field amplitude is theoretically correlated to the mechanical properties of the object. Moreover, the detection scheme can be miniaturized by combining the transmitter and detector into one structure. In this case, a hole (~ 2.5 mm diameter of a miniaturized needle hydrophone), will be created in the center of the curved confocal transducer, and the beam pattern of the transducer will be evaluated. Figure 32 illustrates the two orientations that will be examined. The diameter as well the ROC of the curved confaocal transducer will be the same for both orienttaions and is the same as discussed in chapter 2.

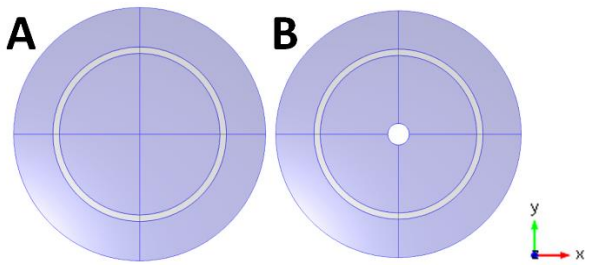


**Figure 32**: Sketches of the confocal transducer designs. A) Current confocal transducer orientation with no center hole, B) compact confocal transducer design with center hole for a needle hydrophone for acoustic detection.

## 5.3. Analysis and Results

Theoretical simulations of a compact *in vivo* VA system investigated its design parameters, such as depth of focus, beam profile, resolution limits, and focus volume, for future characterization and system development. The beam profile of two types of confocal transducers, one with a center hole and one without, were investigated using COMSOL multi-physics simulation software.

Figures 33 demonstrates individual beam patterns for each portion of the transducer, inner and outer, and two different orientations, with and without center hole.

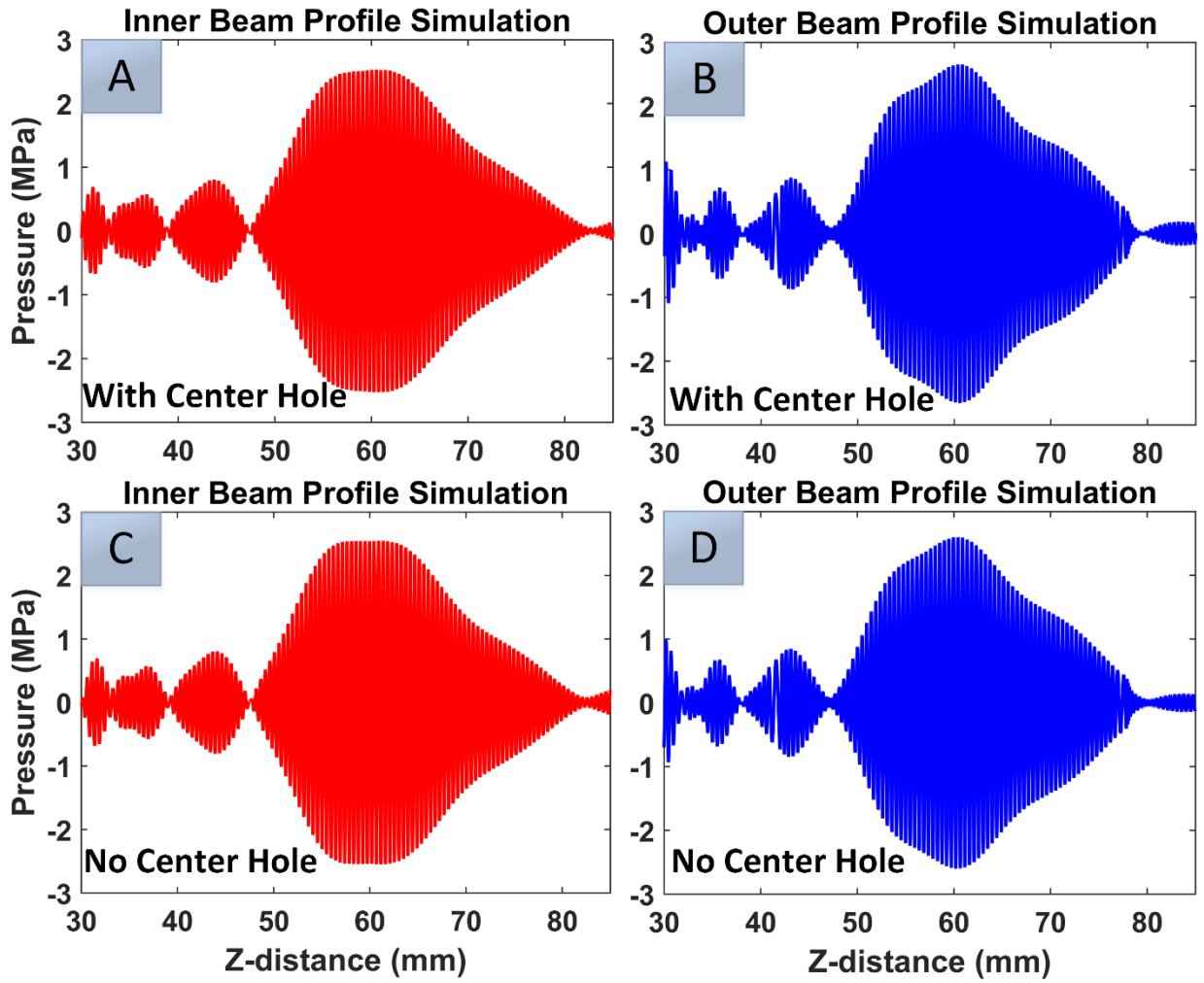


**Figure 33**: Simulation results of two different VA system orientation. Individual beam patterns for inner and outer part of the curved confocal transducer with center hole, A and B, and no center hole, C and D.

As illustrated, the overall pattern of the individual beam profiles for both portions of the confocal transducer in the discussed orientations are relatively the same; however, there were minute differences when the overall combined patterns were compared to one another. After individual inspections, the envelope of inner and outer beam profiles per configuration were added together and only the positive portion of the generated pressure waves were analyzed. Figure 34 denotes the Z-axis envelope beam profile of the two orientations. Insertion of a center hole shifted the

focus spot by 0.7mm and decreased the relative generated pressure by 1%. The decrease in generated pressure theoretically makes sense because the surface area that generates the acoustic pressure was decreased due to the presence of center hole. Moreover, the center hole was very small relative to the size of the transducer and as the figure indicates, the hole did not affect the focus spot and the overall pressure beam pattern of the transducer. Since the ROC of the transducer was ~60mm, ~ $\pm$ 15mm from the focused spot was analyzed for the beam profile comparison.

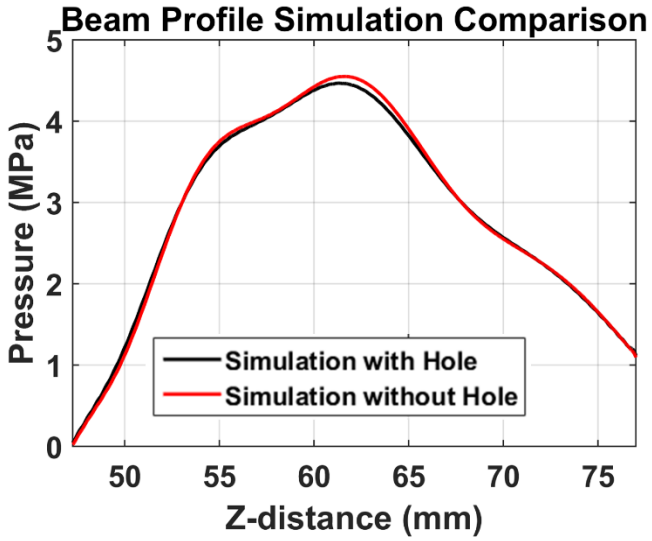


**Figure 34**: Z-axis beam profiles for two different orientations of the confocal transducer, no center hole and with center hole.

Further evaluations must be explored for development of a practical device. Current geometries that were simulated and analyzed had a ROC of ~60mm and outer diameter of ~45mm, albeit this geometry might be practical for large animal *in vivo* studies, smaller probes are preferred for human *in vivo* studies.

# 6. Mathematical Modeling of the Contrast Mechanism

Biological tissues are modeled as viscoelastic materials due to a manifestation of hysteresis on relaxation of the stress in stress vs. strain curves [88, 89]. Gelatin, agar, and PVA and other *ex vivo* pre-clinical models such as liver, gallbladder, and HNSCC specimens are appropriate representations of tissue substituents that were used in this work to establish the viscoelastic mechanical properties of targets as the dominant contrast mechanism for VA imagery. In the previous sections, Hertzian model and contact mechanics model were used to examine the viscosity, elastic moduli, and time constant of these materials under applied force and displacement. The results were then compared to VA signal intensity to generate a relationship between the two techniques [84, 88, 89]. An inverse relationship was demonstrated between VA signal intensity and elastic moduli of TMPs using contact mechanics, but a mathematical model that directly relates VA generated signals to mechanical properties has not been established. The purpose of this chapter is to develop a mathematical relationship based on target's geometry, mechanical properties, and acoustic properties to further investigate and verify the contrast mechanism of the VA imagery.

## 6.1. Viscoelasticity

The word viscoelastic is a combination of viscous fluidity and elastic solidity and thus materials under stress and/or strain exhibit both viscous and elastic behavior. Moreover, in modeling materials such as biological tissues, linear elastic Hookean spring, elasticity behavior, and linear viscous Newtonian Dash-pot, viscosity behavior, are used to examine and understand the performance of these materials under spring force and displacement. Various simple mechanical models such as Maxwell and Kelvin-Voigt models are used to describe this behavior. Following

figures represent the linear elastic spring and linear viscous Dash-pot in series, Maxwell model, and in parallel, Kelvin-Voigt model: [88, 89]:

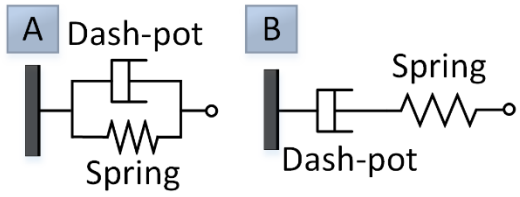


**Figure 35**: Dash-pot and spring combination in parallel (Kelvin-Voigt model), A, and in series (Maxwell model), B. Dash-pot represents pure viscous and spring represents pure elastic behavior.

The linear elastic spring relates stress, exerted force per unit area, to strain, changes in length with respect to its original length, in a linear fashion by elastic modulus, E, in solids. During the process, the material will go under an instantaneous deformation upon loading and an instantaneous de-straining upon unloading. Following equation will illustrate the relationship:

$$\sigma = E\,\varepsilon \tag{6.1}$$

where σ and ε represent stress (force per unit area) and strain (displacement per initial displacement), respectively. The linear viscous Dash-pot contains a piston-cylinder filled with a viscous fluid and by definition relates stress and strain by η, the viscosity of the materials, in a linear fashion for fluids. Following figure represents the linear elastic spring and linear viscous Dash-pot.

$$\sigma = \eta\,\varepsilon \tag{6.2}$$

## 6.2.Maxwell Model

The scenario of time dependence of viscoelastic response is similar to the time dependence of electrical circuits, and thus ordinary differential equations can be utilized to examine their characteristics. In Maxwell's model, Hookean spring and a Newtonian Dash-pot are connected in

series and so the stress on each element is the same and equal to the initial stress and the strain is the addition of each element [88, 89].

$$\sigma = \sigma_s = \sigma_d \tag{6.3}$$

$$\varepsilon = \varepsilon_s + \varepsilon_d = \frac{\sigma_s}{E} + \frac{\sigma_d}{\eta} \tag{6.4}$$

where $\sigma_s$ and $\varepsilon_s$ represent stress and strain of Hookean spring and $\sigma_d$ and $\varepsilon_d$ represent stress and strain of Newtonian Dash-pot, respectively. At equilibrium, the stress of each element will be the same, and by multiplying by E and substituting time constant, $\tau = \frac{\eta}{E}$, the total strain in Maxwell model becomes:

$$E\varepsilon = \sigma \left(1 + \frac{1}{\tau}\right) \tag{6.5}$$

One way to test the viscoelastic behavior of the target under Maxwell model is stress relaxation. In this test, the material initially will undergo constant strain, $\varepsilon_0$, equating to the initial condition of $\sigma_0 = E\varepsilon_0$. So, by integrating using variable separation, the total stress that was illustrated in equation 6.1 in Maxwell model becomes:

$$\sigma\,(t) = \sigma_0\, exp\left(\frac{-t}{\tau}\right) \tag{6.6}$$

The stress relaxation behavior is denoted by an exponential decay with time constant, $\tau$, which shows as the applied strain on the target decreases, the measured stress decreases in an exponential decay fashion. This shows the non-linear behavior of viscoelastic materials when under strain using Maxwell model.

## 6.3.Kelvin-Voigt Model

In Kelvin-Voigt's model, Hookean spring and a Newtonian Dash-pot are connected in parallel and so the strain on each element is the same and equal to the initial strain, while the stress is the

addition of the stress on each element [88, 89]. For this model, it is assumed that the elements will not bend in response to a force or displacement, so the strain on each element remains equal:

$$\varepsilon = \varepsilon_s = \varepsilon_d \tag{6.7}$$

$$\sigma = \sigma_s + \sigma_d = E\varepsilon + \eta\varepsilon = \varepsilon(E + \eta) \tag{6.8}$$

One way to test the viscoelastic behavior of the targets under Kelvin-Voigt model is by creep recovery test. In this test, the material is subjected to a constant stress, $\sigma_0$. After applying the constant stress, the spring will want to stretch, but it is held back by the Dash-pot due to its delayed reaction, so the stress is initially used by the Dash-pot and as a result the creep curve starts with an initial slope of $\frac{\sigma_0}{\eta}$. However, after a defined time period, the spring takes all the stress that was inputted and sets up an initial condition of $\varepsilon_0 = \frac{\sigma_0}{E}$ illustrating the deformation of a pure elastic element. Therefore, the total strain in the system using Kelvin-Voigt model:

$$\varepsilon(t) = \varepsilon_0\left(1 - exp^{\frac{-t}{\tau}}\right) \tag{6.9}$$

In this case, the system will undergo an initial stress causing an initial deformation, strain, in a period of $\tau$, retardation time, and then the stress is removed and the creep-recovery, strain, will be collected in an exponential decay fashion. The retardation time, $\tau$, is the same as the time constant in the Maxwell model. The shorter the retardation time, the faster the creep straining.

Moreover, when the load is removed from the target, the spring reacts instantaneously, but the Dash-pot cannot recover, and as a result there appears an elastic recovery.

## 6.4. Radiation Force of an Oscillating Sphere in a Viscoelastic Medium

As mentioned before, the resultant dynamic radiation force, $F_r(\Delta\omega)$ from an acoustic vibration field on a homogeneous isotropic sphere immersed in a homogeneous fluid, *i.e.* propagating medium, is given by:

$$F_{r(\Delta\omega)} = Sd_r\langle E\rangle \tag{6.10}$$

where $S = \pi r^2$ is the vibrated area of the target with radius of $r$, $\langle E\rangle = \frac{p(t)^2}{\rho_0 c^2}$ is the time averaged energy density of the ultrasonic waves with $p(t) = 2P_0[1 + \cos(\Delta\omega)\, t + \Delta\varphi]$ for vibroacoustography technique, and $d_r$ is the radiation force function that depends on the material properties of the target and the medium, usually expressed as a function of $k$, where *k* is the wave number of the incident wave, $\frac{2\pi}{\lambda}$, and r is the target's radius [37, 103, 104].

The velocity of an oscillating sphere in a viscoelastic medium using Oestreicher can be calculated as [104]:

$$V = \frac{F_r}{Z_r + Z_m} \tag{6.11}$$

where $Z_r$ and $Z_m$ are radiation and mechanical impedances, respectively. $Z_r$ can be defined as:

$$Z_r = -j\frac{4\pi r^3}{3}\rho\Delta\omega\left(\frac{\left(1 - \frac{3j}{rh} - \frac{3}{r^2h^2}\right) - 2\left(\frac{j}{rh} + \frac{1}{r^2h^2}\right)\left(3 - \frac{r^2k^2}{jrk+1}\right)}{\left(\frac{j}{rh} + \frac{1}{r^2h^2}\right)\frac{r^2k^2}{jrk+1} + \left(2 - \frac{r^2k^2}{jrk+1}\right)}\right) \tag{6.12}$$

$$k = \sqrt{\frac{\rho\Delta\omega^2}{(2\mu+\lambda)}}\ and\ h = \sqrt{\frac{\rho\Delta\omega^2}{\mu}} \tag{6.13}$$

where $\mu = \mu_1 + j\Delta\omega\mu_2$ and $\lambda = \lambda_1 + j\Delta\omega\lambda_2$ are Lamé's constants, ρ is the density of the medium, c is the speed of sound of the medium, $\mu_1$ and $\mu_2$ are the shear elasticity and viscosity of the medium, respectively, and $\lambda_1$ and $\lambda_2$ are the bulk elasticity and viscosity of the medium, respectively [37, 104]. Using Newton's second law, the resultant force on an object with mass $m$ and measured velocity $v$ is defined as:

$$F = m\frac{d}{dt}ve^{j\Delta\omega t} = jm\Delta\omega ve^{j\Delta\omega t} \tag{6.14}$$

The mechanical impedance is defined as the ratio of the applied force to the resulting velocity:

$$Z_m = \frac{-F}{ve^{j\Delta\omega t}} = -jm\Delta\omega = -j\frac{4\pi}{3}r^3\rho_s\Delta\omega \tag{6.15}$$

where the mechanical impedance is in terms of the object's volume, $\frac{4\pi}{3}r^3$, beat frequency, $\Delta\omega$, and object's density, $\rho_s$.

Using phasor notation for the calculated velocity, the velocity becomes:

$$V = \frac{|F_r|\angle\varphi_r}{|Z_r|\angle\varphi_r + |Z_m|\angle\varphi_m} = \left|\frac{F_r}{Z}\right|\angle\varphi_r - \angle\varphi_z \tag{6.16}$$

Based on the equations 6.11, 6.12, 6.15, and 6.16, we can calculate the shear velocity by the assumption of continuity, homogeneity, and isotropy of the medium for homogeneous isotropic targets of varying density over a range of beat frequencies.

## 6.5. Mathematical Model Formulation

As discussed in chapter one, the radiation force generated from the confocal transducer in VA technique is confined to a focus plane to image a target of interest. It is only at the focus spot that the beat frequency is generated from the intersection of two CW ultrasonic waves. As a result of this generation, the object will vibrate at the beat frequency, $\Delta\omega$, and start emitting acoustic radiation that is a function of its geometry, surrounding medium, and mechanical and acoustic properties. The relationship between the emitted acoustic radiation pressure and the object is as follows:

$$P_{(\Delta\omega)}(\vec{r}) = \rho_0 c^2 H_{(\Delta\omega)}(l) Q_{(\Delta\omega)}(\vec{r}) F_{r(\Delta\omega)} \tag{6.17}$$

where the detected pressure, $P_{\Delta\omega}$,is in terms of medium density, $\rho_0$, speed of sound in the medium, $c$, medium transfer function, $H_{(\Delta\omega)}(l)$, the radiation force, $F_{(\Delta\omega)}$, and $Q_{\Delta\omega}(\vec{r})$, total acoustic outflow by an object per unit force which itself is in terms of the ultrasound pressure, $P$, and the ultrasound characteristics of the object, $Y$, and $(\vec{r})$, a radial vector on the focal plane The function $Q_{\Delta\omega}(\vec{r})$ includes target's vibrating area, geometry, and its mechanical impedance. The mechanical impedance itself has two components: one arising from inertia, *i.e.* geometry and mass, $m$, friction, and viscoelasticity, *i.e.* elastic moduli, $E$, and viscosity, $\eta$ [14, 49]

$$Q_{\Delta\omega}(\vec{r}) = \frac{A}{(Z_m + Z_r)} \tag{6.18}$$

equation 6.18 demonstrates that the generated acoustic radiation pressure is dependent on both mechanical and radiation impedance of the target as well as the area of the target, $A$. In the case of radiation impedance, the target is assumed to be a rigid piston with radius *r* set in a plane wall. Therefore, based on Morse [105], the radiation impedance will become:

$$Z_r = \pi r^2 (R_r - jX_r) \tag{6.19}$$

$$\begin{aligned} &where\ R_r = \rho c \left[1 - \frac{c}{\Delta\omega r} J_1\left(\frac{c}{2\Delta\omega r}\right)\right]\ and \\ &X_r = \frac{4\rho c}{\pi} \int_0^{\frac{\pi}{2}} sin\left[\frac{2r\Delta\omega}{c} cos\,\alpha\right] sin^2(\alpha) d\alpha \end{aligned} \tag{6.20}$$

The real part of the radiation impedance, $R_r$, is in terms of the beat frequency, $\Delta\omega$, medium acoustic properties, $\rho c$, and $J_1(a)$, the first order Bessel function of the first kind. The imaginary part, $X_r$, is in terms of α, which represents the angle between the detector and the center of the target. Both parts in the radiation impedance are in terms of $\left(\frac{r\Delta\omega}{c}\right)$ and in the case of small targets:

$$As\,\frac{2\Delta\omega a}{c} < 0.5 \;\longrightarrow R_r = \frac{\Delta\omega^2 a^2}{2c^2}\; and\; as\,\frac{2\Delta\omega a}{c} < 1 \longrightarrow X_r = \frac{8\omega a}{3\pi c} \qquad (6.21)$$

Therefore, the radiation frequency term becomes a constant for small targets.

In the case of mechanical impedance, $Z_m$, the general solution based on Morse [105] becomes:

$$Z_m = R_m - jX_m = R_m - j\left(m\Delta\omega - {}^{k}/_{\Delta\omega}\right) \qquad (6.22)$$

where $R_m$ represents the mechanical resistance analogous to electrical resistance and damper (viscosity in Dash-pot), $m$ represents the mass analogous to electrical inductance and mass of the target, $k$ represents the stiffness analogous to capacitor and spring constant (elasticity), and $\Delta\omega$ represents the beat frequency at the focus plane.

The last term in equation 6.17 is $H_{(\Delta\omega)}(l)$, the medium transfer function, which is in terms of the target's radius, observation point, acoustic properties of the medium, and boundary conditions based on Morse derivation [22, 105] is:

$$H_{(\Delta\omega)}(l) = j\frac{\Delta\omega}{c^2}\left[\frac{\exp\left(\frac{j\Delta\omega l}{c}\right)}{4\pi l}\left(\frac{2J_1\left(\frac{\Delta\omega r}{c}sin\vartheta\right)}{\frac{\Delta\omega r}{c}sin\vartheta}x\frac{cos\vartheta}{cos\vartheta + \frac{\rho_0 c}{Z_B}}\right)\right] \qquad (6.23)$$

where $l$ is the distance from the observation point, detector, to the center of the target, $\vartheta$, is the angle between the observation and the imaging axis, of the curved transducer, and $Z_B$ is the acoustic impedance of the boundary, the ratio between the pressure and the normal fluid velocity at a point on the target.

As discussed in this work, the generated acoustic pressure depends on the medium transfer function, $H_{(\Delta\omega)}(l)$, radiation force, $F_{r(\Delta\omega)}$, and the acoustic outflow, $Q_{\Delta\omega}(\vec{r})$; however, the only parameter that includes the mechanical properties of target, *i.e.* elasticity and viscosity, is the

imaginary part of the mechanical impedance of the acoustic outflow parameter. The final expression for the generated acoustic pressure is as follows:

$$P_{\Delta\omega} = j\frac{\Delta\omega}{c^2} d_r p(t)^2 S \left[\frac{\exp\left(\frac{j\Delta\omega l}{c}\right)}{4\pi l}\left(\frac{2J_1\left(\frac{\Delta\omega r}{c} sin\vartheta\right)}{\frac{\Delta\omega r}{c} sin\vartheta} x \frac{cos\vartheta}{cos\vartheta + \frac{\rho_0 c}{Z_B}}\right)\right]\frac{A}{(Z_m + Z_r)} \quad (6.24)$$

where $p(t)^2$ is the amplitude of the incoming ultrasonic waves, $d_r$ is the radiation force function, S is the vibrated area of the target, and A is the surface area of the vibrated target, which in a case of small targets, *i.e.* $\left(\frac{r\Delta\omega}{c}\right) \rightarrow small$, they are assumed to be the same. Moreover, the generated acoustic pressure in equation 6.24 is inversely proportional to $Z_m$, the only factor that includes the stiffness, *k*, of the target, and further confirms our experimental results in chapter 4. However, to directly evaluate the effect of viscoelasticity of the target as a function of the beat frequency, the acoustic outflow needs to be examined. So, the behavior of targets with different densities, illustrating different tissue constituents, were simulated to determine the resonant beat frequency for each constituent.

## 6.6. Simulation Results and Discussion

For this simulation, human adipose tissue, soft tissue, and muscle in spherical shapes were chosen to mimic actual scenarios when imaging human tissue. The acoustic outflow of each type was compared as a function of their generated resonant frequency peak. The three tissues had water with $\rho = 1000\,\frac{kg}{m^3}$ and $c = 1500\,m/s$ as their propagating media for the ultrasonic waves. The spherical geometry was chosen to ensure isotropic homogeneity for simplification of calculations. In terms of radiation impedance, $Z_r$, it was assumed to be a constant since the spherical targets, $r = 500\,\mu m$, were much smaller than the wavelength of the beat frequency range, 1-100 kHz. For these three tissue types, the real part of the acoustic outflow, $R_m$, was assumed to be zero for all

types. For the imaginary part, adipose tissue was assumed to have $\rho = 950\frac{kg}{m^3}$ and $k = 1 - 20\ kPa$, soft tissue $\rho = 1043\frac{kg}{m^3}$ and $k = 20 - 50\ kPa$, and muscle $\rho = 1050\frac{kg}{m^3}$ and $k = 50 - 100\ kPa$, respectively. These values were based on given density and elastic modulus[64]. Figure 36 represents the generated results from this simulation. As apparent, as the targets become stiffer, *i.e.* increase in density as well as elastic modulus, the peak resonant frequency for each tissue type increases. This positive correlation was shown in section 4.3 in TMPs and is now confirmed by the results of this simulation. Moreover, this will eventually lead to the characterization of tissue stiffness and creation of databases for tissue vibroacoustic responses based on their mechanical properties.

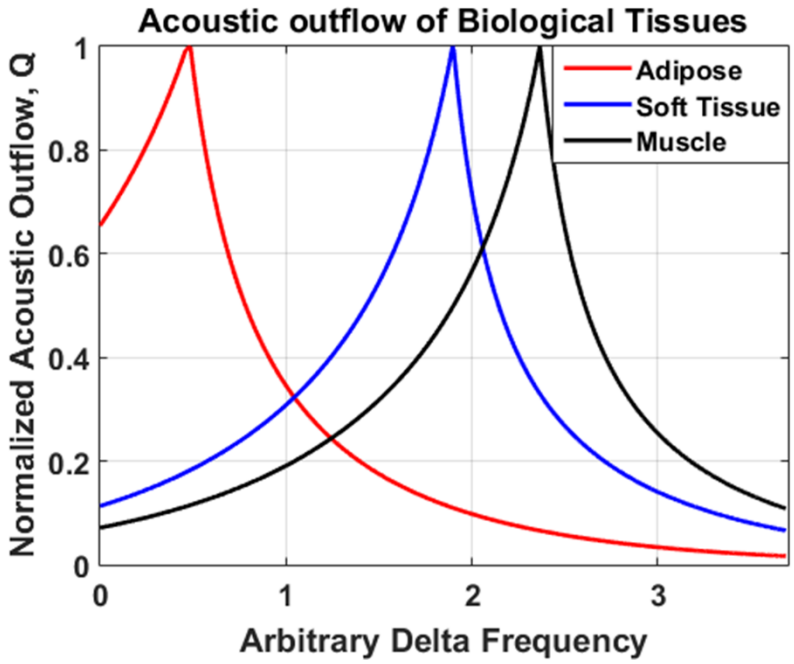


**Figure 36**: Acoustic outflow of biological tissues, specifically adipose, soft tissue, and muscle, as a function of resonant beat frequency. As the tissue becomes stiffer, the delta frequency, resonance peak, start to increase.

## 6.7. Simulation Summary

The simulation results in the chapter verify the hypothesis that the tissue viscoelastic properties are the primary contrast mechanism in the generation of VA signal in the vibroacoustography

imaging system. A positive correlation between mechanical properties of tissues and the beat frequency was observed. The simulation results in various human tissue constituents illustrated in this chapter as well as tissue mimicking phantom results in section 4.3 show a good proof of concept. This may further help with the future investigation of the VA resonant frequency characterization for different tissue types for the creation of databases for future VA technique investigations.

# 7. Conclusion and Future Directions

This dissertation primarily focused on the fundamental understanding and verification of the main contrast mechanism, viscoelastic properties of targets, of the vibroacoustography (VA) technique. After fabrication and development of the VA system in chapter 2, the important parameters of the system such as PSF, MTF, sensitivity, and specificity in imaging potential targets were evaluated and characterized in chapter 3. Establishing ideal system parameters in imaging biological tissues directed the way to examine the profile and to enhance the boundaries of imaging targets to further establish VA as a potential imaging modality in distinguishing regions with different mechanical properties during intra-operative surgical procedures, chapter 4. After attaining preliminary data, a parallel correlation study was completed between two techniques with comparable sensing schemes to correlate the VA signal intensity to the absolute elasticity measurements using a direct force/displacement technique. This correlation study resulted in an inverse correlation between VA signal intensity and the elastic moduli of TMPs, which paved the way for the future experiments in chapter 4. Following this, spherical-tip micro-indentation using Hertzian model, similar technique to force/displacement measurement, was used to further examine other mechanical parameters, *i.e.* viscosity and time constant, of pre-clinical models like hepatic animal tissues and TMPs. VA feasibility was evaluated in aforementioned models, and so the generated results in chapters 3 and 4 paved the way to miniaturize the VA system for intra-operative surgical applications, chapter 5. Simulations for the new VA probe design showed minor discrepancies from the characterized system in chapters 2 and 3. The results in chapter 5 provided preliminary works in the compact system implementation and will help in the future fabrication and characterization process of the miniature VA system.

The accomplishments in this dissertation were further summarized in chapter 6, mathematical modeling of the contrast mechanism. Preliminary results suggested viscoelasticity plays a crucial role in the contrast mechanism of VA and satisfied the hypothesis that was formulated when the technique gained clinical traction in the late 1990s. This model confirmed the inverse relationship between VA signal intensity and mechanical properties of targets that was generated in chapter 4. The mathematical model also generated a relationship between the output signal to the medium acoustic effect, input pressure, and acoustic outflow. It also established how mechanical properties and geometry of the intended targets generate contrast for the VA imagery.

The future goal of my scientific work is to implement the demonstrated technique in this dissertation into an array of elements to further investigate its feasibility in clinical applications and to gain clinical traction from major medical imaging companies. This technique has a potential in optimizing image-guided approaches for real-time imagery and can potentially resolve small abnormalities that are otherwise undetectable by conventional methods in tumor excision applications. Moreover, with the ability to measure both amplitude and phase in the intended tissue as shown in this work, more information from the tissue can be extracted for quantified investigations. VA can be used to provide more quantitative measurements of the viscoelastic properties of various tissues and can potentially establish a database for tissue response to a low frequency perturbation for future tissue characterization and investigations.

Furthermore, the utility of efforts that originate from VA viscoelasticity maps are immense for the preservation of healthy tissues around diseased regions in tumor excision surgical procedures and can provide supreme quantitative measurements of abnormalities within vital organs that can increase patients' healthcare. The information presented in this dissertation can assist with

effective translation of VA technology into clinical settings and perhaps can gain industry attraction for commercialization of the technology.

## 7.1. Summary of Achievements and Accomplishments

This project cultivated many achievements including conference proceedings, abstract presentations, peer-reviewed journal articles, and a provisional patent. The list of these accomplishments are as follows:

**Peer-reviewed Journal Articles**

**A. Maccabi**, Z. Taylor, N. Bajwa, J. Mallen-St Clair, M. St John, S. Sung, W. Grundfest, and G. Saddik. "An examination of the elastic properties of tissue-mimicking phantoms using vibro-acoustography and a muscle motor system." Review of Scientific Instruments 87, no. 2 (2016): 024903.

**Ashkan Maccabi**, Nikan K. Namiri, Neha Bajwa, Suraj A. Dhanjani, Shijun Sung, Zachary D. Taylor, Maie A. St. John, Warren S. Grundfest, and George N. Saddik. “Sensitivity and resolution performance limits of a vibroacoustographic system.” IEEE Transactions on Ultrasonics, Ferroelectrics, and Frequency Control. In Review.

**Ashkan Maccabi**, Andrew Shin, Nikan K. Namiri, Neha Bajwa, Maie St. John, Zachary D. Taylor, Warren S. Grundfest, and George N. Saddik. “Quantitative characterization of viscoelastic behavior in tissue mimicking phantoms and ex vivo animal hepatic tissues.” Journal of Biomechanics. In Review.

**Conference Proceedings**

**A. Maccabi**, J. Garritano, A. Arshi, G. Saddik, B. A. Tajudeen, M. St John, W. S. Grundfest, and Z. D. Taylor. "Ex vivo viscoelastic characterization of head and neck tissue abnormalities using ultrasound-stimulated vibro-acoustography (USVA)." In SPIE Medical Imaging, pp. 904006-904006. International Society for Optics and Photonics, 2014.

**A. Maccabi**, A. Arshi, J. Garritano, G. Saddik, E. Kohanbash, B. A. Tajudeen, M. St John, W. S. Grundfest, and Z. D. Taylor. "Ultrasound-stimulated vibro-acoustography for high-resolution differentiation based on viscoelastic properties of tissue mimicking phantoms." Studies in health technology and informatics 196 (2013): 262-264.

**Conference Abstracts**

N. Namiri, **A. Maccabi**, N. Bajwa, M. St. John, G. Saddik, Z. Taylor, and W. Grundfest. "Vibroacoustography system characterization using parallel difference frequency and elasticity measurements for potential applications in tumor margin detection." Biomedical Engineering Society (BMES) Annual Meeting. 2016 Oct 5-8, Minneapolis, MN.*

**Ashkan Maccabi**, Yiwen Meng, Nikan Namiri, Zachary Taylor, Maie St. john, Warren Grundfest, George Saddik. "Compact Vibroacoustography (VA) System Design and Characterization." 38th IEEE Engineering in Medicine and Biology (EMBC). 2016 Aug 16-20; Orlando, FL.

**A. Maccabi**, G.N. Saddik, N. Bajwa, M. St. John, W.S. Grundfest. "Characterization of the elasticity of embedded objects in PVA phantoms using USVA." 14th UC Systemwide Bioengineering Symposium; 2013 Jun 19-21; San Diego, CA.

*This abstract was awarded best Undergraduate Design and Research Award for the BMES Annual Meeting.

**Invention Disclosure**

Warren Grundfest, Maie St. John, **Ashkan Maccabi**, George N. Saddik, Zachary D. Taylor. Multi Frequency Harmonic Acoustography for Target Identification and Border Detection. The Regents of the University of California, a California Corporation, assignee. Patent UC. Case No. UC-2017-223-2-LA. Oct. 2016.

# 8. References


1. Fatemi, M. and J.F. Greenleaf, *Vibro-acoustography: An imaging modality based on ultrasound-stimulated acoustic emission.* Proceedings of the National Academy of Sciences of the United States of America, 1999. **96**(12): p. 6603–6608.

2. Das, D., et al., *Elastography: the next step.* Journal of Oral Science, 2011. **53**(2): p. 137-141.

3. Itoh, A., et al., *Breast Disease: Clinical Application of US Elastography for Diagnosis.* Radiology, 2006. **239**(2): p. 341-50.

4. Garra, B.S., et al., *Elastography of breast lesions: initial clinical results.* Radiology, 1997. **202**(1): p. 79-86.

5. Krouskop, T.A., et al., *Elastic moduli of breast and prostate tissues under compression.* Ultrasonic imaging, 1998. **20**(4): p. 260-274.

6. Schaar, J.A., et al., *Intravascular palpography for high-risk vulnerable plaque assessment.* Herz, 2003. **28**(6): p. 488-495.

7. Kademani, D., *Oral Cancer.* Mayo Clinic Proceedings, 2007. **82**(7): p. 878-887.

8. Seiwert, T. and E. Cohen, *State-of-the-art management of locally advanced head and neck cancer.* British Journal of Cancer, 2005. **92**(8): p. 1341-1348.

9. A.M., M., et al., *Oral cancer in 57,518 industrial workers of Gujarat, India: a prevalence and followup study.* Cancer, 1976. **37**(4): p. 1882-6.

10. Vahabi, M., *Breast cancer screening methods: a review of the evidence.* Health Care for Women International, 2003. **24**(9): p. 773-793.

11. Askeland, D.R. and P.P. Phulé, *The science and engineering of materials.* 2003.

12. Kruse, S., et al., *Tissue characterization using magnetic resonance elastography: preliminary results*.* Physics in medicine and biology, 2000. **45**(6): p. 1579.

13. Fatemi, M. and J.F. Greenleaf, *Probing the dynamics of tissue at low frequencies with the radiation force of ultrasound.* Physics in medicine and biology, 2000. **45**(6): p. 1449.

14. Fatemi, M. and J.F. Greenleaf, *Imaging the viscoelastic properties of tissue*, in *Imaging of Complex Media with Acoustic and Seismic Waves*. 2002, Springer. p. 257-276.

15. Papadakis, E.P., *Ultrasonic instruments and devices: reference for modern instrumentation, techniques, and technology*. 1999: Springer Science & Business.

16. Fatemi, M. and J.F. Greenleaf, *Vibro-acoustography: An imaging modality based on ultrasound-stimulated acoustic emission.* Proceedings of the National Academy of Sciences, 1999. **96**(12): p. 6603-6608.

17. Ophir, J., et al., *Elastography: a quantitative method for imaging the elasticity of biological tissues.* Ultrasonic imaging, 1991. **13**(2): p. 111-134.

18. Hasegawa, H. and H. Kanai, *Improving accuracy in estimation of artery-wall displacement by referring to center frequency of RF echo.* IEEE transactions on ultrasonics, ferroelectrics, and frequency control, 2006. **53**(1): p. 52-63.

19. Viola, F. and W.F. Walker, *A spline-based algorithm for continuous time-delay estimation using sampled data.* IEEE transactions on ultrasonics, ferroelectrics, and frequency control, 2005. **52**(1): p. 80-93.

20. Zheng, Y., et al., *Detection of tissue harmonic motion induced by ultrasonic radiation force using pulse-echo ultrasound and Kalman filter.* IEEE transactions on ultrasonics, ferroelectrics, and frequency control, 2007. **54**(2): p. 290-300.

21. Ganne-Carrié, N., et al., *Accuracy of liver stiffness measurement for the diagnosis of cirrhosis in patients with chronic liver diseases.* Hepatology, 2006. **44**(6): p. 1511-1517.

22. Fatemi, M., A. Manduca, and J.F. Greenleaf, *Imaging elastic properties of biological tissues by low-frequency harmonic vibration.* Proceedings of the IEEE, 2003. **91**(10): p. 1503-1519.

23. Pijpers, R., et al., *Vital dye and radiolabelled colloids—complement or alternative*, in *Lymphatic Metastasis and Sentinel Lymphonodectomy*. 2000, Springer. p. 130-137.

24. Nolte, D.D., *Optical interferometry for biology and medicine*. Vol. 1. 2011: Springer Science & Business Media.

25. Maslov, K., et al., *Optical-resolution photoacoustic microscopy for in vivo imaging of single capillaries.* Optics letters, 2008. **33**(9): p. 929-931.

26. Kennedy, B.F., K.M. Kennedy, and D.D. Sampson, *A review of optical coherence elastography: fundamentals, techniques and prospects.* Ieee Journal of Selected Topics in Quantum Electronics, 2014. **20**(2): p. 272-288.

27. Ferry, J.D., *Viscoelastic properties of polymers*. 1980: John Wiley & Sons.

28. Gao, G., S. Yang, and D. Xing, *Viscoelasticity imaging of biological tissues with phase-resolved photoacoustic measurement.* Optics letters, 2011. **36**(17): p. 3341-3343.

29. Jacques, S.L. and S.J. Kirkpatrick, *Acoustically modulated speckle imaging of biological tissues.* Optics letters, 1998. **23**(11): p. 879-881.

30. Schmitt, J.M., *OCT elastography: imaging microscopic deformation and strain of tissue.* Optics express, 1998. **3**(6): p. 199-211.

31. Sun, C., B. Standish, and V.X. Yang, *Optical coherence elastography: current status and future applications.* Journal of biomedical optics, 2011. **16**(4): p. 043001-043001-12.

32. Westervelt, P.J., *Scattering of sound by sound.* The Journal of the Acoustical Society of America, 1957. **29**(2): p. 199-203.

33. Maccabi, A., et al. *Ex vivo viscoelastic characterization of head and neck tissue abnormalities using ultrasound-stimulated vibro-acoustography (USVA)*. in *SPIE Medical Imaging*. 2014. International Society for Optics and Photonics.

34. Fatemi, M. and J.F. Greenleaf, *Ultrasound-stimulated vibro-acoustic spectrography.* Science, 1998. **280**(5360): p. 82-85.

35. W Urban, M., et al., *A review of vibro-acoustography and its applications in medicine.* Current medical imaging reviews, 2011. **7**(4): p. 350-359.

36. Fatemi, M. and J.F. Greenleaf, *Probing the dynamics of tissue at low frequencies with the radiation force of ultrasound.* Physics in Medicine and Biology, 2000. **45**(6).

37. Urban, M.W., *Multifrequency ultrasound radiation force excitation and motion detection of harmonically vibrating scatterers*. 2007, Citeseer.

38. Alizad, A., et al., *Potential applications of vibro-acoustography in breast imaging.* Technology in cancer research & treatment, 2005. **4**(2): p. 151-157.

39. Alizad, A., et al., *Critical issues in breast imaging by vibro-acoustography.* Ultrasonics, 2006. **44**: p. e217-e220.

40. Pislaru, C., et al., *In vivo vibroacoustography of large peripheral arteries.* Investigative radiology, 2008. **43**(4): p. 243.

41. Maccabi, A., et al., *Ultrasound-stimulated vibro-acoustography for high-resolution differentiation based on viscoelastic properties of tissue mimicking phantoms.* Studies in health technology and informatics, 2014. **196**: p. 262.

42. Maccabi, A., et al., *An examination of the elastic properties of tissue-mimicking phantoms using vibro-acoustography and a muscle motor system.* Review of Scientific Instruments, 2016. **87**(2): p. 024903.

43. Alizad, A., et al., *Application of vibro-acoustography in prostate tissue imaging.* Medical physics, 2013. **40**(2): p. 022902.

44. Urban, M.W., et al., *Implementation of vibro-acoustography on a clinical ultrasound system.* IEEE transactions on ultrasonics, ferroelectrics, and frequency control, 2011. **58**(6): p. 1169-1181.

45. Yuan, H. and B.B. Guzina, *Topological sensitivity for vibro-acoustography applications.* Wave Motion, 2012. **49**(8): p. 765-781.

46. Yamamoto, N., et al., *Diagnosis of small partial-thickness rotator cuff tears using vibro-acoustography.* Journal of Medical Ultrasonics, 2015. **42**(1): p. 3-7.

47. Kamimura, H.A., et al., *Vibroacoustography for the assessment of total hip arthroplasty.* Clinics, 2013. **68**(4): p. 463-468.

48. Alizad, A., et al., *In vivo thyroid vibro-acoustography: a pilot study.* BMC medical imaging, 2013. **13**(1): p. 1.

49. Alizad, A., et al., *Imaging mass lesions by vibro-acoustography: modeling and experiments.* IEEE transactions on medical imaging, 2004. **23**(9): p. 1087-1093.

50. Fatemi, M. and J.F. Greenleaf, *Application of Radiation Force in Noncontact Measurement of the Elastic Parameters.* Ultrasuound Imaging, 1999. **21**(2): p. 147-154.

51. Urban, M.W., et al., *Multifrequency Vibro-Acoustography.* IEEE Transactions on Medical Imaging, 2006. **25**(10): p. 1284-1295.

52. Mhala, M., P. Decai, and G. Kumar. *Broadband Impedance Matching Network for RF Power Amplifiers*. in *National Conf. on Communications*. 2008.

53. Brounley, R.W., *Matching networks for power amplifiers operating into high VSWR loads.* HF Electronics, 2004: p. 58-62.

54. Pozar, D.M., *Microwave engineering*. 2009: John Wiley & Sons.

55. Haughey, B. and K. Robbins, *Biology of Head & Neck Cancer.* Cummings Otolaryngology: Head & Neck Surgery, 5th ed. Elsevier Inc.

56. Kharine, A., et al., *Poly (vinyl alcohol) gels for use as tissue phantoms in photoacoustic mammography.* Physics in medicine and biology, 2003. **48**(3): p. 357.

57. Manohar, S., et al. *Photoacoustic imaging of inhomogeneities embedded in breast tissue phantoms*. in *Biomedical Optics 2003*. 2003. International Society for Optics and Photonics.

58. Xia, W., et al., *Poly (vinyl alcohol) gels as photoacoustic breast phantoms revisited.* Journal of biomedical optics, 2011. **16**(7): p. 075002-075002-10.

59. Fatemi, M. and J.F. Greenleaf, *Imaging the Viscoelastic Properties of Tissue*, in *Imaging of Complex Media with Acoustic and Seismic Waves*. 2002, Springer Berlin Heidelberg. p. 257-276.

60. Ma, T., et al. *Acoustic radiation force optical coherence elastography using vibro-acoustography*. in *SPIE BiOS*. 2015. International Society for Optics and Photonics.

61. Zysk, A.M., et al., *Optical coherence tomography: a review of clinical development from bench to bedside.* Journal of biomedical optics, 2007. **12**(5): p. 051403-051403-21.

62. Chen, S., et al., *Comparison of stress field forming methods for vibro-acoustography.* Ultrasonics, Ferroelectrics, and Frequency Control, IEEE Transactions on, 2004. **51**(3): p. 313-321.

63. Urban, M.W., et al., *Multifrequency vibro-acoustography.* Medical Imaging, IEEE Transactions on, 2006. **25**(10): p. 1284-1295.

64. Culjat, M.O., et al., *A review of tissue substitutes for ultrasound imaging.* Ultrasound in medicine & biology, 2010. **36**(6): p. 861-873.

65. Hall, T.J., et al., *Phantom materials for elastography.* Ultrasonics, Ferroelectrics, and Frequency Control, IEEE Transactions on, 1997. **44**(6): p. 1355-1365.

66. Dunmire, B., et al., *Characterizing an agar/gelatin phantom for image guided dosing and feedback control of high-intensity focused ultrasound.* Ultrasound in medicine & biology, 2013. **39**(2): p. 300-311.

67. Wells, P.N. and H.-D. Liang, *Medical ultrasound: imaging of soft tissue strain and elasticity.* Journal of the Royal Society Interface, 2011. **8**(64): p. 1521-1549.

68. Bushberg, J.T. and J.M. Boone, *The essential physics of medical imaging*. 2011: Lippincott Williams & Wilkins.

69. Alizad, A., et al., *Performance of vibro-acoustography in detecting microcalcifications in excised human breast tissue: A study of 74 tissue samples.* Medical Imaging, IEEE Transactions on, 2004. **23**(3): p. 307-312.

70. Urban, M.W., et al., *A review of vibro-acoustography and its applications in medicine.* Current medical imaging reviews, 2011. **7**(4): p. 350.

71. Lodder, W.L., et al., *Tumour thickness in oral cancer using an intra-oral ultrasound probe.* European radiology, 2011. **21**(1): p. 98-106.

72. Mashberg, A. and A.M. Samit, *Early detection, diagnosis, and management of oral and oropharyngeal cancer.* CA: a cancer journal for clinicians, 1989. **39**(2): p. 67-88.

73. Malaowalla, A., et al., *Oral cancer in 57,518 industrial workers of Gujarat, India. A prevalence and followup study.* Cancer, 1976. **37**(4): p. 1882-1886.

74. Aguiló, M., et al., *An inverse problem approach for elasticity imaging through vibroacoustics.* Medical Imaging, IEEE Transactions on, 2010. **29**(4): p. 1012-1021.

75. Jiang, S., S. Liu, and W. Feng, *PVA hydrogel properties for biomedical application.* Journal of the mechanical behavior of biomedical materials, 2011. **4**(7): p. 1228-1233.

76. Madsen, E.L., et al., *Tissue-mimicking agar/gelatin materials for use in heterogeneous elastography phantoms.* Physics in medicine and biology, 2005. **50**(23): p. 5597.

77. Cao, R., et al., *Tissue mimicking materials for the detection of prostate cancer using shear wave elastography: A validation study.* Medical physics, 2013. **40**(2): p. 022903.

78. Cournane, S., et al., *Assessment of the accuracy of an ultrasound elastography liver scanning system using a PVA-cryogel phantom with optimal acoustic and mechanical properties.* Physics in medicine and biology, 2010. **55**(19): p. 5965.

79. Zell, K., et al., *Acoustical properties of selected tissue phantom materials for ultrasound imaging.* Physics in medicine and biology, 2007. **52**(20): p. N475.

80. Qu, Y., et al. *Acoustic radiation force optical coherence elastography using vibro-acoustography*. in *SPIE BiOS*. 2015. International Society for Optics and Photonics.

81. Qi, W., et al., *Phase-resolved acoustic radiation force optical coherence elastography.* Journal of biomedical optics, 2012. **17**(11): p. 110505-110505.

82. Sneddon, I.N., *The relation between load and penetration in the axisymmetric Boussinesq problem for a punch of arbitrary profile.* International Journal of Engineering Science, 1965. **3**(1): p. 47-57.

83. Mitri, F.G., J.F. Greenleaf, and M. Fatemi, *Chirp imaging vibro-acoustography for removing the ultrasound standing wave artifact.* IEEE transactions on medical imaging, 2005. **24**(10): p. 1249-1255.

84. Yoo, L., et al., *Characterization of ocular tissues using microindentation and hertzian viscoelastic models.* Investigative ophthalmology & visual science, 2011. **52**(6): p. 3475-3482.

85. Mitri, F.G., P. Trompette, and J.-Y. Chapelon, *Detection of object resonances by vibro-acoustography and numerical vibrational mode identification.* The Journal of the Acoustical Society of America, 2003. **114**(5): p. 2648-2653.

86. Mitri, F.G., P. Trompette, and J.-Y. Chapelon, *Improving the use of vibro-acoustography for brachytherapy metal seed imaging: a feasibility study.* IEEE transactions on medical imaging, 2004. **23**(1): p. 1-6.

87. Siegel, R., C. DeSantis, and A. Jemal, *Colorectal cancer statistics, 2014.* CA: a cancer journal for clinicians, 2014. **64**(2): p. 104-117.

88. Roylance, D., *Engineering viscoelasticity.* Department of Materials Science and Engineering–Massachusetts Institute of Technology, Cambridge MA, 2001. **2139**: p. 1-37.

89. Kelly, P., *Solid Mechanics.* Part, 2008. **1**: p. 301-313.

90. Mattice, J.M., et al., *Spherical indentation load-relaxation of soft biological tissues.* Journal of Materials Research, 2006. **21**(08): p. 2003-2010.

91. Chua, W.K. and M.L. Oyen, *Viscoelastic properties of membranes measured by spherical indentation.* Cellular and Molecular Bioengineering, 2009. **2**(1): p. 49-56.

92. Oyen, M.L., *Spherical indentation creep following ramp loading.* Journal of Materials Research, 2005. **20**(08): p. 2094-2100.

93. Shin, A., L. Yoo, and J.L. Demer, *Viscoelastic Characterization of Extraocular Z-MyotomyBiomechanics of Z-Myotomy.* Investigative ophthalmology & visual science, 2015. **56**(1): p. 243-251.

94. Hamhaber, U., et al., *Comparison of quantitative shear wave MR-elastography with mechanical compression tests.* Magnetic Resonance in Medicine, 2003. **49**(1): p. 71-77.

95. Pavan, T.Z., et al., *Nonlinear elastic behavior of phantom materials for elastography.* Physics in medicine and biology, 2010. **55**(9): p. 2679.

96. Catheline, S., et al., *Measurement of viscoelastic properties of homogeneous soft solid using transient elastography: an inverse problem approach.* The Journal of the Acoustical Society of America, 2004. **116**(6): p. 3734-3741.

97. Kobayashi, H., Y. Hiki, and H. Takahashi, *An experimental study on the shear viscosity of solids.* Journal of applied physics, 1996. **80**(1): p. 122-130.

98. Brouwer, I., et al. *Measuring in vivo animal soft tissue properties for haptic modeling in surgical*. in *Medicine meets virtual reality*. 2001.

99. Kerdok, A.E., M.P. Ottensmeyer, and R.D. Howe, *Effects of perfusion on the viscoelastic characteristics of liver.* Journal of Biomechanics, 2006. **39**(12): p. 2221-2231.

100. Venkatesh, S.K., M. Yin, and R.L. Ehman, *Magnetic resonance elastography of liver: technique, analysis, and clinical applications.* Journal of Magnetic Resonance Imaging, 2013. **37**(3): p. 544-555.

101. Chen, S., et al., *Shearwave dispersion ultrasound vibrometry (SDUV) for measuring tissue elasticity and viscosity.* Ultrasonics, Ferroelectrics, and Frequency Control, IEEE Transactions on, 2009. **56**(1): p. 55-62.

102. Wang, M.H., et al., *In vivo quantification of liver stiffness in a rat model of hepatic fibrosis with acoustic radiation force.* Ultrasound in medicine & biology, 2009. **35**(10): p. 1709-1721.

103. Chen, S., M. Fatemi, and J.F. Greenleaf, *Remote measurement of material properties from radiation force induced vibration of an embedded sphere.* Journal of the Acoustical Society of America, 2002. **112**(3): p. 884-889.

104. Oestreicher, H.L., *Field and impedance of an oscillating sphere in a viscoelastic medium with an application to biophysics.* The Journal of the Acoustical Society of America, 1951. **23**(6): p. 707-714.

105. Morse, P.M. and K.U. Ingard, *Theoretical acoustics*. 1968: Princeton university press.